University of Birmingham

AGEING OF INTEGRATED-PLANAR SOLID OXIDE FUEL CELLS

BY

GHZZAI ALMUTAIRI

A thesis submitted to

The University of Birmingham

For the degree of

DOCTOR OF PHILOSOPHY

Chemical Engineering
School of Engineering
University of Birmingham
Edgbaston
Birmingham
B15 2TT
July 2013

Abstract

The ageing of Solid Oxide Fuel Cells (SOFCs) is a key problem because of the requirement of 50,000 hours to their lifetime in many applications. At present, such performance is still not attainable because degradation occurs at more than 1% per thousand hours under practical test conditions. In this thesis, the ageing of the Rolls Royce Fuel Cell Systems (RRFCS) Integrated Planar Solid Oxide Fuel Cell (IP-SOFC) was studied under different operating conditions, especially by accelerated degradation testing (ADT), in order to investigate the fuel cell stability and degradation behaviour under non-steady operating conditions for further improvement of the systems.

Cycling tests, as the widely recognised method used for ADT, were performed in this work to enable the simulation of weeks and years of damage over much shorter periods of testing durations, as the cell quality becomes increasingly likely to degenerate at greater numbers of cycles. This thesis presents a theory of ADT and goes on to experimentally determine the durability of the IP-SOFC, in particular the two main challenges faced with SOFC technologies: the structure degradation caused in long-term operation and cycling, and the carbon deposition at anode side when operated with methane.

To study the structure deterioration, the IP-SOFCs were tested at a constant current of 0.17 A per cm^2 at 900 ^oC with hydrogen as fuel. Long-term durability was assessed over more than 6000 hours of testing, including 133 current load cycles and 19 restarts and shutdowns. The average voltage degradation rate was measured. The Ohmic resistance and the microstructural changing along with operation were analysed. One paper “Cycling durability studies of IP-SOFC” on this

work has been published in the *International Journal of Low-Carbon Technologies* [1]. Thermal cycling testing was further performed by fast heating up (5 ^{o}C per minute) and natural cooling down, and serious microstructural degradation was detected in IP-SOFCs.

The influence of carbon deposition on the performance of the IP-SOFCs fed with hydrocarbons was assessed by examining the durability of the IP-SOFCs in conjunction with methane mixed in hydrogen. Two series of experiments were performed to check the IP-SOFC tolerance to carbon deposition. In experiment I, four methane contents were used in the experiment, e.g. 5%, 10%, 15% and 20% in the fuel mixtures of hydrogen and methane. A significantly higher voltage degradation rate was detected when the methane content was increased from 5% to 20%. An improvement on the IP-SOFC performance was also observed with increasing proportions of methane (0-20%) in the fuel. In experiment II, durability test was performed with two methane contents, 5% and 20%. The treatment for removing carbon deposition from IP-SOFC operated with methane was also explored. As a consequence of this, a paper “Direct operation of IP-Solid Oxide Fuel Cell with hydrogen and methane fuel mixtures under current load cycle operating condition” has been submitted to *Fuel Cells* [2].

To understand the mechanism of the carbon deposition, the IP-SOFC operated with methane was dissected into pieces and a temperature-programmed oxidation (TPO) experiment was performed to analyse the carbon formed. It was found that two types of carbon, amorphous and graphitic carbon, were produced with methane as fuel. The effects of the reaction temperature and methane consumption on the carbon formation, and the direct structural damage to the IP-SOFC surface due to the

carbon deposition, were further discussed. A third paper on measurement techniques has been submitted to the *Journal of Power Sources* [3] based on these findings.

This work demonstrates that the long-term durability of the IP-SOFC is very good when pure hydrogen is used as fuel. However, the introducing of even a small amount of methane in fuel has demonstrated the capacity to damage the IP-SOFC through the formation of carbon deposits on the anode surface. Future work is therefore required to identify viable alternative materials and optimal operating conditions.

I dedicate this thesis to my mother, wife, children and all of my family members for their help, support, encouragement and patience during the years of my study.

Acknowledgements

I would like to thank Prof. Kevin Kendall, Dr. Waldemar Bujalski and Dr. Aman Dhir for allowing me to undertake the project under their supervision.

I would also like to acknowledge the financial support from Centre for Hydrogen and fuel cell research which allowed me to complete my work.

In addition, I would like to acknowledge the tremendous support and encouragement of my family throughout the period of study.

Finally, I would like to thank my colleagues and friends who were always there for guidance and advice.

Contents

List of Figures:

List of Tables:

Chapter 1

Introduction

1 Introduction

This chapter provides a short discussion of the core features and characteristics of fuel cells, with particular reference to the solid oxide fuel cells (SOFCs) studied in this research. In addition, the objectives and outline of this thesis are also provided.

1.1 The description of fuel cell

There are increasing concerns about energy security and the levels of CO_2 emissions from burning fossil fuel causing global warming, with the increasing world population and the depletion of global oil reserves. This concern has resulted in a strong demand for cleaner and more efficient technologies to secure future energy supplies. Solid Oxide Fuel Cells (SOFCs), as one of the most promising alternative energy conversion devices, are currently being tested for their viability in terms of replacing the conventional combustion technologies basing on fossil fuels and therefore becoming a mainstay in future sustainable energy supply. In comparison with conventional combustion technology, fuel cells produce lower levels of pollution, higher electrical efficiency and potentially have lower operating cost in the future. Increasing concern about environmental issues and global warming has also brought greater attention to the possibility of using fuel cells to efficiently generate energy from hydrogen, methanol, natural gas or higher hydrocarbons. Fuel cell can utilise various fuels, such as hydrogen, methane (natural gas, biogas, syngas) and reformed fuels (diesel, kerosene), thus it can also form a link between current energy supply systems based on fossil fuels and future development on the basis of renewable, pollution-free gaseous and liquid fuels [4, 5].

Fuel cells are electrochemical devices that directly convert the chemical energy of fuels into electrical energy, with thermal energy as by product. When the fuel oxidises, it reacts with oxygen or other oxidisers. As SOFC operation does not involve the conversion to or from mechanical energy, these cells show a high level of energy efficiency. In addition, fuel cells can be designed in modular form and in different sizes, offering numerous advantages over conventional energy conversion systems. The ability to utilise various types of fuels also means that these cells offer a more flexible and efficient use of existing energy resources.

A fuel cell consists of a fuel electrode (anode or negative electrode), oxidant electrode (cathode or positive electrode), and an electrolyte between the two electrodes that allow the passage of positive and negative ions but which does not permit the passage of electrons. A schematic diagram of a fuel cell is shown below in Figure 1 [6]. In operation, fuel is oxidised at the anode region, which results in the liberation of electrons. These are then transferred to the cathode via an external circuit, where oxygen is reduced to ions that pass through the electrolyte to complete the reaction. The electron flow constitutes a direct current (DC), which can thus be usefully applied to perform a task or be converted to alternating current (AC).

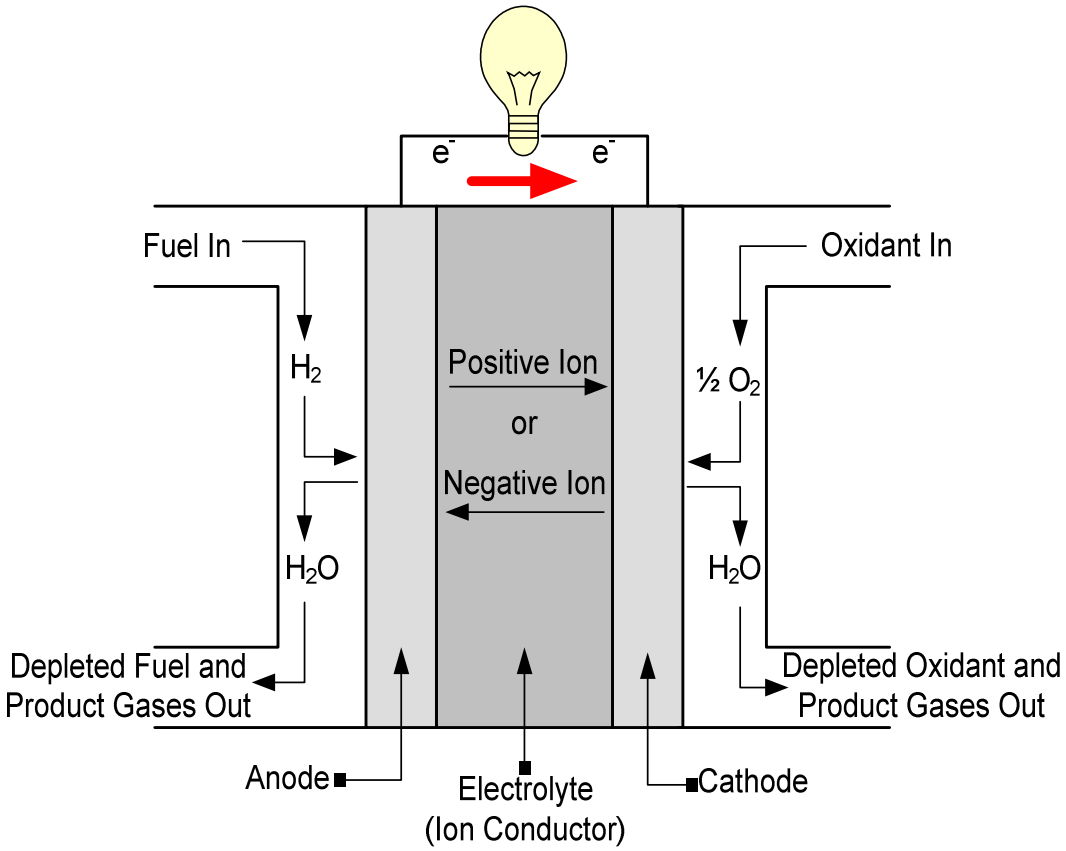

Figure 1: The schematic diagram of a fuel cell (generic scheme) [6].

1.2 Fuel cell types:

Fuel cells are commonly classified based on the types of electrolytes, such as: Proton Exchange Membrane Fuel Cell (PEMFC), Alkaline Fuel Cell (AFC), Phosphoric Acid Fuel Cell (PAFC), Molten Carbonate Fuel Cell (MCFC), and Solid Oxide Fuel Cell (SOFC). The differences of various fuel cells are summarised in Table 1, while Table 2 presents the advantages and disadvantages of common fuel cells in comparison to conventional combustion technologies.

Table 1: Summary of the major differences of the fuel cell types [7].

	PEMFC	**AFC**	**PAFC**	**MCFC**	**SOFC**
Electrolyte	Ion exchange membrane	Mobilized or immobilized potassium hydroxide	Immobilized liquid phosphoric acid	Immobilized liquid molten carbonate	Ceramic
Operating temperature	80°C	65-220 °C	205 °C	650 °C	600-1000 °C
Charge carrier	H^+	OH^-	H^+	$CO_3^=$	$O^=$
External reformer for CH_4	Yes	Yes	Yes	No	No
Prime Cell Components	Carbon-based	Carbon-based	Graphite-based	Stainless (steel-based)	Ceramic
Catalyst	Platinum	Platinum	Platinum	Nickel	Nickel Perovskites
Product water management	Evaporative	Evaporative	Evaporative	Gaseous product	Gaseous product
Product heat management	Process gas+ independent cooling medium	Process gas+ electrolyte calculation	Process gas+ independent cooling medium	Internal reforming+ process gas	Internal reforming+ process gas

Table 2: Advantages and disadvantages of common fuel cells compared to conventional combustions technology [8].

Advantages	Disadvantages
▪ High efficiencies ▪ Excellent part load characteristics ▪ Low emissions ▪ No rotating parts in the main hardware components ▪ Low noise emissions	▪ Life time limitations (partly no knowledge about real life time) ▪ Decreasing electrical efficiencies as function of life time ▪ High investment costs ▪ Low demonstrated availability ▪ Few technology providers

1.3 Solid Oxide Fuel Cell (SOFC):

This thesis focuses on Solid Oxide Fuel Cells (SOFCs), due to the advantages they offer over other types of fuel cell. i) SOFCs operate at a high temperature (600-1000 ^{o}C), meaning that precious metals, which are commonly used in low temperature fuel cells [9], are not required. This reduces the cost of the construction and maintenance; ii) The efficiency of SOFC in converting fuel to electricity is likely as high as 50-60%. SOFCs can also take advantage of the waste heat (co-generation) system, where fuel cell efficiency can increase to 80-90%; iii) SOFCs can function with many kinds of fuels, playing the role of the internal reactor (i.e. reformer). In addition, they are also not sensitive to carbon monoxide, which can therefore be used as the fuel for SOFC, as shown below with the Equation 1-1, for the SOFC reaction:

Anode reactions $H_2 + O^{--} \rightarrow H_2O + 2e^-$

$CO + O^{--} \rightarrow CO_2 + 2e^-$ 1-1

Cathode reaction $O_2 + 4e^- \rightarrow 2\ O^{--}$ 1-2

Overall reaction $H_2 + 0.5\ O_2 \rightarrow H_2O + \text{Heat} + \text{Electricity}$ 1-3

$CO + 0.5\ O_2 \rightarrow CO_2 + \text{Heat} + \text{Electricity}$

The SOFC is characterised by having a solid ceramic electrolyte, which eliminates the electrolyte corrosion and liquid management problems typically associated with PAFCs and MCFCs; SOFC has a high flexibility in the choice of fuel, e.g. carbon monoxide and hydrocarbons can be directly oxidised by SOFCs, because the anode has nickel materials which use the catalytic properties of the nickel anode to reform

them as internal reforming [10-12]. When compared with lower temperature variants, a further advantage of the high temperature of the SOFC is that it can be used as a co-product in various ways, for example in combined heat and power (CHP) systems, or to drive a gas turbine to generate more electricity, which can increase the overall efficiency of the SOFC to in excess of 70% [13]. In addition, a longer lifetime of over 40,000 hours is a standard requirement for stationary applications, while auxiliary power units in transportation applications require approximately 20,000 hours, with more frequent thermal cycling [14].

SOFCs are fabricated from ceramic materials that comprise three main parts: anode, cathode and electrolyte. The electrolyte separates two electrodes (anode and cathode). Baur and Preis (1937) used Yttria Stabilised Zirconia (YSZ) as the first fuel cell electrolyte, with Nickel/YSZ and Lanthanum Strontium Manganate (LSM) layer being used as anode and cathode, respectively [15]. As described previously, fuel is oxidised at the anode region, resulting in the liberation of electrons that are then transferred from the anode via an external circuit to the cathode, where oxygen is reduced to ions, passing through the electrolyte to complete the reaction. This reaction at the anode releases electrons, which are transferred through the external circuit, resulting in the production of the direct-current electricity. Hydrogen and air are the simplest reactants, which are used as fuel and oxidant, respectively. The electrochemical reaction scheme for this system can be seen below in Figure 2.

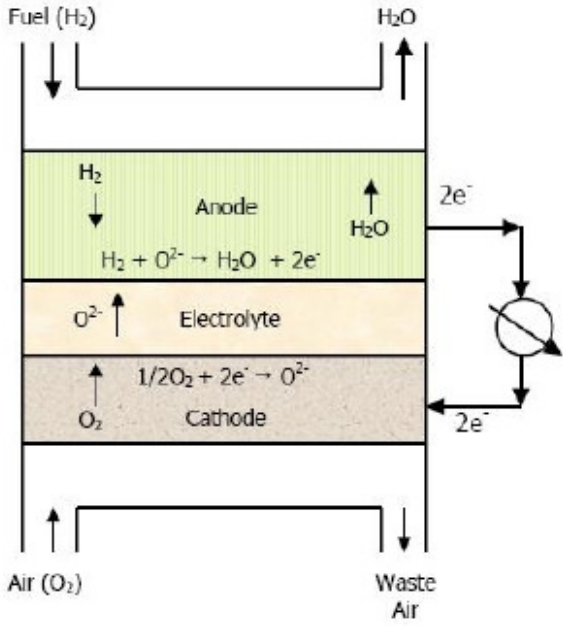

Figure 2: Schematic diagram showing reactions and charge transfer in SOFC.

This electrochemical reaction can only occur at the triple-phase boundary (TPB), which is the collection of sites where the electrolyte, the electron-conducting metal phase, and the gas phase all come together (Figure 3) [16]. The performance of a SOFC is dependent on this structure and it should also be noted that some aspects of the electrochemical reactions are quite different from normal heterogeneous reactions. Therefore, it is useful to consider how the anode works on a microscopic scale [17]. The reaction cannot occur if the TPB is broken and the TPB site will be unable to contribute to the performance of the cell if the ions from the electrolyte or gas-phase fuel molecules cannot reach this area, or when electrons cannot be removed from the TPB site [18]. The fuel will be adsorbed, leading to dissociation on the surface of the metal catalyst (for example Ni), which produces $H_{(ads)}$ that reacts with O^{2-} at TPB. This reaction will then produce H_2O and $2e^-$, after which the water will be diffused through the pores and the electrons will migrate through the metal

and the external circuit to generate power.

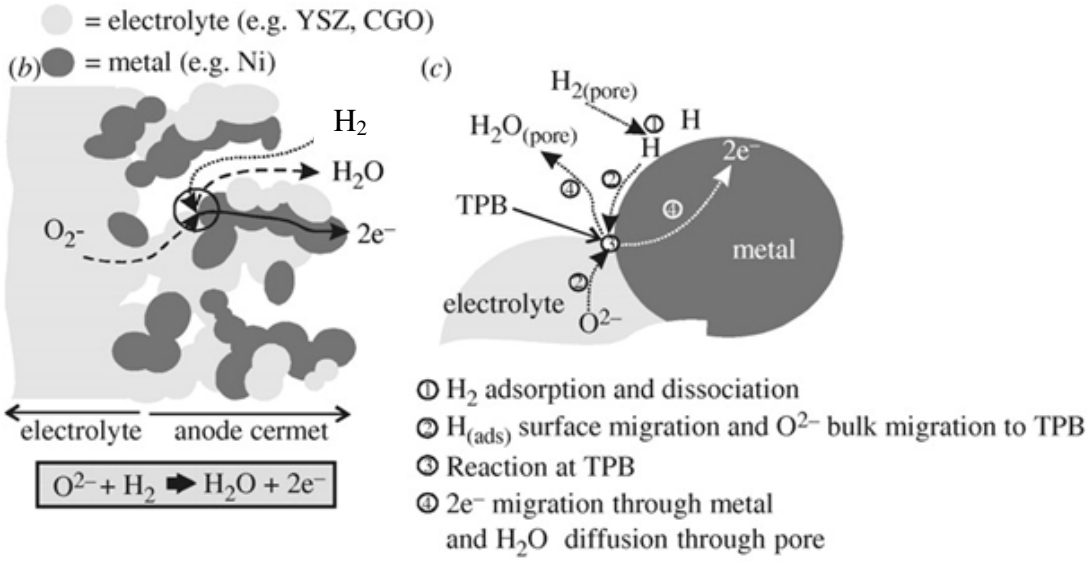

Figure 3: Schematic view of the reaction pathway at SOFC anode cermet and TPB [16].

1.4 Objectives of this thesis:

The discussion above demonstrates the appropriateness of SOFCs for power and heat generation applications. The key problem is the lifetime of the materials under the high temperature operating environment. This work will therefore focus on performing an assessment of the Integrated Planar Solid Oxide Fuel Cell (IP-SOFC) from Rolls Royce Fuel Cell Systems Ltd (RRFCS) under different operating conditions. Particular attention will be given to the two main degradations of SOFC:

- Microstructure changes during long-term operation.
- Carbon deposition with hydrocarbon.

Initially, the research begins with a study on the effect of reduction techniques from

NiO to Ni at anode, as a necessary step which must be performed before SOFC can really work, and then investigates the influence of thermal and current load cycling on the durability of IP-SOFC, using pure hydrogen as fuel. A theory is put forward to suggest that accelerated degradation testing (ADT) can be achieved under certain circumstances. This approach can then be used to simulate weeks and years of damage over much shorter periods of testing durations. Secondly, a fuel mixture containing methane is utilised to study the durability of IP-SOFC under hydrocarbon fuel, especially the effects of carbon deposition on the performance of IP-SOFC.

1.5 Thesis outline

This thesis starts, in the first two chapters, with a literature review of the relevant cell and stack designs, the materials and components used in SOFCs, and the accelerated ageing and durability of SOFCs. A discussion is also be provided to the theoretical arguments regarding the causes of low performance in fuel cells, such as polarization curves, material reasons, fuel related reasons and cycling tests. The literature review also details the fuel used and a brief description of the effect carbon deposition on IP-SOFC performance. This is followed by Chapter 3, which describes the equipment and methods used in this work, e.g. the SOFC test station. Chapter 4 details the methods of the reduction process to the IP-SOFC anode before it can be used for further testing, including the influence of the reduction process and durability studies on the IP-SOFCs. To evaluate the microstructural change in long-term operation, Chapter 5 presents the methods of durability studies conducted on the IP-SOFC operated with pure hydrogen, with particular focus on the influence that thermal and current load cycling have on the IP-SOFC durability. Chapter 6 and Chapter 7 describe the IP-SOFCs operated with methane, in order to investigate the

influence of carbon deposition on fuel cell performance, including the effects of methane content in the mixture fuel on the performance and durability of IP-SOFCs in Chapter 6, and in Chapter 7, a detailed analysis of the consequence of carbon deposition to IP-SOFC structures and components. Finally, in Chapter 8, this thesis concludes the current understanding of IP-SOFC performance, in light of the various areas of investigation undertaken in this thesis.

Chapter 2

Literature Review

2 Literature Review

Following the general introduction to SOFC technology in Chapter 1, the purpose of this chapter is to review, introduce and explain the present state of SOFC technology, followed by a detailed review of the materials and considerations involved in an in-depth experimental investigation of SOFC degradation and ageing.

2.1 Solid oxide fuel cells technology

SOFCs are ceramic electrochemical reactors running at high temperatures up to 1000 ^{o}C [19]. In an operating system at normal atmospheric pressure, SOFCs demonstrate the ability to convert the chemical energy in fuels into electric power, with an approximate efficiency of 45%. The temperature of the exhaust gas emerging from a SOFC is in the region of 850 ^{o}C. Through this feature it becomes possible to synergistically integrate the SOFC with a gas turbine engine generator and to then realise the potential for generation of electricity at an efficiency of over 80%. This concept has become a practical reality with several such SOFC linked gas turbine power generating systems being developed, the first of which was from Siemens Westinghouse for Southern California Edison in 1999 [20], now exhibited at University of California in Irvine.

High temperature SOFCs offer several advantages, including the potential for clean, low pollution electrochemically generated electricity at comparatively high efficiency levels. In comparison with traditionally employed energy systems, SOFCs have also been found to provide high reliability, modularity, fuel adaptability and significantly lower levels of polluting emissions, e.g. oxides of nitrogen and sulphur. In SOFCs, there is no need for a costly external reformer like that in low temperature fuel cell systems, because internal reforming is beneficial. As mentioned above, they are also

suitable replacements for the combustors in gas turbines, with predicted system efficiency of over 80% [21].

2.2 Cell and stack design

In SOFC, cell designs can be divided into two main groups: planar and tubular as shown in Figure 4. Each has its own features and advantages. In planar cell design, the most important requirements are: low Ohmic losses, short current paths, high reversible voltage, low activation losses and uniform temperature distribution. In addition, the design should be strong enough to be easily assembled and handled, as well as being compact and stackable to allow for a high power density [22]. Planar designs are distinguished by having a higher volumetric power density, better electrical performance, and lower fabrication costs by the utilisation of various methods like tape casting, slurry coating, screen printing or other deposition techniques, compared with the tubular design. The tubular design has fewer problems with temperature gradients or with low volumetric power density, as a result of the long circumferential current paths in the electrodes [23]. The advantage of a tubular cell over planar cell design is that there is no need to use seals to isolate the oxidant from the fuel at a high temperature [22, 24]. But, they are more expensive to manufacture than planar SOFCs, as well having the lower volumetric power density depending on tube diameter. Large diameter tubular SOFCs are thus more suited for stationary power generation applications, and not found to be attractive in transportation and military purposes which cycle repeatedly [25]. However, safely heating the Siemens Westinghouse tubular cell requires several hours in order to ensure that the cell is not cracked [26].

Taking into the various designs of SOFCs that have been attempted, the greatest advances have been associated with the tubular design of SOFCs. The drawbacks of Westinghouse tubular design SOFCs are their high electric resistance, low specific power output and volumetric power density, which have restricted the applications of tubular SOFCs for stationary applications and means that they not been found suitable for mobile applications [27].

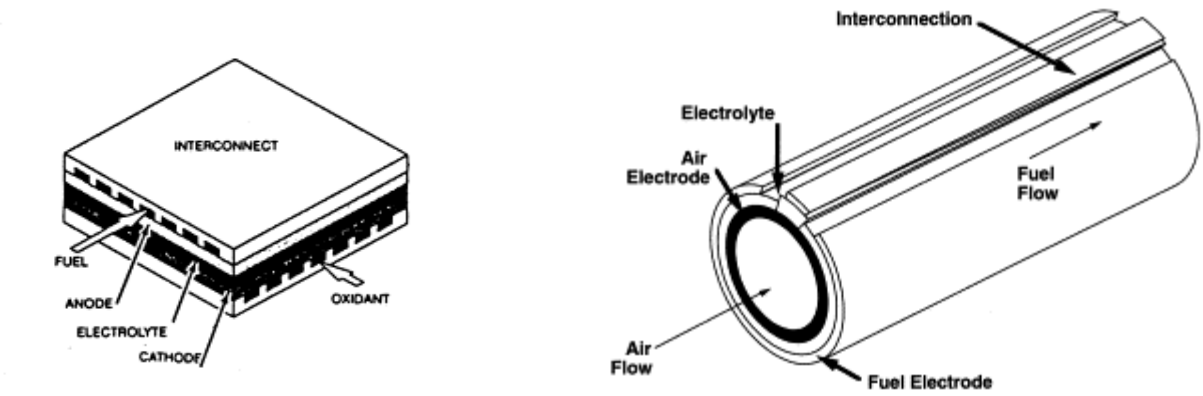

Figure 4: Schematic of the planar SOFC design (left) and the tubular SOFC design (right).

For these reasons and in order to improve the volumetric power density, Siemens-Westinghouse has improved its tubular design into the flattened tubular cell as shown below in Figure 5.

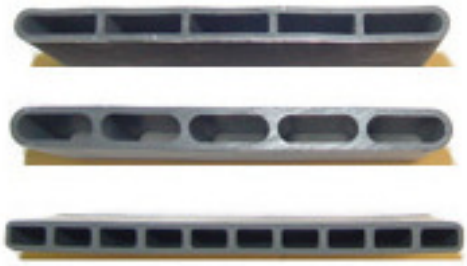

Figure 5: The flattened tubular SOFC cell design.

Another example of a tubular cell structure is the microtubular design. The earliest

study of which was conducted in the early 1990s. This design comprises 1-5 mm diameter tubes that are shorter with lenght between 50 and 200 mm. This is a design that has high power density, low thermal inertia and thermal shock sensitivity in order to allow for faster start-up and shutdown compared with other designs. It can be fabricated as anode supported, electrolyte supported and open-ended. The fuel flow inside the microtubular cells is presented in Figure 6 [22, 28].

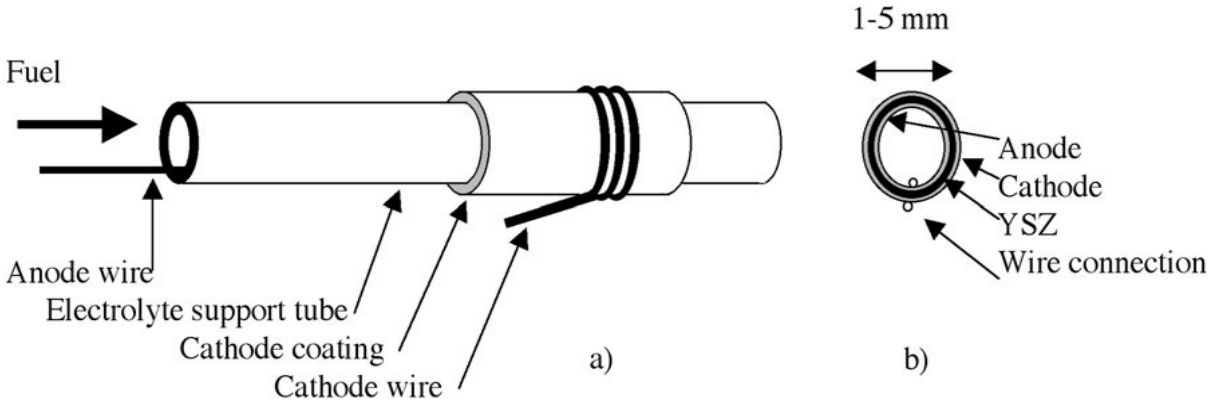

Figure 6: The microtubular SOFC design.

Figure 7 shows the RRFCS IP-SOFC, which is designed in a planar and tubular manner to overcome the disadvantage of both. This kind of cell is connected in series cell design for high voltage and low current, in order to reduce Ohmic resistance and to substantially reduce the production costs typically associated with this method [29].

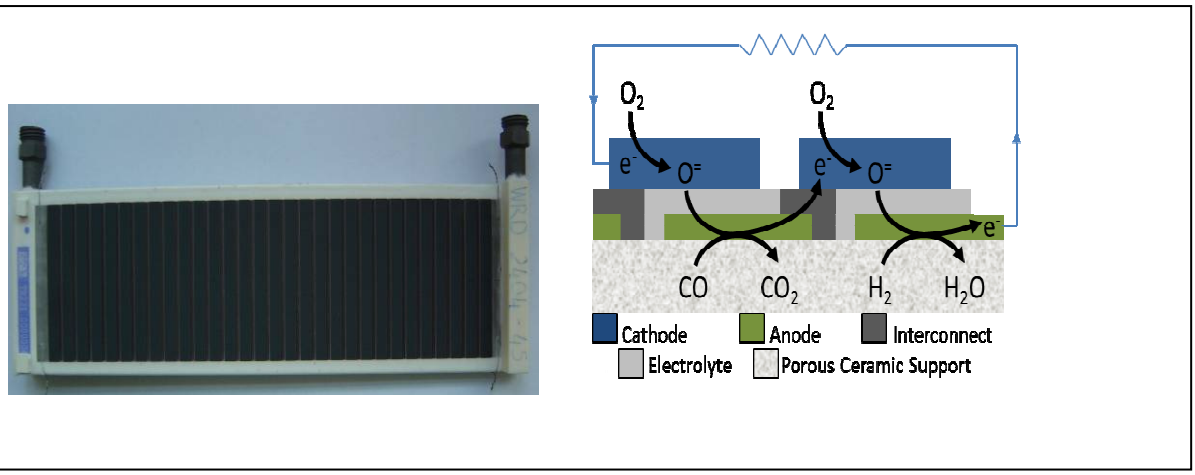

Figure 7: The RRFCS IP-SOFC in series design.

Other important configurations in SOFC classifications can be classified into either self-supporting or external supporting. In the self-supporting group, one of the cell components acts as the structural support of the cell, examples of which are electrolyte-support, anode-support and cathode support. Because of this, the structural support must be the thickest layer in cell components. In contrast, the external-supporting groups are configured as a thin layer on an interconnecting or porous substrate [22].

In the stack design, individual cells are connected together in series, parallel or both. In addition, the type of cell, such as tubular or planar, is also important. The planar cells are easily incorporated into stacks and the separation between the cells is interconnecting materials, which have flow channels to provide fuel and oxidant gases to cells. However, they require high temperature sealing around the plate edges, which is still a big challenge that must be solved at the moment [30]. Stacks can also be made with microtubular structures, by connecting the cathode wires between cells, and anodes at the fuel manifold, as series or parallel connections [31].

2.3 Materials for SOFC

In SOFCs, ions are conducted across the ceramic electrolyte at high temperatures in the range of 600 to 1000°C. SOFC designs (tubular and planar) are comprised of five key types of components: electrolyte, anode, cathode, interconnect and seals. Figure 8 presents the taxonomies of these SOFC materials [32].

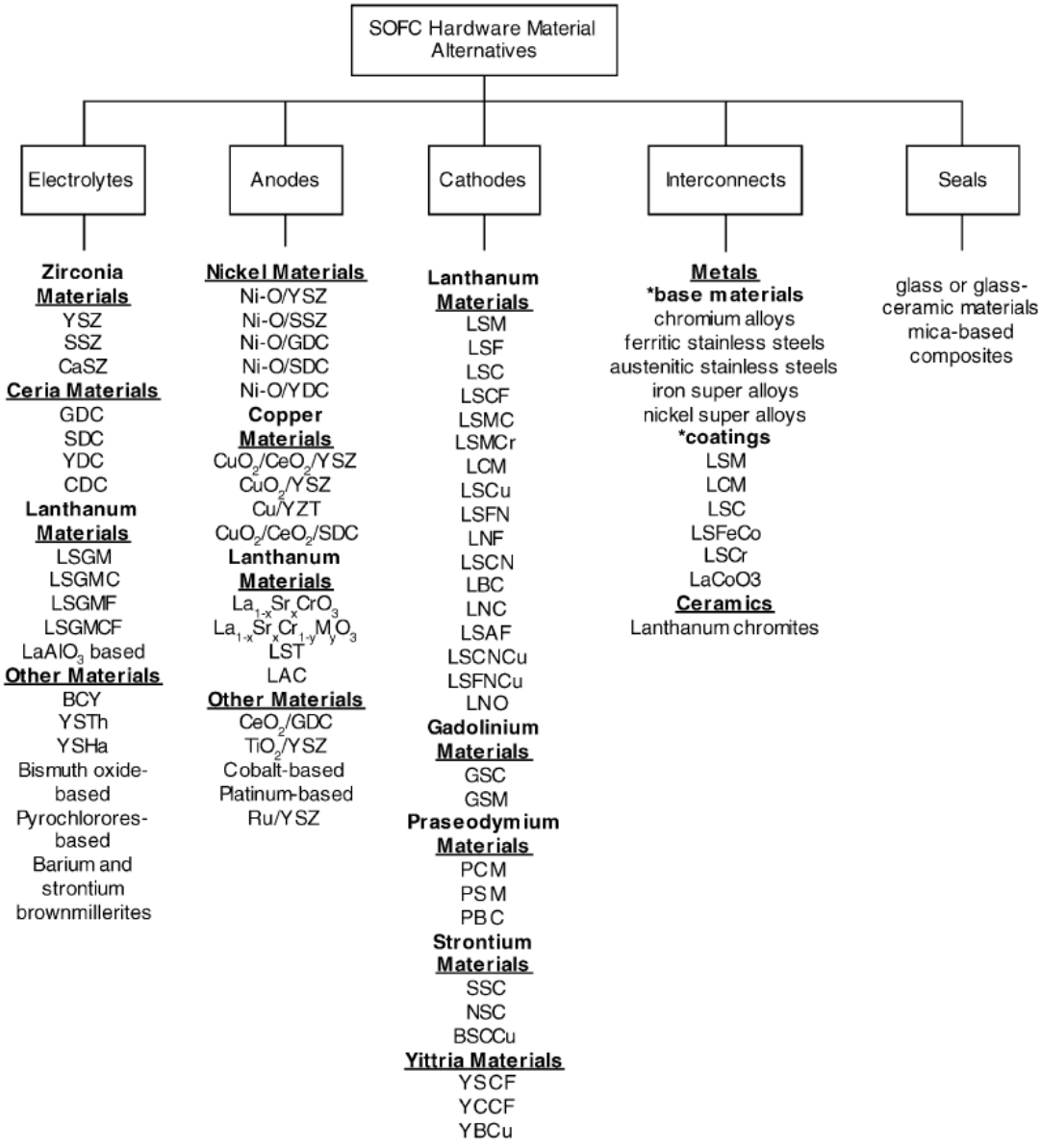

Figure 8: Construction materials for each SOFC component [12].

2.3.1 Electrolyte materials

In SOFCs, the electrolyte plays two major roles, acting as the O^{2-} charge carrier from the cathode to the anode to complete the reactions, and separating the oxidative and reductive half reactions. The requirements for the electrolyte materials are as follows: (1) They must be fully dense to insulate between oxidising and reducing gases; (2) They must have high ionic conductivity, whilst also being an electrical insulator; (3) They must have chemical compatibility with other material components during fabrication and cell operation, as well as being chemically stable at high temperature;.(4) Thermal expansion coefficient values must be close to those of the other component cell materials, in order to avoid delamination and cracking, in addition to reducing stresses during fabrication and operation; and (5) The electrolyte materials should be inexpensive.

Electrolyte materials are mainly classified into three systems: yttria-stabilized zirconia, gadolinium- or samarium-doped ceria and magnesium-doped lanthanum gallate.

The yttria-stabilized zirconia (YSZ) electrolyte is the most common solid electrolyte used in SOFCs operated at high temperatures (800-1000^{o}C), due to its high conductivity (about 0.1 S per cm) at 1000^{o}C. This material consists of 8 mol% of Y_2O_3 stabilized ZrO_2, commonly known as YSZ [33]. Badwal and Foger [34] found that zirconia electrolyte doped with yttria has good thermal and mechanical shock resistance when operated in the temperature range of 800 to 1000 ^{o}C. YSZ is one of the best electrolyte materials from the high quality raw materials available, due to its good chemical and mechanical stability [35]. Extensive research has been carried out on YSZ because of its high ionic conductivity, low electrical conductivity and

stability in both reducing and oxidising conditions [36]. There is a relationship between the ionic conductivity of YSZ and the concentration of yttria. The conductivity of YSZ increases with larger amounts of yttria, until approximately 8 mol%, and then decreases for high amounts of yttria [36, 37]. Many researchers have added alumina, 5-20% of alumina to YSZ in order to enhance its mechanical properties, sintered density and electrical properties [38]. Despite its popularity, however, Ralph et al [39] indicated that YSZ did not operate well at temperatures below 700 ^{o}C, due to reduced ionic conductivity. Ishihara, et al. [40] also found that the reliability could be low when the thickness of YSZ is made extremely thin (1 µm).

Another zirconia based electrolyte material is scandia-stabilized zirconia 'Sc_2O_3-ZrO_2' (SSZ). 8-9 % SSZ can be operated at intermediate temperatures (600-800 ^{o}C) as the ionic conductivity of SSZ is high and its mechanical stability is better than other stabilised zirconia electrolytes [34]. However, the cost of the SSZ electrolyte material is high due to the expensive scandium. In addition, its ionic conductivity has also been shown to deteriorate over time [41].

Other electrolyte material is Ceria-based electrolytes, which have been shown to be extremely suitable for use as electrolyte materials for intermediate temperature SOFCs (550-650 ^{o}C). This is because of their high ionic conductivity, lower polarization resistance, and their compatibility with high performance electrode materials, such as cobalt containing perovskite oxide cathode [42]. The major problem with ceria is that it becomes electrically conductive at low oxygen partial pressure [43]. Gadolinium and samarium added to ceria (CGO and CSO) increase its conductivity due to the least mismatch between them [44, 45].

Another common material for use in electrolytes is strontium/magnesium-doped

lanthanum gallate (LSGM). This electrolyte is fabricated from perovskite ($LaGaO_3$) with the dopants strontium and magnesium $La_{1-x}Sr_xGa_{1-y}Mg_yO_3$ (LSGM), and shows good ionic conductivity at low temperatures [46].

Weber [47] summarises the advantages and disadvantages of common electrolyte materials. While the properties of materials is an important characteristic in the selection of an appropriate electrolyte for SOFC applications, other important considerations include compatibility with electrode materials during fabrication and cell operation, as well as the cost of the material.

2.3.2 Cathode materials

The cathode (air, O_2 or oxidant electrode) is the site where O_2 is reduced to O^{2-}. The general requirements for a SOFC cathode are: high mixed ionic and electrical conductivity, chemical compatibility with electrolyte materials, stability under oxidising environments, thermal expansion coefficient close to that of the SOFC electrolyte and good adhesion to the electrolyte surface. Ideally, the cathode should also be simple to fabricate and utilise inexpensive materials [48]. There are few materials that meet these requirements.

Most cathodes are constructed from perovskite type oxide (ABO_3), such as LSM, LSF, LSCF and LSGM. LSM (lanthanum strontium manganite) consists of $LaMnO_3$ doped with Sr to produce $La_{1-x}Sr_xMnO_{3-x/2}$ (LSM). LSM is the most common cathode material for high temperature SOFCs (800-1000 ^oC). This is because it has high ionic and electronic conductivity, high electrochemical activity for the oxygen reduction reaction, high thermal stability, and a high degree of chemical compatibility with the most common electrolytes, such as YSZ, GDC and LSGM [49]. At high temperatures, the operation of LSM is characterised by its excellent microstructure

and long-term performance stability [49]. The problem with this material is that very low concentrations of Sr cause the electrical conductivity to decrease [32], while at temperatures above 1300 ^{o}C, the LSM will react with the YSZ electrolyte [50]. Some studies have investigated the addition of other layers onto the LSM cathode in order to improve its performance, with layers such as YSZ [51], SDC [52] and GDC [50] composite layer being added at the interface of cathode-electrolyte.

Another ABO_3 perovskite oxide is lanthanum strontium cobalt ferrite (commonly known as LSCF), which is operated at low temperatures (between 650-800 ^{o}C) with an YSZ electrolyte. Recently, there has been growing interest in LSCF perovskite as a cathode material for SOFC applications, as it shows high electrical and ionic conductivities, excellent catalytic activity for the oxygen reduction at low temperatures and a superior chemical compatibility with doped CeO_2 electrolytes [42]. The electrical conductivity of $La_{1-x}Sr_xCoO_{3-\delta}$ in air increases with increasing temperature, when x = 0.0, 0.1 and 0.2, and then decreases with increasing temperature at x = 0.3 [53]. The electrical conductivity of LSCF is 275 S per cm and its ionic conductivity is around 0.01 S per cm at 700 ^{o}C [54, 55]. In contrast, LSCF typically has high thermal expansion coefficients (> 20 x 10^{-6} per K) and reacts with the YSZ electrolyte at low temperatures, which are typically 700 ^{o}C. This is because the LSCF cathode contains Sr materials that react with the zirconia-based electrolyte to produce a highly resistive reaction product such as $SrZrO_3$ [55]. In order to avoid this issue and reduce the polarisation resistance, ceria-based oxide interlayers such as GDC [56] and SDC [57] are usually employed to separate the LSCF and YSZ.

There are a number of other promising cathode materials, including perovskite lanthanum strontium manganese chromite (LSMC) [58] and $La(Ni_{0.4}Fe_{0.6})O_3$ (LNF)

[59]. The choice of cathode materials is largely dependent on the particular electrolyte materials used, with care being taken to match thermal expansion coefficients and avoid undesirable reactions with the cathode/electrolyte interface. Lanthanum strontium manganite (LSM) based perovskites are still generally the materials of choice for SOFC cathodes for YSZ at high temperatures (800-1000 ^{o}C), whilst lanthanum strontium cobalt ferrite (LSCF) based perovskites are preferred for cathodes of SOFCs for doped ceria electrolytes. LSCF shows acceptable performance for SOFCs operating at intermediate temperatures (600-800 ^{o}C).

The target for the development of cathode materials is to reduce the operating temperature, while decreasing the electrode polarisation losses. One way to overcome this issue may be through the addition of a certain amount of noble metals, such as palladium [60], silver [61], or platinum [62], to the most common cathode materials.

2.3.3 Anode materials

The primary function of the anode in SOFCs is to oxidize the fuel. Other important functions include the use of anode as a support material during fabrication in planar designs as well as its ability to function as an internal reformer of the fuel when hydrocarbons, such as methane, are used. There are a number of important considerations in the design of the anode: Firstly, it should be composed of a high density material, which requires good chemical and thermal stability during fuel cell fabrication and operation. High electrical conductivity under fuel cell operating conditions and high electrocatalytic activity are both essential. In addition, the coefficient of its thermal expansion must be similar to the neighbouring cell components and must be chemically compatible with electrolyte components. Ease

of fabrication into the required microstructures and the inexpensive materials are also important considerations. Furthermore, the anode must be able to provide mechanical support to other components within the cell and to direct the internal reforming for hydrocarbon fuels [63, 64].

Many anode materials were studied in the early developmental stages of SOFCs, including graphite, platinum, iron, cobalt, and nickel. The current preferred anode material for SOFC is Ni metal, due to its low cost, good chemical stability and excellent catalytic activity toward hydrogen oxidation and reforming of hydrocarbon fuels.

There are many potential problems in the usage of Ni anodes in SOFCs such as carbon deposition, mismatch in thermal expansion coefficients of YSZ and Ni [65] and poor binding [66] to overcome these problems Nickel with YSZ is used together as the anode material.

The Ni/YSZ anodes are the preferred anode for SOFC running with H_2 when the operating temperature ≥ 800 ^oC [67]. The current trend is to reduce the operating temperature to below 800 ^oC, however, which makes the electrolyte very thin and means that the anode must act as a support for the other cell components. The performance of the Ni/YSZ anode depends critically on factors such as the microstructure of the porous YSZ, the distribution of Ni on the surface of the anode, the practical size of YSZ and NiO and the ratio in which they are used. The particle sizes of YSZ are normally between 0.2 to 0.3 μm, whereas the particle sizes of NiO powders are ~1 μm. The Ni to YSZ volume ratio usually varies from 35:65 to 55:45 [68]. Porosity is increased through the reduction of the NiO to Ni, which decreases

the volume of this phase by 25%, greatly increasing the porosity [65]. The amount of Ni must be over 30 vol.% in order to achieve the percolation threshold for electrical conductivity [69].

Several solutions have been proposed regarding the problem of carbon deposition. Firstly, carbon deposition does not arise on the anode until the operating temperature exceeds a value of about 750 ^{o}C [70, 71]. The second solution is to use new anode materials, which can promote hydrocarbon oxidation and therefore avoid carbon deposition. It is replaced Ni cermets with materials containing Cu with ceria or samaria doped ceria [72-74]. Other solutions are looking at alternative anode materials with oxide ion and electrical conductivity (mixed-conducting), which have an advantage in that an electrochemical reaction can occur between the entire electrode and gas phase. In comparison to Ni or Cu, it is difficult to find materials that have the catalytic activity for many of the fuels, such as hydrogen oxidation and methane reforming, while still having a good degree of ionic and electrical conductivity. Some materials with mixed-conductivity have been studied as alternative anode materials, for instance $ZrO_2/TiO_2/Y_2O_3$ [75], doped $LaCrO_3$ [76], LSCF ($La_{0.6}Sr_{0.4}Co_{0.2}Fe_{0.8}O_3$) [77], LSCV ($La_{0.8}Sr_{0.2}Cr_{0.97}V_{0.0.03}O_3$) [78] and La, Fe, and Y $SrTiO_3$ [79].

Redox (Reduction and Oxidation) behaviour, in other words re-oxidation, may occur in the degradation of the Ni-YSZ anode. The volume noticeably increases when Ni-YSZ is kept at a high temperature in an oxidising atmosphere, because when the Ni is oxidised to the NiO the volume expands. The YSZ structure can experience a mechanical failure if before the initial reduction of Ni and NiO get rearranged [80, 81]. For this reason, a constant and a stable fuel gas supply is needed and gas leaks

should be avoided, because they can oxidise the anode.

2.3.4 Interconnecting materials

The reason for interconnection in a SOFC is to carry an electrical current between the electrodes and the external circuit, as well as to protect the cathode material from the reducing environment of the fuel. Therefore, the materials used must have very high electrical conductivity, high density and be stable in both the oxidising and reducing environments. For operation at high temperatures over long periods of time, these materials must be chemically and mechanically stable, as well as being resistant to sulfur poisoning. Thermal expansion must be matched with the expansion of other cell components. They must be chemically stable with neighbouring fuel cell components during operation and fabrication. Finally, simple fabrication and uses of relatively inexpensive materials are important [82].

Options for the interconnect are typically divided into ceramic and metallic materials. Ceramic interconnects are fabricated from semiconducting oxides, as they have good stability in air and are chemically compatible with neighbouring cell components. The conductivity of semiconducting oxides increases with higher temperatures, which is well-suited for SOFC application and for the high operating temperature [83]. The most common candidate material used in the interconnect for SOFCs is doped lanthanum chromate ($LaCrO_3$), which has a relativity good electrical conductivity [84]. Certain properties can be improved, such as conductivity, defect chemistry, chemical stability, thermal expansion and mechanical strength, with the addition of dopant materials like strontium and calcium [84-86].

Other kinds of interconnect materials are metallic substances, due to the reduction of

the operating temperature below 800 ^{o}C [87]. They have higher electrical and thermal conductivity than La-chromite, with relatively low cost, ease of manufacture and good workability [82]. Another function of the interconnect is facilitated by the metallic materials, which can be applied as bipolar plates in a planar SOFC. The metallic interconnect can be divided into five metallic alloy groups: chromium alloys, ferritic stainless steels, austenitic stainless steels, iron super alloys and nickel super alloys [88]. The availability of a chromium alloy as an interconnect for SOFCs is useful, due to the high electrical conductivity of chromia, low cost and enhanced mechanical properties [87]. However, at operating temperatures above 900 ^{o}C, the chromium will be oxidized to form an oxide layer on the cathode side [89]. Iron-based alloys can also be used as interconnects in SOFC applications, because their coefficients of thermal expansion can be matched with other SOFC components at an operating temperature of around 800 ^{o}C [90, 91]. Metallic interconnects still face some problems, such as the higher thermal expansion coefficient than most other cell components [92]. It may be possible to improve the metallic interconnect properties through the application of perovskite oxide coating, which improves their performance. The LSM has been investigated as interconnect coating, because of its high electrical conductivity [93]. Like the LSMs, LSCM materials can be used as perovskite oxide coating, due to their properties.

Research in both designs (tubular and planar) seeks cutting interconnect costs by reducing operating temperatures, enabling the use of cheap and established interconnect SOFCs materials.

2.3.5 Sealing materials

Many tubular designs are seal-less. However, in planar SOFCs designs, several types of seals are required, such as those able to attach the cell to the interconnect and/or metal, as well as seals at all possible leakage points. The seal materials must possess certain characteristics: high electrical insulation; compatibility with other cell components, in terms of thermal expansion and chemical compatibility; have high physical and chemical stability; be gastight; have a high degree of mechanical bonding strength; and be constructed from inexpensive and readily available materials [32, 34]. Available high temperature seals can be divided into many categories: glass seal, glass-ceramic seal, compressive seal, metal seal, ceramic-composite seal and compliant seal [94].

All types of seals can encounter significant problems during long term operation at high temperature. These can result from corrosion effects, long-term phase changes such as devitrification, or from cracking associated with different operating conditions, including heating up, cooling down, dynamic load conditions and redox cycling [94]. Currently, the best of these materials for sealing SOFCs are glass-ceramic and composite seals, because of their stability and low chemical reactivity [32, 94].

2.4 Fuels used

The kind of fuel used depends on the type of anode materials, because electrochemical oxidation occurs in an operating SOFC that takes place on the TPB at the anode region. This reaction occurs within 10 to 20 μm of the electrolyte/electrode interface [25]. Three different reforming modes are possible

using SOFC applications: external reforming, indirect internal reforming and direct internal reforming. In the first two cases, the purpose is to completely convert the fuel to hydrogen and synthesise a gas that is electrochemically oxidized afterwards [95]. In the third case, the SOFC is a promising fuel cell because it can operate with more fuels types, such as hydrogen, syngas, hydrocarbons and liquid fuels.

2.4.1 Hydrocarbon gases

As mentioned earlier, two of the principal advantages possessed by SOFCs are tolerance to CO and CO_2, which is produced by reactions of hydrocarbons, and the ability to use hydrocarbon fuels without any preliminary treatment or the addition of an oxidant. Direct utilisation of hydrocarbons refers to the addition of the fuel to the anode where the anode reaction occurs. This reaction can be either the electrochemical oxidation of the products formed by decomposition of the fuel, or the partial electrochemical oxidation of the fuel molecules themselves [95].

Because at the SOFC anode there has some metal catalysts (e.g. Ni, Fe and Cu) operating at a high temperature, this is a suitable environment for the direct reformation of hydrocarbons. The main drawback to direct reforming of hydrocarbon is carbon deposition, resulting in the deactivation of catalyst sites, thus causing blockage or fracture of the cell. This depends on many factors, such as operating temperature, feed [96, 97], anodic polarisation [98] and type of catalyst used.

The hydrocarbon reactions only require nickel particles as catalysts, but electrocatalytic oxidation can still only occur at the TPB. The anode (Ni/YSZ) provides both a fixed catalyst and an extended area where fuel molecules can react with oxide ions to lose electrons. The most common reforming mechanisms in SOFC

come from the water shift reaction [99], partial oxidation [100, 101] and dry reforming [102, 103], all of which produce carbon deposition in varying degrees.

2.4.2 Liquid fuel

Whether or not the direct utilisation of liquid fuels is suitable in SOFCs depends on several factors: The first of these is the tendency of fuel to create carbon deposits at high temperature, thereby reducing the condition found on the anode side. Another important issue is the cost and availability of this fuel, as well as the ease of its storage and transport to the SOFC. Other important factors are toxicity and the environmental impact [95]. Jiang et al. [104] found that the addition of water to ethanol improves the performance of the SOFC, which had Ni-YSZ as the anode. Another anode material for methanol fuel is copper, due to its poor catalytic cracking activity and resistance to carbon deposition [105]. However, a Cu-CGO anode operated with dry methanol was shown to be unstable during operation, because of delaminating of the anode from the electrolyte CGO. In order to overcome this problem, the copper anode is improved with the addition of Cu-ceria [106]. Liu et al. [107] studied NiO/SDC anode materials, for SOFCs with SDC electrolyte and SSD/SDC cathode. This cell was operated with hydrogen and ammonia to compare the performance obtained with methanol liquid fuels. The power density when operated with methanol was found to be higher than that with ammonia and lower than that of hydrogen.

The discussions above have illustrated that the main problem facing IP-SOFC using Ni/YSZ anode occurs in the use of hydrocarbon fuels. This problem is carbon deposition, which is discussed in more depth in the later sections.

2.5 Actual performance of SOFC

The polarisation curve describes the relationship between the cell voltage and current, usually plotted as voltage versus current in A. This is the standard figure for the evaluation of fuel cell performance, and is dependent on the overall cell reaction, the kind of reactant material at the cathode and anode, and the particular reaction products. When the electrons are produced and pass from the electrode via an external load, the voltage drops due to irreversibilities associated with internal resistances.

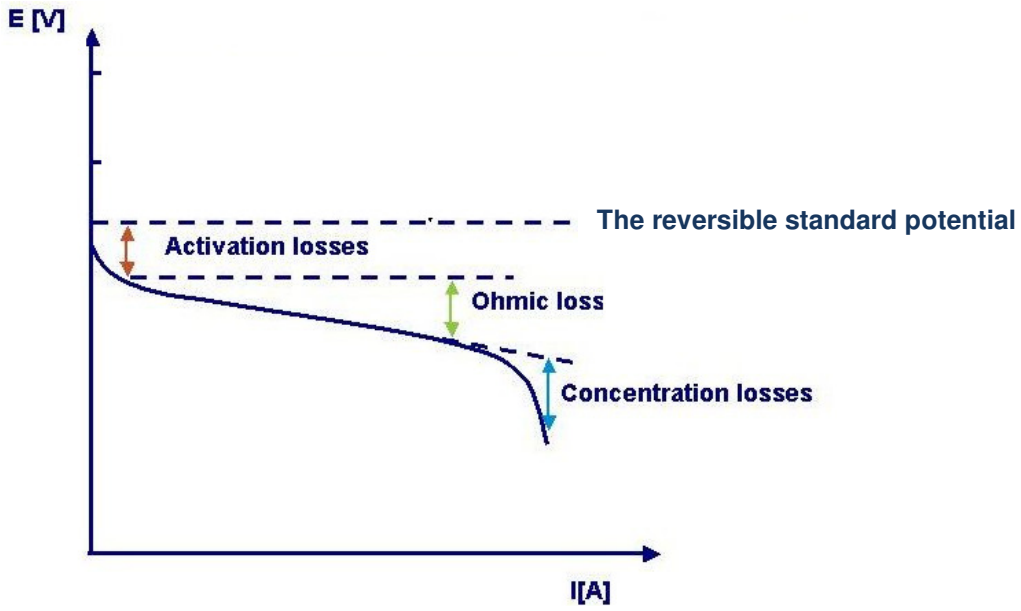

Figure 9: A typical polarisation curve consists of three regions [108].

A typical polarisation curve for a fuel cell showing the net voltage (V_{cell}), is illustrated in Figure 9. This polarization curve consists of three regions: activation (η_{act}), Ohmic (η_{ohm}) and concentration (η_{conc}) polarizations, which are attributed to voltage loss in the fuel cell [108].

2.6 Degradation phenomena in SOFC.

Before going into further detail about the degradation, it is vital to understand the apparatus for all elements in SOFCs. For SOFC systems, a higher cell and stack life time is required i.e. around 40,000-50,000 hours and in order to maintain such high cell and stack life degradation of all components must take place very slowly. In the course of operation, if a change occurs in the cell it can lead to clogged reaction sites or transport paths for species, thus the overall cell reaction and degradation will proliferate. The variations in the electrode / electrolyte interfaces and grain boundaries are acute in the degradation of the fuel cells. When microstructural changes are taking place in the interface regions, such as impurity segregation [109], this can inexorably affect the performance of the cell. The interface regions not only provide the TPB, but are also active for diffusion and segregation of species involved in the fuel cell reactions and mass transportation during the operation.

As can be seen from the above discussion, the selection of the appropriate material for SOFC construction can mitigate fuel cell degradation. In SOFC commercialisation, fuel cell degradation can be considered to be one of the most significant technological problems facing researchers, and consequently a clear understanding of deactivation phenomena has not yet been reached [110]. However, it is possible to specify a number of fuel cell degradation pathways. The studies have specified the following fuel cell degradation pathways:

2.6.1 Microstructural changes

Microstructural changes represent one of the two main kinds of degradation that can occur during the operation of a SOFC. As mentioned above, the SOFC is operated at high temperature (700-1000 ^{o}C) to achieve high performance. This causes the

electrical conductivity of the LSM and the ionic conductivity of the YSZ to increase exponentially with increasing temperature [111]. In addition, the catalytic activity of the electrodes also has an exponential relationship with increasing temperature. However, microstructural changes also arise due to high temperature of operation, such as densification and particle coarsening with the consequent decrease of the TPB. In addition, it is possible that there is a loss of percolation and hindered diffusion. Because of the sintering of Ni, this phenomenon appears particularly evident in the anode [112-114], but it has also been observed at high temperatures (900–1000 ℃) for the LSM [115]. Another phenomenon that may change the microstructure is Ni evaporation from anode at high temperatures in the presence of water vapours [116].

Nickel agglomeration in the anode is a usual and steady mode of degradation. At the surface, the electrochemical reaction abruptly stops due to the broken link between the current collector and the electrolyte, which occurs due to the pooling of nickel. Close contact between nickel particles is needed for electrical conductivity and thus, at high temperature nickel starts to pool [117]. In order to avoid this nickel mobility, the cermet microstructure control must therefore be very carefully designed [118].

2.6.2 Carbon deposition

Most current studies into SOFCs focus on the usage of available hydrocarbon fuels. Ni/YSZ cermet is the most commonly used anode material, despite certain disadvantages when hydrocarbons are used as fuels. Therefore, there is a need to develop alternative anode materials that are capable of displaying mixed conductivity when subjected to a range of fuel conditions [18]. In general, the anode of SOFCs consists of metallic materials (for example Ni) and operating at high temperature.

This make it suitable for the direct reforming of hydrocarbons, but the main problem is carbon deposition [119, 120]. Hydrocarbons can be oxidized on the anode side to generate electricity; but as a result, they also produce several unwanted carbon coking reactions. It is known that nickel can promote hydrocarbons pyrolysis, thereby causing carbon to deposit [121].

The catalysis material will be deactivated by this deposition, which causes physical blockage or fracture of the cell in extreme cases, leading to reduction in cell performance. The carbon deposition can be avoided by changing the parameters of the reaction. For example, reduction in operating temperature leads to non-deposition of carbon on the surface of nickel anode. Otherwise, adding water to an oxidant will oxidize the deposited carbon to CO_2 .To avoid carbon build-up on the nickel anode surface and maintain carbon free conditions a C:O ratio of less than 8 is required [122].

Others ways to avoid carbon deposition include the change of Ni with alternate materials that are Cu-based and Ru-doped. Such anodes are studied for the effect of carbon deposition and they found, that these materials have high tolerance to carbon deposition but the Cu-based anodes have less activity for reforming, and the Ru-doped anodes are more expensive compared with the Ni-based anodes. Other studies have found that the dopant into zirconia affects electrode performance and durability in the Ni-based anode [17, 123, 124]. They have found that Ni-scandia stabilised zirconia (ScSZ) anode is less affected by carbon deposition than the Ni-YSZ anode, under power generation by internal reforming of methane [125, 126].

Cells using Ni/YSZ anodes that are fuelled by any mixture related to natural gas face potential problems of impurity poisoning and carbon deposition. Impurity poisoning, such as phosphide, chloride, and sulphide, poisons the SOFC anode leading to rapid degradation. Carbon deposition occurs because Ni is an excellent catalyst for carbon deposition reactions, such as methane cracking (Equation 2-1), reduction of carbon monoxide (Equation 2-2) and disproportionation of monoxide (Equation 2-3). Therefore, Ni catalyst can be deactivated by the carbon deposited, accelerating cell degradation [127].

$$CH_4 \rightarrow C + 2H_2 \qquad 2\text{-}1$$

$$CO + H_2 \rightarrow C + H_2O \qquad 2\text{-}2$$

$$2CO \rightarrow C + CO_2 \qquad 2\text{-}3$$

Various strategies have been devised in an attempt to curb carbon deposition in SOFCs. A study conducted into the direct oxidation of natural gas indicates that the prevention of carbon deposition on a Ni/YSZ anode is possible by increasing the operation current density and lowering the operation temperature [128, 129]. However, these two operation parameters are not easily attainable in real SOFC systems. Another strategy that has been used for the prevention of carbon deposition in the internal steam reforming of natural gas is the use of a high steam to carbon ratio (S/C). This strategy dilutes the fuel, however, reducing the cell electrical efficiency. In addition, the endothermic reforming reaction leads to disproportionately large temperature gradients in the stack. Consequently, real SOFC systems normally use an external reformer to supply syngas obtained from the steam reformation of methane [130, 131].

A number of different carbon species exist and their deposition varies depending on the conditions of reactions. One of the species of carbon is referred to as carbidic (C bonded to Ni), which are formed at temperatures equal to or less than 350 ^{o}C, meaning that they are not normally observed in SOFCs. The second carbon species is referred to as adsorbed or amorphous carbon, which is formed at temperatures above 350 ^{o}C. The last species is referred to as graphitic layers and are formed at temperatures above 450 ^{o}C. Graphitic layers and adsorbed carbon are easily deposited in hydrocarbon-fuelled SOFCs [127].

In an attempt to resolve the carbon deposition problem, Ni/YSZ has been replaced by many substitute anode materials, such as GDC, doped $SrTiO_3$ [132] and Cu-CeO-YSZ [127]. Nonetheless, these substitute materials have certain inherent disadvantages, such as complicated fabrication processes, low conductivity or poor electrochemical catalyst activity. This leaves Ni/YSZ cermet as the preferred anode material. For this reason, it is crucial to properly understand carbon deposition behaviour on the Ni/YSZ anode.

Carbon deposition can be decreased by increasing the current density and can even reach zero at a critical current density [133]. Steam supplied in the feed stream has also been shown to decrease the amount of carbon deposition through the study conducted by Laycock, Staniforth and Ormerod [134]. Increases in temperature in their study initially caused the amount of carbon to decrease, until a certain point after which it increased.

Research into carbon deposition in the SOFCs with a Ni-based anode commonly focuses on three critical issues. The first factor is thermodynamic calculation, which assists in the prediction of the carbon deposition conditions. However, such

calculations are likely to deviate from real situations and therefore require careful experimental verification. Some experimental studies into thermodynamic calculation have already been conducted for certain fuels, such as direct oxidation and the internal reforming of methane. The second issue is the species of the deposited carbon. Several studies have indicated that the carbon morphologies and species depend on the operation reactants and temperature [127]. Through the use of temperature-programmed oxidation (TPO) and temperature-programmed reduction (TPR), some researchers have identified three carbon species from methane cracking, depending on the reaction temperature range [135]. In the SOFC operation temperature range of 600 ^{o}C to 1000^{o}C, carbon exists in the form of graphite, while at lower temperatures carbon nanofibers are formed which cannot be observed at high temperatures [96, 136]. In addition, Matsui et al. observed that carbon formed under current is hydrogenated and can therefore be more easily removed than carbon formed under open circuit voltage (OCV). Finally, the last issue is the degradation mechanism and behaviour of the cell deposited with carbon. This issue assists in predicting whether carbon deposition occurs or whether performance degradation is reversible [137].

2.6.3 Other degradation phenomena

2.6.3.1 Reactions between LSM and the electrolyte

Zirconium oxide reacts with La and Sr to make up the LSM. This can lead to the formation of non-conducting phases, such as $La_2Zr_2O_7$ or $SrZrO_3$ at the interface between the LSM and YSZ, causing deterioration of the catalytic activity of the cathode. These defects have been detected experimentally by microscopic observations [138] and thermodynamically modelled with multicomponent phase

diagrams [139, 140]. A key parameter in controlling the tendency towards the formation of foreign phases is the composition of the LSM, and in particular the amount of Sr.

2.6.3.2 Poisoning by Cr

Some of the interconnects in the fuel cell stack are metallic components that contain a certain quantity of Cr in order to resist the temperature of operation. The transfer of volatile chromium oxides and hydroxides from the surfaces of the metals to the cathode occurs due to the hot air flowing along these chromium-containing alloys. Through the use of microscopic techniques, studies have identified the presence of Cr near the TPB, and have made observations of a strong decrease in performance [141, 142]. This change is due to the formation of volatile chromium oxides at the surface of metallic components in the stack, and then transport to the cathode side is explained by the mechanism proposed by the literature. This formation tends to precipitate at the active sites in the cathode [143].

2.6.3.3 Crack formation in the electrolyte

Leakages or mishandled on/off cycles reoxidise the anode support materials because oxygen passes through the anodic compartment. This results in the formation of NiO, causing a difference in the molar volume of Ni and its oxides, which in turn leads to the expansion of the oxidised Ni particles. This may be a cause of significant internal stresses, which bring the thin electrolyte under tension with the consequent formation of cracks in the anode support [144, 145].

2.6.3.4 Formation of nickel sulphide

Using untreated hydrocarbon fuels that may contain sulphur-bearing compounds for the operation of the SOFC can lead to the formation of Ni sulphide, with consequent degradation of the activity in the anodic catalyst [146, 147].

2.6.3.5 Loss of conductivity of the electrolyte

The ionic conductivity can be decreased by a phase change of the electrolyte or the diffusion of impurities or dopants [148-150]. Materials expanding at various rates lead to thermal mismatch, which is another common cause of failure [25]. This expansion should result in bending but instead results in cracking of planar cells, which do not tend to bend under compressive pressure. Delamination can also occur due to a thermal mismatch. This typically results in the isolation of ceramic layers from each other, causing a reduction in the contact area between the electrolyte and electrode which in turn lowers the performance of the cell even more.

2.6.3.6 Fuel impurities

A wide range of commercial fuels are suitable for SOFC applications, such as natural gas, gasoline, diesel hydrocarbon and alcohols. As mentioned above, three different reforming modes are possible using SOFC applications, these modes are external reforming, indirect internal reforming and direct internal reforming. It has to be considered, that the products of these reformings have hydrogen-rich fuels. However, they contain small quantities of sulfur-containing and other contaminants, including H_2S, CH_3SH, COS, Cl_2 and siloxane, which are strong poisons for the anodes of many fuel cell systems. The fuel impurities could cause degradation of cell performance and affect system durability [151, 152].

2.7 Degradation and durability studies of SOFC

Degradation of a fuel cell is calculated in percentage loss in performance parameter (voltage under defined load, as an example) per 1000 hours of operation. When the performance of a fuel cell decreases from long usage, this is called ageing. A life of 40,000 hours of a fuel cell means that it can be used commercially, for example, as for stationary power generation. The traget for degradation rates is to be as low as 0.1% per 1000 hours indicating a minimal power loss [153]. While many SOFC cells and stacks still face a sudden failure, steady degradations are a common cause of this failure.

Accelerated degradation testing (ADT), as one of the aging techniques, can be used to make the thermal and mechanical failures of the fuel cell even quicker. Redox conditions, cycles of load or thermal shock are examples of these techniques that results in rapid degradation of the fuel cell over long term testing [154]. Previous studies done in this area are presented below.

Researchers	SOFC (Anode, Electrolyte and Cathode)	Degradation rate per 1000 hours	References
Horita et al	Ni-ZrO_2, YSZ and $LaFeO_3$	1.5%	[155]
Komatsu et al.	NiO-SASZ, SASZ and LNF	1.4%	[156]
Park et al	NiO-CGO91, CGO91 and PSGF3737	7.7%	[157]

Tietz et al.	Ni-YSZ, YSZ and LSCF	0.9-1.5%	[158]
Mai et al.	Ni-YSZ, YSZ and LSCF	2 – 6%	[159]
Komatsu et al.	NiO-SASZ, SASZ and LNF	increased with increasing constant load	[160]
Simner et al.	Ni-YSZ, YSZ and LSCF	7%	[161]
Simner et al.	Ni-YSZ, YSZ and LSCF (coated)	7.5% at 750 ^{o}C 4.5% at 700 ^{o}C 0.0% at 650 ^{o}C	[162]
Yamaguchi et al.	NiO- GDC, GDC and LSCF-GDC	0.25% per 100 hours	[163]
Akhtar et al.	Ni-YSZ, YSZ and LSM	0.05 per 24 hours unacceptable for long-term	[164]

Cycling of SOFC is an increase in degeneration as the number of turns increase stated in literature [154, 165], so this method is also used for the accelerate degradation testing (ADT) to check the fuel cell durability. In addition, the process of cycling cannot be avoided throughout the operation of SOFC due to temporary situation leading to a constant state of shutdown. As the number of cycles increase, degradation may also increase progressively. There were three kinds of cycles stated during this process namely thermal cycling, redox cycling and electrical load cycling. The most dangerous of all is the redox cycling. According to Positive-Electrolyte-Negative (PEN) [154] the most cases of de-lamination and cracking was

noticed during redox cycling. The outcome of cycling was given in some researches [166, 167]. It was thought that the process of cycling also depends on the structure and shape of SOFC [154]. Due to differences in design in the case of tubular forms, there is more resilience to cycling when compared with the other planar type, as heat is allowed to pass both radially and axially [168]. Previous studies have shown the effects of cycling, but much more research need to be done in this area, because there are so many uncertainties in those studies (Liu and Jiao 439). This thesis will mainly focus on electrical/current load cycling.

2.7.1 Electrical Load Cycling

In the United Kingdom there is an increase demand of energy in the morning from 6:30- 8:30 hrs and in the evening between 18:00-20:00, due to the life style of consumers [169]. These times therefore comprise the time of maximum consumption for many UK households. The cycling loading of a SOFC illustrates a natural process and during this load cycling a cyclic manner is observed in the electrical cell. This phenomenon is used in cases of most of the SOFC appliances e.g. the CHP and other units that generates stationary power. In the evening the load on the system increases more than in any other part of the day, when the demand of power among the customers is relatively lower. The demands increase in peak hours and fall at other times of the day, which could have adverse effects due to this sudden fall in demand. Bujalski et al. [154] found details of the temporary activity of the RRFCS IP-SOFCs followed by load cycling. The chief impairment occurs due to load cycling in SOFC is the ageing of the electrode; this is the process in which there is an increase in the resistance of electrodes. There was degeneration in the function of electrical load cycles but a small increase in the resistance of electrodes was noted, which

contributed to the ageing process of the electrode. Electrical load cycling of SOFC has been tested by using AC impedance spectroscopy to study the mechanism of electrode ageing and to analyze it [170, 171]. The results of electrical load cycling of SOFC were low in comparison to either thermal or redox cycling.

2.7.2 Thermal Cycling

Thermal cycling is the mostly used type of cycling in the majority of the SOFC. This engages a variation in temperature, mostly ranges between the normal room temperature to the operating temperatures. SOFC undergoes abrupt changes during its operational phase. It works by a start-up and steady state of shutdown operations. As mentioned above, these cycles vary in terms of the design and internal architecture. Tubular and micro-tubular forms of SOFC show greater thermal cycling resilience in comparison with the planar or integrated ones because the tubular forms is capable of distributing the uniform radial and axial heat [154].

500 thermal cycles were performed by Adelen to micro-tubular SOFCs. The ramping rates were 200 ^{o}C per minute to the operating temperate of 800 ^{o}C in case of micro-tubular SOFC while 15 hours is required for the RRFCS IP-SOFC [154]. The starting time of micro-tubular SOFC ranging from the ambient temperature to the operating temperature (800℃) can even < 1 minute as against > 2 hours for a typical planar architecture.

This heat cycle could damage SOFC due to alternative expansion and contraction cycles in PEN (Positive-Electrolyte-Negative). These expansion and contractions are a greatest threat to the system. During the heat cycles the entire system showed expansion and contraction to relieve this stress at the junctions by its component

(anode) as in the case of redox cycling. Due to this, the material boundaries faced stress which thus caused failure of the system.

2.7.3 Redox Cycling

Out of the three cycles redox cycling is the most dangerous of all as it usually causes directly damage. It causes damage to SOFC anodes by gross cracking and delamination processes. In their cycles there is a displacement in volumes of SOFC. The anodes made of Ni/YSZ are more likely to experience re-oxidation due to the reason that Ni with oxygen has increase catalytic activity [172]. The anode-electrolyte junction shows extreme stress and constant strain of electrolyte as expansion occurs only on the anode.

2.8 Conclusion

This chapter has introduced the SOFC technology and the main problems that it faces. The most important of these is the cycling operation, which can irreversibly damage the cells, with cycling current load accelerating the degradation of the overall cell and thermal cycling causing mechanical damages to the fuel cell materials.

The SOFCs technology has the advantage that it can be operated with hydrocarbon fuels, such as methane, but this leads to the formation of carbon on the surface of the anode, resulting in degradation in overall performance.

An uninterruptable power supply (UPS) is designed for extensive, long duration application, specifically for stationary power of the SOFC [173]. In this case, it can be assumed that a supply cut-out, maintenance, or component failure could potentially cause the system to shutdown more quickly than expected. This will be taken into

account during this research. There are a number of challenges that need to be factored into operational procedure (which can then refer to gradient stress and delamination). Over a thermal gradient, stress increases further due to variations in the material CTE (Coefficient of Thermal Expansion) [174]. Delamination of cell materials and cracks often occurs due to thermal cycling and current load cycling for long term testing.

The furnace of the Advanced Measurement test station (SOFC station) is suitable for use with IP-SOFC, which does not need a mechanical load. Unfortunately, IP-SOFC with Ni/YSZ anode forms carbon deposition on the anode when using hydrocarbon fuel. The fuel mixture will be used to avoid serious carbon deposition to enable a mechanism study, as well as to increase performance and life time.

In this research, IP-SOFC will be used because it does not require mechanical load transmission inside the furnace, making this type of cell suitable for use in the standard Advanced Measurements test station (the SOFC station will be discussed in chapter three). In addition, they enable unrestrained thermal expansion, are sufficiently stable for long term testing and can also be fabricated by means of low cost ceramic fabrication processes [175].

The objective of the following chapters is to study the performance of the IP-SOFC under different operating conditions, including the effect of current load and thermal cycles and the impact of carbon deposition on the performance of the IP-SOFC, with the aim of simulating weeks and years of damage to understand the degradation mechanism of IP-SOFCs. This work seeks to contribute to ongoing investigations in this field by testing the durability of the IP-SOFC through the use of these

accelerated ageing techniques, as well as seeking to present a clear perception of the performance of the cell and their contribution to the use of alternative energy.

Chapter 3

Materials and Methods

3 Materials and Methods

This chapter seeks to describe the materials and the experimental procedures designed to investigate the performance of the IP-SOFC through accelerated aging techniques, including load and thermal cyclings. The aim of these approaches is to simulate long term accumulated damage and to measure degradation in the performance of fuel cells, thus providing reference for further improvement of IP-SOFCs in the future.

3.1 Test experimental apparatus

The test station used in this work is Fuel Cell Test Stand, Advanced Measurements Inc. (Canada), as shown below (see Figure 10). This station is capable of testing fuel cell stacks and taking measurements of up to 30 voltage inputs, 32 thermocouples, and with an electronic load capable of 100 W of power. The test station is equipped with Integrity software for the control of gas flow, operating temperature and humidity, in order to allow for a versatile, fully automated test system.

The test station operates through National Instrument Based Integrity software that can record and monitor the work of the device throughout its operation period. The station has sensors to detect gases (H_2 and CO), as well as to automatically shut down the operation should the concentration of H_2 and CO exceed the permitted limiting leak level. It has five inlets for gases, which are hydrogen, air, carbon monoxide, nitrogen and purge gas.

The most important component of the test station is its electric furnace, which is designed to be heated to a desired temperature up to 1200 ^{o}C. The furnace temperature is controlled through the software and continuously measured with

thermocouples. The interior dimensions of the furnace are 45 x 45 x 45 cm with a wall thickness that is typically 5 inches, which can maintain the skin temperature at less than 40 ^{o}C. This furnace is suitable for testing IP-SOFCs, which will be discussed in more detail in next section.

Figure 10: Fuel Cell Test Stand, showing the furnace and control system.

3.2 IP-SOFC

The IP-SOFC utilized in this project operates in the same way as a standard SOFC, which employs natural gas or hydrogen as fuel. The design of the IP-SOFC is based on a rectangular flat porous ceramic IP-SOFC, which enables a fuel supply to the anode. The IP-SOFC is screen printed with anode (Ni/YSZ based), cathode (LSM-based), electrolyte (YSZ) and interconnected layers. Each IP-SOFC comprises 30 cell pairs connected in series, each with a cell area of 6 cm^2 [29, 176]. The IP-SOFC is shown below in Figure 11 and Figure 12. In the test, the IP-SOFC is placed inside a special container so that air can be circulated around the cathode (Figure 13).

Figure 11: Integrated Planar Solid Oxide Fuel Cell (IP-SOFC) from Rolls Royce Fuel Cell Systems Ltd. (UK).

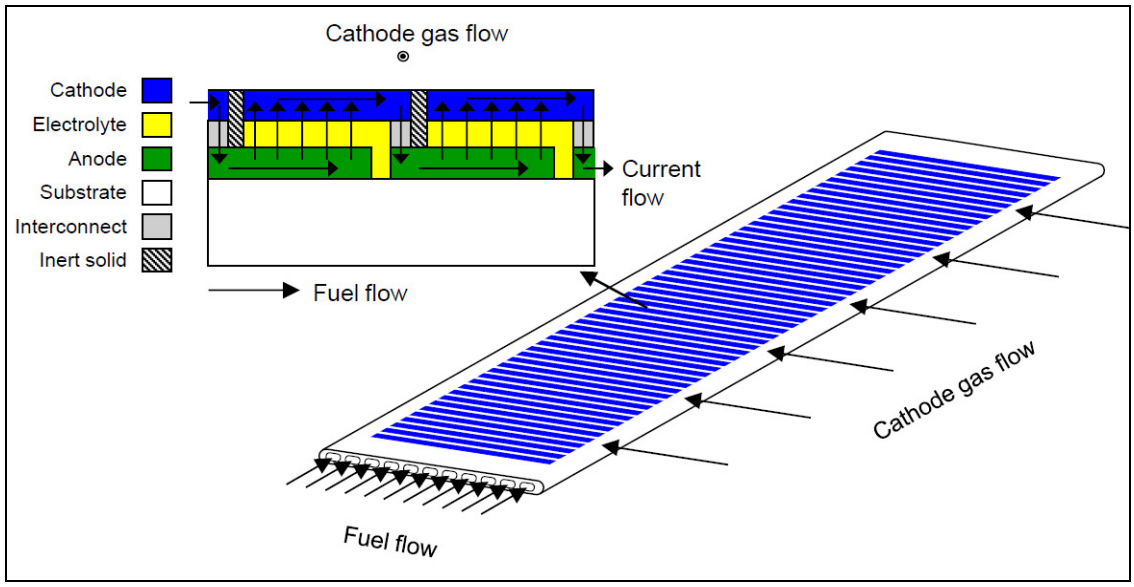

Figure 12: Schematic of IP-SOFC tube [177].

Figure 13: IP-SOFC inside a special container to circulate air around the cathode.

3.2.1 Microstructure of IP-SOFC

Scanning Electron Microscopy (SEM) was used to characterize the microstructure of the IP-SOFC. The characterization details will be discussed later in Section 3.4. Figure 14 shows the microstructure of a cross section area of the IP-SOFC, which consists of the anode, electrolyte, the cathode and porous ceramic support. The thickness of IP-SOFC components can be directly measured.

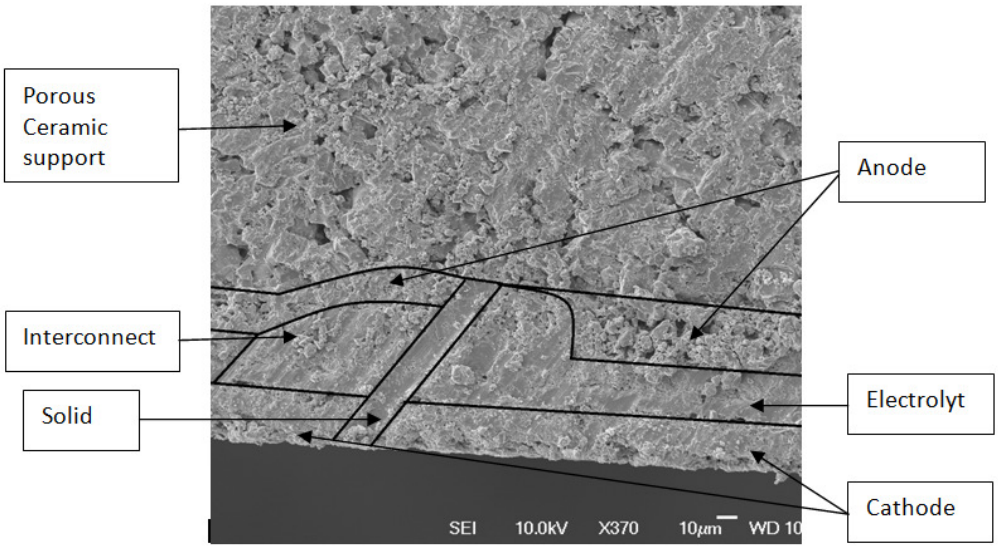

Figure 14: The cross section SEM image of the IP-SOFC.

Table 3 presents the thickness of the active IP-SOFC layers (anode, cathode and electrolyte), where the total thickness of the active IP-SOFC layers is approximately 80 µm. This limited thickness of tube (IP-SOFC) components is advantageous due to short current transferring paths.

Table 3: Thickness of IP-SOFC components.

Components	Thickness (µm)
Anode	40
Electrolyte	15
Cathode	25

3.2.2 Porosity of IP-SOFC

IP-SOFC tube consists of ceramic modules with electrochemical cells printed on the outer surfaces. The cathodes are supplied with oxygen from air flowing over the outside of the IP-SOFC, whereas the anode of IP-SOFC is in contact with the porous ceramic support. The feeding fuel is directed into a number of vertical channels

present inside the IP-SOFC, and reaches the anode side of the IP-SOFC by diffusion through the pores.

The Mercury porosimetry IV 9500 Series (introduced later in section 3.6) was used to characterize the porosity of a porous ceramic support, where finding the average pore diameter was 508.2 nm and porosity around 20.6 vol.%, as shown in Figure 15.

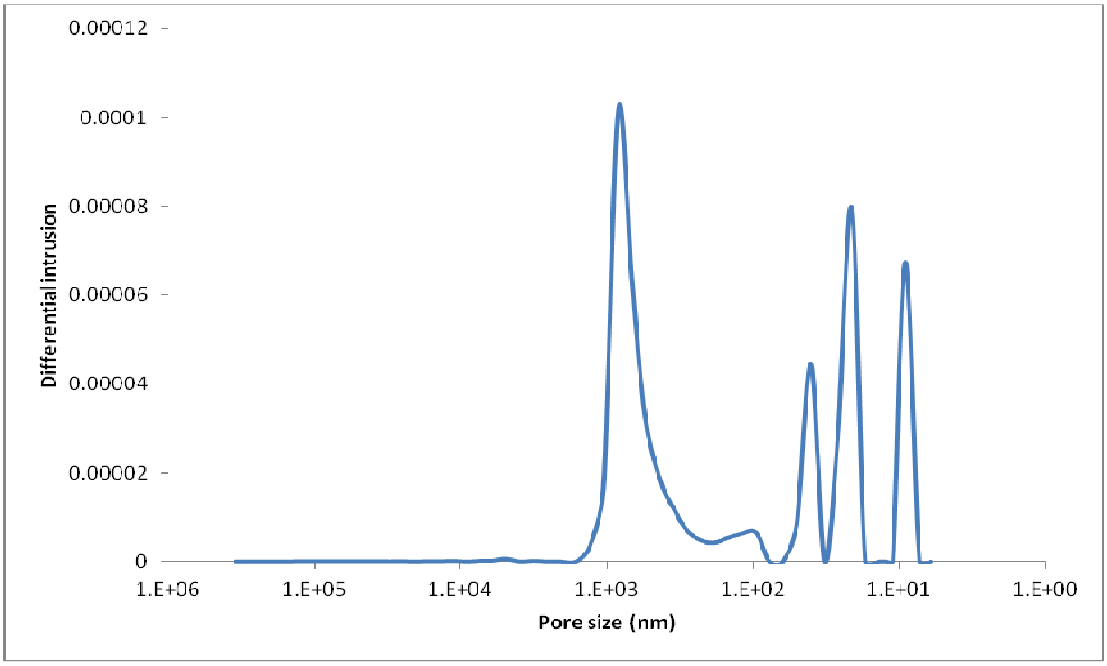

Figure 15: Porosity of the porous ceramic support in IP-SOFC.

As explained above, the fuel is driven by pressure or high flow rate along vertical channels to the anode side via pores. In all of experiments, a flow rate of 1.5 litres per minute of fuel was used, although the amount of fuel consumed in the reactions was substantially less than this amount. The actual amount of hydrogen delivered to the anode can be greater than determined by Faraday's law, as shown in Equation 3-1, but should never be less.

$$R_{H_2} = \frac{I_{cell}}{n * F} \qquad 3\text{-}1$$

I_{cell} is the total current leaving the IP-SOFC, n is molar number of electron and F is Faraday's constant.

In this case, the maximum current is 1.8 A, and the molar number of electron is 2, so, the hydrogen consumed is:

$$R_{H_2} = \frac{1.8}{2*96500} = 9.32*10^{-6} \text{ mole } H_2 \text{ per second}$$

The IP-SOFC consists of 30 cells and it is assumed that hydrogen is the ideal gas. The actual amount of hydrogen delivered to the anode is 0.376 liter per minute, which equals less than three times from the total amount used.

3.3 Mass spectrometer

The mass spectrometer (MKS Mini-Lab) was used to analyse the reaction products from the anode. It was also used to measure the carbon deposited during the tests when the IP-SOFC was operated with a mixture of fuel (hydrogen and methane). The mass spectrometer involves the use of a quadrupole mass filter, an electronic ion source, and a Faraday cup detector (see Figure 16).

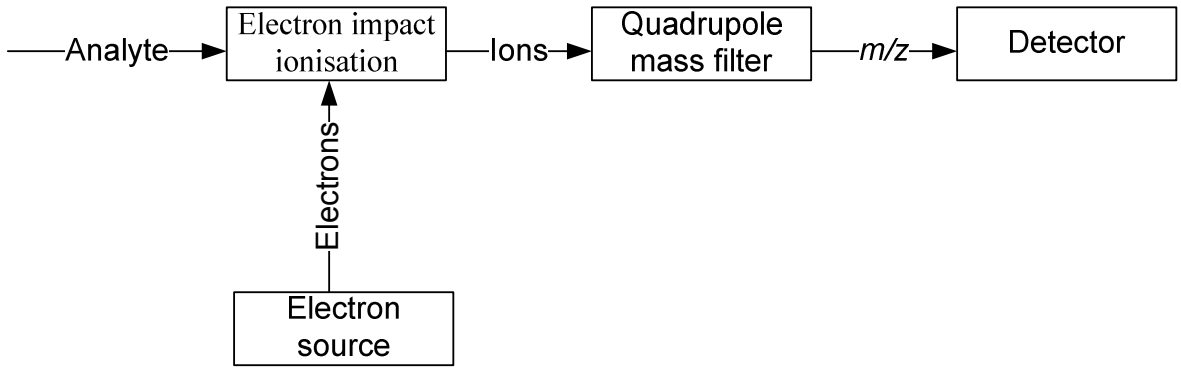

Figure 16: Simplified schematic diagram of a quadrupole mass spectrometer.

The process of electron ionization (EI) requires a wire filament to be heated

electrically. This produces an accelerated stream of electrons that flow towards the anode (typical energy 70eV). The movement of these electrons through incoming gas results in fragmentation and ionization.

The fragmented and ionized gas molecules pass into the quadrupole mass filter through the ionization chamber. The mass filter is comprised of four parallel rods with a DC potential arranged so that diagonally opposite rods have the same potential. In addition, radio frequency AC potential is applied to the rod pairs, causing the incoming ions to travel between the rods, through the centre of the quadrupole. The result of this arrangement is that the ions are filtered by the particular choice of AC and DC voltage. Only those of a given mass to charge ratio will pass through the quadrupole, as others will have unstable oscillations that result in their collision with a rod. This means that selective variation of the voltages can enable the detection of ions across a range of mass/charge ratios, which enables a comprehensive mass spectrum analysis to be obtained (this result is given in partial pressures). The ions that pass through the mass filter are detected by a metal Faraday cup. This detector becomes charged by the collision of ions with it. This is discharged to produce a small current that is equivalent to the charge on the captured ions.

The mass spectrometer results are given in partial pressures. For example, if there were components *a* and *b*, in a mixture, then if the amount of component *a* increases, its partial pressure would increase accordingly. This would mean that *b* would decrease, even though the absolute amount of *b* remains unchanged. The mass spectrometer scans the gases every 3 seconds, giving signal intensity at any 1 scan point. An example of this output is shown below in Figure 17.

The mass spectrometer requires calibration with known gases, such as helium or

argon. More information on these calibration mathematics can be found in section 3.3.1 as well as in the work of Dhir [118] and Lee [178] previously performed in our Group.

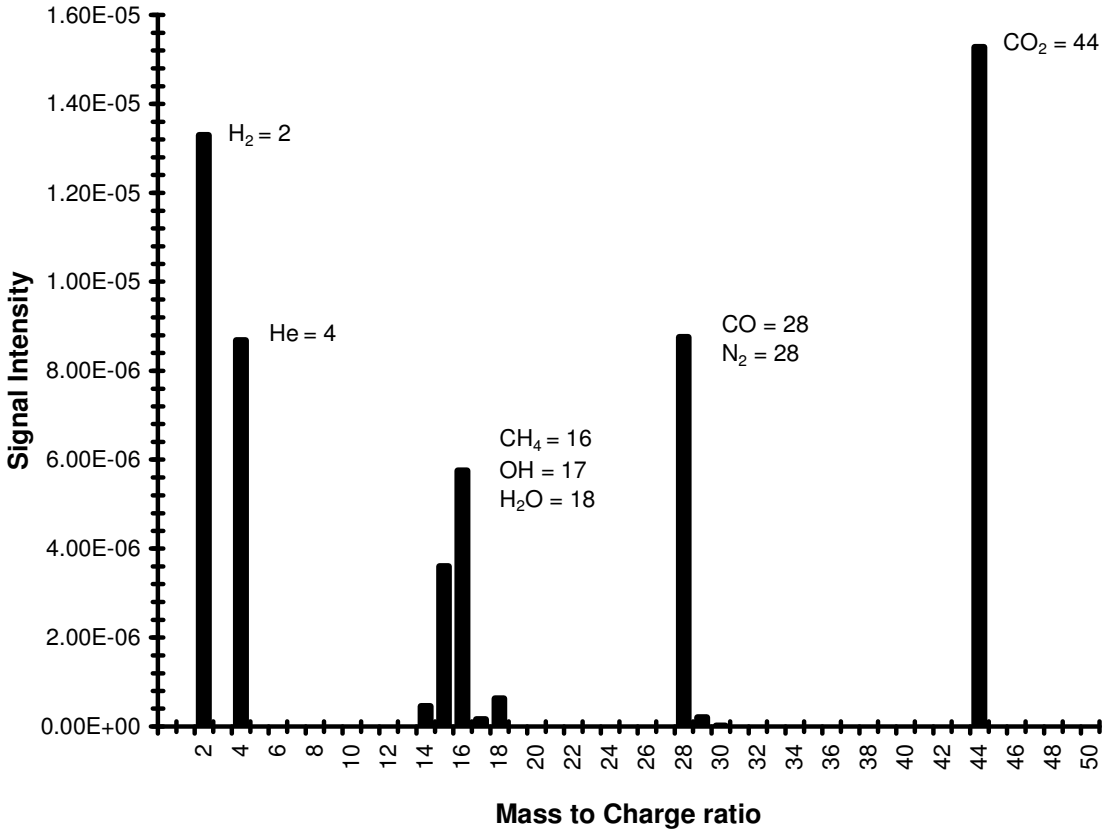

Figure 17: Typical mass spectrometer scan data for the reforming of methane [118].

3.3.1 Calibration Mathematics

It is necessary to perform a series of calibration experiments for the relevant gas composition in order to know the compositions of the actual mixture of gases, as was previously performed by Dhir [118] and Preece [179]. The compositions of these gases are therefore mixed with a known inert gas (helium or argon), at a constant flow rate. Once measurements are made relative to this reference, partial pressure measurements can then be converted into actual fractions or normalised against the reference gas, thereby giving an accurate absolute amount.

The mass spectrometer signal m_k will be given for the unknown gas component k which exists in a mixture of gases as a (percentage) fraction G_k. In order to obtain m_k corrected for relative ionisation sensitivity m_k [c] where a corrected factor (v_k) is required, the expression as Equation 3-2 is used:

$$m_k[c] = v_k . m_k \qquad 3\text{-}2$$

where:

$$v_k = \frac{G_k}{[m_k]^{cal}} \qquad 3\text{-}3$$

Here $[m_k]^{cal}$ is the mass spectrometer signal for a known gas fraction component k. If this component k exists with many other mass components, the percentage of component k, Equation 3-3, is expressed as follows:

$$G_k[c] = \frac{m_k[c]}{\sum_i m_i[c]} = \frac{m_k . v_k}{\sum_i m_i . v_i} \qquad 3\text{-}4$$

In these experiments, helium is used as component m_r. This denotes the absolute mass component and so all other signals are measured relative to this mass, as illustrated in Equation 3-5:

$$G_k[c] = \frac{m_k . v_k}{\sum_i m_i . v_i + m_r . v_r} \qquad 3\text{-}5$$

Factoring the bottom denominator of Equation 3-5 by v_r gives Equation 3-6

$$G_k[c] = \frac{v_k}{v_r} \frac{m_k}{m_r + \sum_i m_i . \frac{v_i}{v_r}} \quad 3\text{-}6$$

and, hence, the calibration factor k_i^r can be defined as shown in Equation 3-7:

$$k_i^r = \frac{v_i}{v_r} \frac{G_i}{[m_i]^{cal}} \frac{[m_r]^{cal}}{G_r} \quad 3\text{-}7$$

Hence,

$$G_k[c] = \frac{m_k . k_k^r}{m_r + \sum_{i \neq r} m_i . k_i^r} \quad 3\text{-}8$$

In these experiments, the mixture gases contain He, H_2, CH_4, CO and CO_2. The relevant gas fraction for these gases is as follows:

Helium:

$$G_{He}[c] = \frac{m_{He}}{m_{He} + m_{H_2} . k_{H_2}^{He} + m_{CH_4} . k_{CH_4}^{He} + m_{CO_2} . k_{CO_2}^{He} + m_{CO} . k_{CO}^{He}} \quad 3\text{-}9$$

Hydrogen:

$$G_{H_2}[c] = \frac{m_{H_2} . k_{H_2}^{He}}{m_{He} + m_{H_2} . k_{H_2}^{He} + m_{CH_4} . k_{CH_4}^{He} + m_{CO_2} . k_{CO_2}^{He} + m_{CO} . k_{CO}^{He}} \quad 3\text{-}10$$

Methane:

$$G_{CH_4}[c] = \frac{m_{CH_4} . k_{CH_4}^{He}}{m_{He} + m_{H_2} . k_{H_2}^{He} + m_{CH_4} . k_{CH_4}^{He} + m_{CO_2} . k_{CO_2}^{He} + m_{CO} . k_{CO}^{He}} \quad 3\text{-}11$$

Carbon dioxide:

$$G_{CO_2}[c] = \frac{m_{CO_2}.k_{CO_2}^{He}}{m_{He} + m_{H_2}.k_{H_2}^{He} + m_{CH_4}.k_{CH_4}^{He} + m_{CO_2}.k_{CO_2}^{He} + m_{CO}.k_{CO}^{He}} \quad 3\text{-}12$$

Carbon monoxide:

$$G_{CO}[c] = \frac{m_{CO}.k_{CO}^{He}}{m_{He} + m_{H_2}.k_{H_2}^{He} + m_{CH_4}.k_{CH_4}^{He} + m_{CO_2}.k_{CO_2}^{He} + m_{CO}.k_{CO}^{He}} \quad 3\text{-}13$$

In case a gas mixture does not contain the reference gas (helium in this experiment), it is possible to use a different component *s* in the gas mixture as the reference, without the need to re-obtain the calibration factor, which is related in Equation 3-14 as follows:

$$k_i^r = \frac{k_i^r}{k_s^r} = \frac{v_i}{v_r}\frac{v_r}{v_s} \quad 3\text{-}14$$

3.4 Scanning electron microscopy (SEM)

SEM was used to characterise the microstructure of the IP-SOFC and to study the morphology changes occurring on its surface. It was also used to measure the thickness of the anode, cathode and the electrolyte. The SEM analysis was undertaken using a Low Vacuum Scanning Electron Microscope (JEOL JSM-6060LV). This is a general purpose high-performance scanning electron microscope, operating at 20 kV.

3.5 Temperature Programmed Oxidation (TPO)

The total carbon deposition was measured and calculated using temperature programmed oxidation, a technique which has the ability to quantify the amount of carbon on the anode surface. This technique also enables the classification of the types of carbon that have been deposited on the anode surface.

At high temperatures, the amount of carbon deposited on the SOFC anode can be determined by exposing the anode to oxygen gas. The different types of carbon react to form CO and CO_2 at different temperatures, where CO and CO_2 levels were monitored by means of an on-line mass spectrometer. Amorphous carbon tends to oxidise around 300 ^{o}C, while graphitic carbon oxidises around 600 ^{o}C [180], as shown in Figure 18.

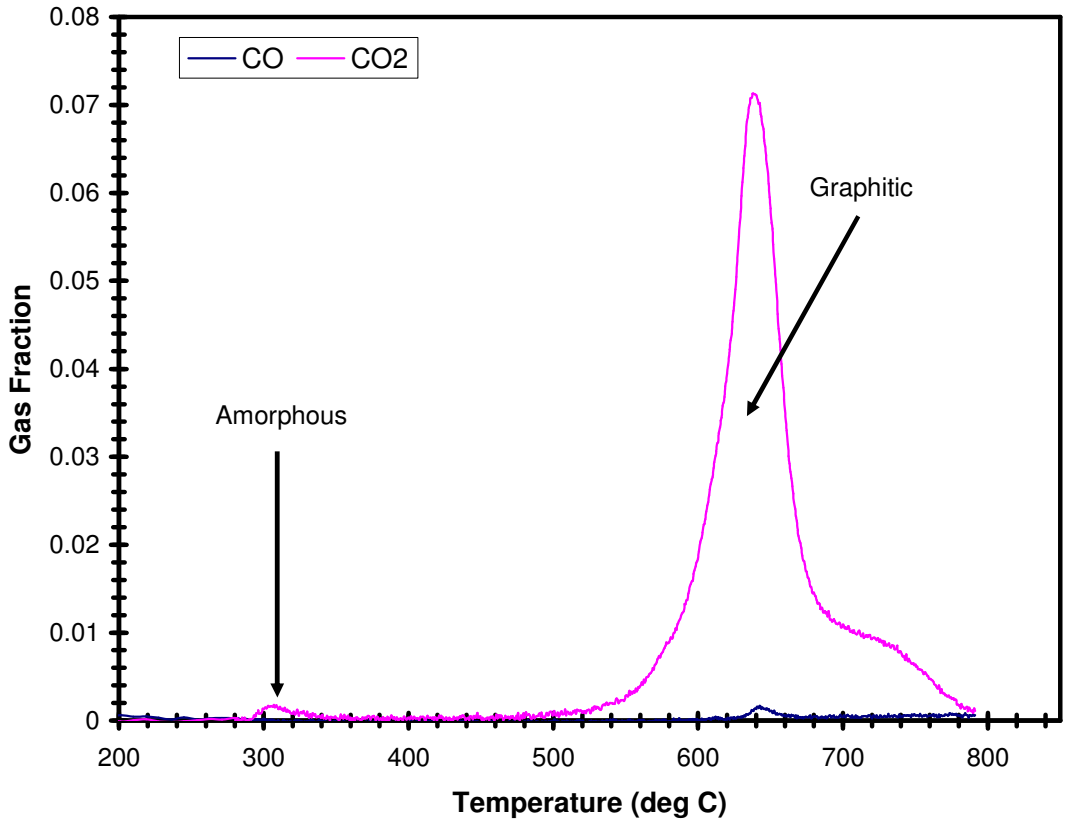

Figure 18: Typical TPO profile of a cell operated on methane [118].

The IP-SOFC (described in Section 3.2) which has been fed with a mixture fuel (mixed hydrogen and methane) was cut into small pieces. These pieces were then placed into a quartz glass tube, which was put into a furnace. This furnace, controlled by a Eurotherm^{TM} 2404 controller, was built using hollowed out thermal ceramic insulating fire blocks and with a ribbon of the heating element wrapped around ceramic rods. Two mass flow controllers (for helium and oxygen) were utilised to regulate the gas delivery to the quartz glass tube. This test rig is described in Figure 19.

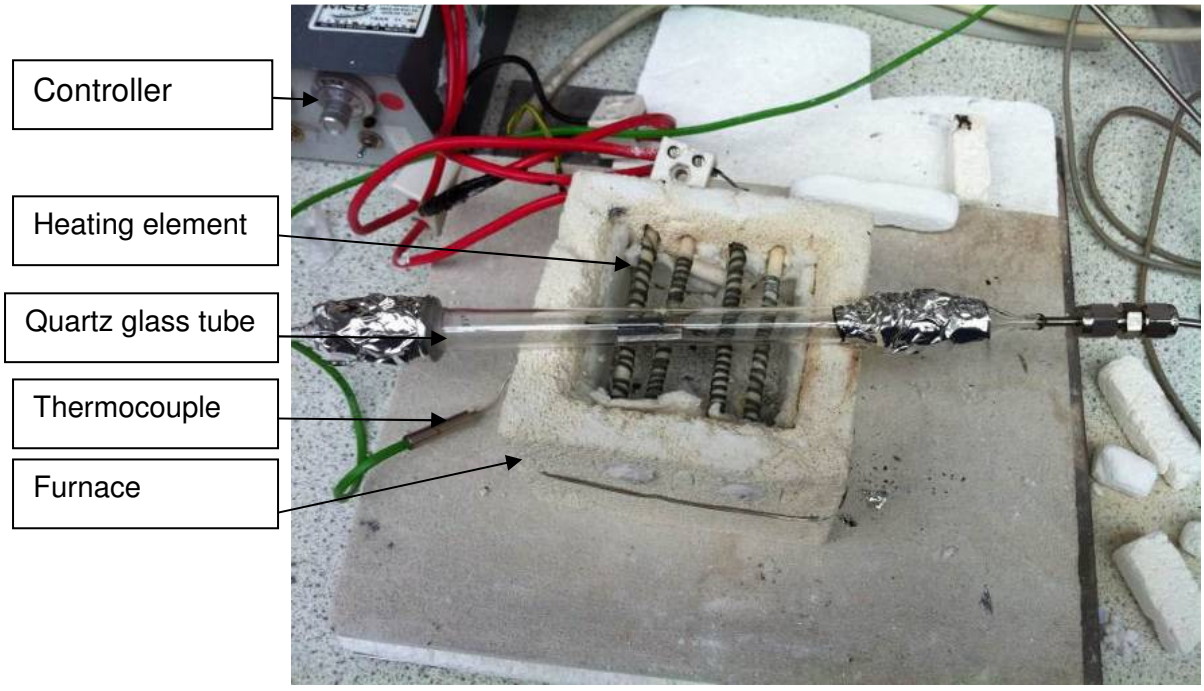

Figure 19: Temperature programmed oxidation kit.

In this experiment, a constant flow of helium (20 millilitres per minute) and oxygen (5 millilitres per minute) were supplied to the quartz tube containing small pieces of the IP-SOFC. The furnace was then heated to 800-900 ^{o}C at a rate of 10 ^{o}C per minute. The outlet of the quartz tube was connected to an on-line mass spectrometer in order to evaluate the exhaust gases.

This technique was calibrated by a known amount of carbon black to give a relationship between the amount of carbon oxidised and the area under the CO and CO_2 peaks. During this calibration, the CO and CO_2 peaks were similar, showing production of the same amount of CO and CO_2. However, most of the fuel cell, which contained carbon deposition, produced far more CO_2 than CO. This is partially because of the presence of oxygen and the way carbon is laid on the anode surface. If CO is formed, this is followed by further oxidation to CO_2. This is a rapid process and continues unless another nearby carbon atom can be oxidised instead [179].

In this thesis, only a methane mixture with hydrogen was studied as fuel. The amount of carbon that was formed on the anode surface is dependent on the operational condition of the IP-SOFC tube, such as temperature and the amount of mixture fuel (hydrogen and methane).

3.6 Porosity

A mercury porosimetry IV 9500 Series was used to characterize the porosity of a porous ceramic support material through the application of various levels of pressure to a sample immersed in mercury, a non-wetting liquid. The fundamental equation of mercury porosimetry is shown in Equation 3-15 [181].

$$\Delta p = \frac{2\gamma}{r} COS\theta \qquad 3\text{-}15$$

where, Δp is pressure difference between vapour and liquid phases, γ is surface tension of liquid phase, r is capillary radius and θ is wetting angle between liquid and solid phases.

It can be assumed that the pores in a ceramic support are cylindrical, enabling the Equation 3-15 to be converted into a simple working formula, where the contact

angle of mercury with most solids is approximately 140° and the surface tension of the mercury under vacuum and at a temperature of 20 °C is 0.48 Newton per meter, the gas pressure can be considered zero and using pore diameter instead of the pore radius, as shown in Equation 3-16.

$$d = \frac{1.470805}{P_L} \qquad 3\text{-}16$$

where P_L is liquid pressure [*Pa*]

3.7 High speed diamond cut-off saw

It is extremely hard to cut ceramic material. Figure 20 shows the high speed diamond cut-off saw that was utilised for quickly cutting valuable materials, such as rough crystals and ceramic. This machine was used to cut the IP-SOFC into small pieces for this study and the analysis.

Figure 20: High speed diamond cut-off saw [182].

3.8 IP-SOFC operating conditions:

Temperature: The IP-SOFC was tested at 900 ^{o}C, where the temperature of the furnace was increased to 900^{o}C at 1 ^{o}C per minute. At the end of each experiment, the temperature of the furnace was cooled to room temperature at a rate of 1 ^{o}C per minute too.

Flow rate*:* The flow rate of hydrogen or mixture gas (hydrogen and methane) was 1.5 litres per minute, whereas the flow rate of oxidising gas (air) was 5 litres per minute.

3.9 Anode Reduction

The reduction process must be applied to the SOFC before the first time testing, because the anode consisted of NiO-YSZ, which must be converted into Ni-YSZ cermet to provide catalytic performance. Here, two different types of reduction method were examined:

- High flow rate reduction
- Low flow rate reduction.

Both of these reductions were conducted at 900 ^{o}C using pure hydrogen as the fuel.

3.10 Current load cycling

The current load cycling test was conducted on the IP-SOFC with pure hydrogen or mixed fuel at 900 ^{o}C; a steady operation at 1 A was commenced and continued for 48 hours, after which the load was decreased to 0 A. The current load cycling was repeated 7 times for each operation. The IV curves were recorded for every current load cycle in order to assess the performance (degradation) of the IP-SOFC.

3.11 Thermal cycling

The thermal cycling test was conducted on the IP-SOFC with pure hydrogen. The IP-SOFC was heated to 900 ^{o}C at a rate of 5 ^{o}C per minute, after which the system was cooled down to 300 ^{o}C. This process was repeated several times. The IV curves were recorded for every thermal cycling.

3.12 Fuel Mixture

The fuel mixture test has been conducted on the IP-SOFC at 900 ^{o}C with mixed hydrogen and methane as a fuel. Two kinds of experiments have been carried out, as follows:

- **Experiment I:** The IP-SOFC was operated using four different methane contents in the fuel mixture (H_2 and CH_4) at 900 ^{o}C in order to investigate its degradation behaviour. The methane content of the fuels varied from 5% to 20%, with the remainder being hydrogen. The initial IV curve for pure hydrogen was taken as a reference and then the IV curves were recorded for each fuel mixture run.

- **Experiment II:** The IP-SOFC was fed with a fuel of 95% hydrogen and 5% methane at a flow rate of 1.5 litres per minute. Steady operation at 1 A commenced for 48 hours, after which the load was decreased to 0 A. This process (current load cycles) was repeated 7 times. The IV curves were recorded for each current load cycle, in order to assess the performance (degradation) of the IP-SOFC. After every 7 load current cycles, the fuel was changed from a mixture to pure hydrogen for 48 hours, after which time the IV curves were recorded for comparison purposes. Following this, the mixed fuel

changes to 80% hydrogen and 20% methane, and repeat same sequence which applied on first mixed fuel.

3.13 Conclusion

This chapter has presented a detailed outline of the design of the IP-SOFC, testing procedures and equipment in this thesis, in addition to the chosen methods for calibration and analysis of results.

Chapter 4

Anode Reduction Process

4 Anode Reduction Process

This chapter presents the experiments into two different methods of anode reduction with pure hydrogen. These experiments used a varying fuel flow rate and time (short and long time periods). This reduction process from NiO to Ni-metal enables the catalytic ability to fuel, but also results in changes to the volume and porosity of the anode material. Due to shrinkage of the NiO particles, the porosity of Ni-YSZ is higher than that of NiO-YSZ.

This chapter discusses two different methods of reduction conditions, and examines the effect that these variations have on anode activity and IP-SOFC performance.

4.1 Reduction methods

The reduction process was completed on three IP-SOFCs noted as IP-SOFC-1, IP-SOFC-2 and IP-SOFC-3. Two different types of reduction method were examined: high flow rate reduction and low flow rate reduction. These reduction techniques were chosen to identify the optimal conditions of different flow rates using pure hydrogen. Both of these reduction conditions can change the properties of anodes and so a discussion will be provided regarding the changes in anode properties and the effect that this had on the three IP-SOFCs.

4.1.1 High flow rate reduction

This reduction process applied an increase in hydrogen flow rate by 0.10 litres per minute and a corresponding decrease in nitrogen flow rate by 0.10 litres per minute. The flow rate change in each step takes 2 minutes, and the total of flow rate of gases (H_2 and N_2) was equal to 1.5 litres per minute in all steps of anode reduction. Completion of all the steps means that the reduction process takes 30 minutes, as

shown in Figure 21. This reduction process was applied on IP-SOFC-1 and IP-SOFC-3. The cell IP-SOFC was subsequently fed by hydrogen, at 3% humidity and a preheated inlet line at 120 °C. These parameters were in accordance with the operating conditions stipulated by the manufacturers. Reduction in this process took place via gradual introduction of hydrogen across a reduction profile.

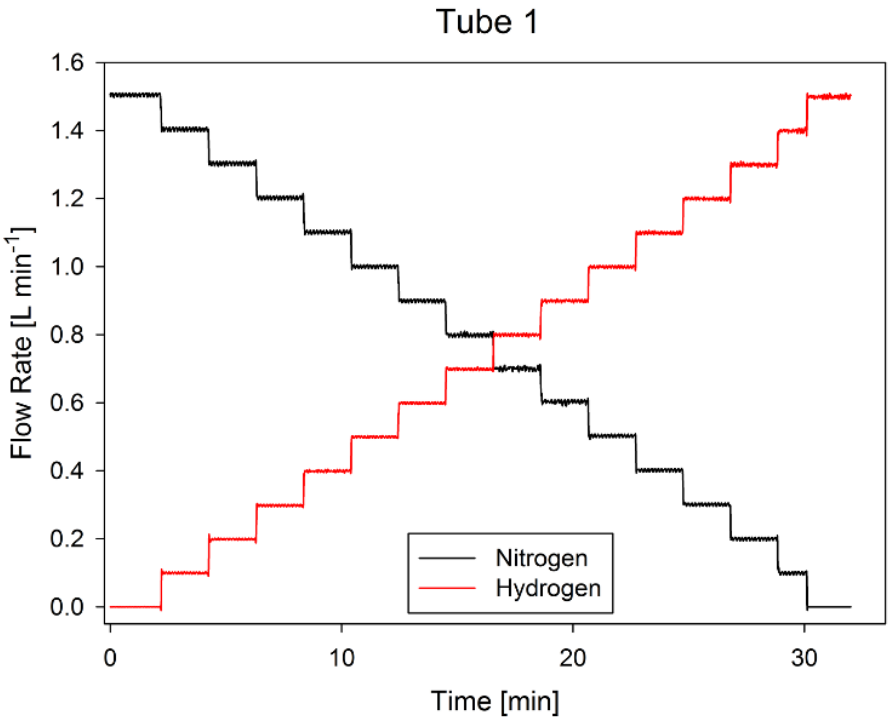

Figure 21: The first reduction process which increased hydrogen by 0.10 litres per minute.

4.1.2 Low flow rate reduction

Figure 22 shows the second reduction process. This reduction process was sustained with an increase in hydrogen flow rate by 0.05 litres per minute per step, while simultaneously decreasing the nitrogen flow rate by 0.05 litres per minute at each step. As in the first reduction, each step took 2 minutes and the total flow rate of gases (H_2 and N_2) was equal to 1.5 litres per minute. It therefore took 60 minutes

to complete all the steps of the reduction process applied on IP-SOFC-2. This anode reduction technique took 30 steps, whereas the previous took only 15 steps. The cell IP-SOFC was subsequently fed by hydrogen, with 3% humidity and preheated inlet line at 120 ^{o}C.

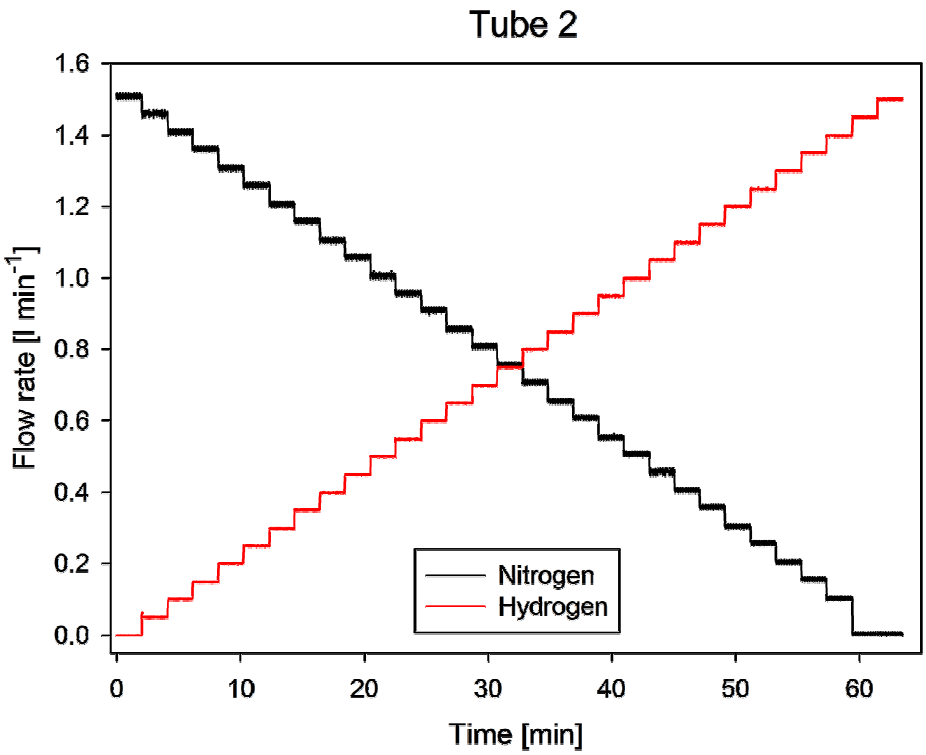

Figure 22: The second reduction process which increased hydrogen by 0.05 litres per minute.

The difference between these two methods is primarily dependent on the amount of the flow rate of hydrogen gas to the IP-SOFC, with a double flow rate being applied in the first method, compared to the second method. This increases the duration of anode reduction in the low flow rate reduction method in comparison with the high flow rate reduction method. This means that while the first method took 30 minutes, the second method took 60 minutes to finish the anode reduction processes of the IP-SOFCs.

4.2 Experimental procedure

The initial stage in this experiment involved clearing the dust from the path of gases, which was achieved by flowing nitrogen for 300 seconds. After then the temperature of the furnace was increased to 900 ^{o}C, at a heating rate of 1 degree per minute without fuel, air or safe gas (5% hydrogen toped up with nitrogen). The system was then kept running to stabilize for about one hour. After that, the nitrogen at the anode and air at the cathode was fed to the IP-SOFC. The flow rate of the nitrogen was set to 1.5 litres per minute and air to 5 litres per minute for one hour, after which the anode reduction techniques were applied on the IP-SOFC. After the anode reduction process, the IP-SOFC was kept running for 24 hours in order to stabilize the process, and then the first IV curve was recorded. The IV curve was comprised of the gradual increase of the load, from 0 to 1.8 A at 0.1 A steps. The first reduction method was applied on IP-SOFC-1 and IP-SOFC-3, and the second reduction method was applied on IP-SOFC-2.

4.3 Results and discussion

Two different methods of anode reduction have been examined with regards to three IP-SOFCs, the high flow rate and the low flow rate, respectively.

4.3.1 High flow rate

Figure 23 shows the IV curve for the initial result for IP-SOFC-1 and IP-SOFC-3, which have been operated with high flow rate of anode reduction. The results of this test were obtained after the reduction process and one day of testing (as described in 4.1.1). It can be seen that the open circuit voltage (OCV) was almost the same for IP-SOFC-1 and IP-SOFC-3. The initial OCV values were 31.42 V and 31.62 V for IP-

SOFC-1 and IP-SOFC-3, respectively. The difference in the values of OCV between IP-SOFC-1 and IP-SOFC-3 were very small, at only around 200 mV. As each IP-SOFC contains 30 cells, this difference in values is less than 7 mV for each cell and thus can effectively be ignored.

The voltage recorded at a high current density of 0.3 A per cm^2, with the cell current of 1.8 A, was measured as 22.96 V and 23.44 V for IP-SOFC-1 and IP-SOFC-3, respectively. The voltage difference was only ca. 2% and thus demonstrating the good quality consistence between each IP-SOFC.

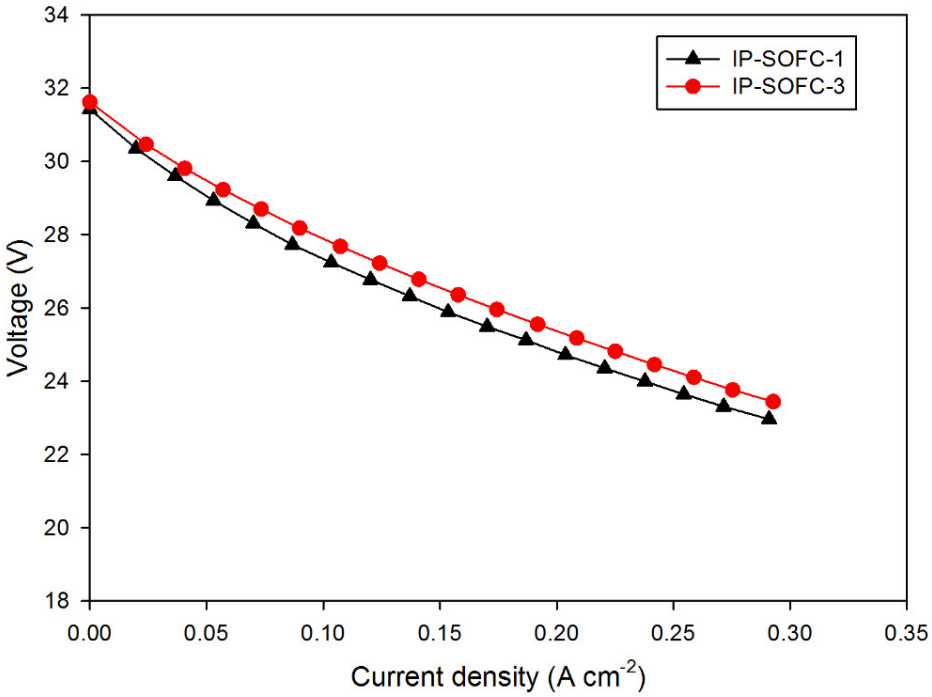

Figure 23: The initial IV curve for IP-SOFC-1 and IP-SOFC-3, reduced at high flow rate.

4.3.2 Low flow rate

Figure 24 shows the initial result of voltage vs. current density (IV curve) for IP-SOFC-2. These data were measured in hydrogen (1.5 litres per minute) and air (5 litres per minute) at 900 ^{o}C after running for 24 hours. In this case, the anode reduction which was applied to IP-SOFC-2 took 60 minutes to complete. The initial OCV was 31.21 V, and the voltage was 21.68 V at the current density 0.3 A per cm^2.

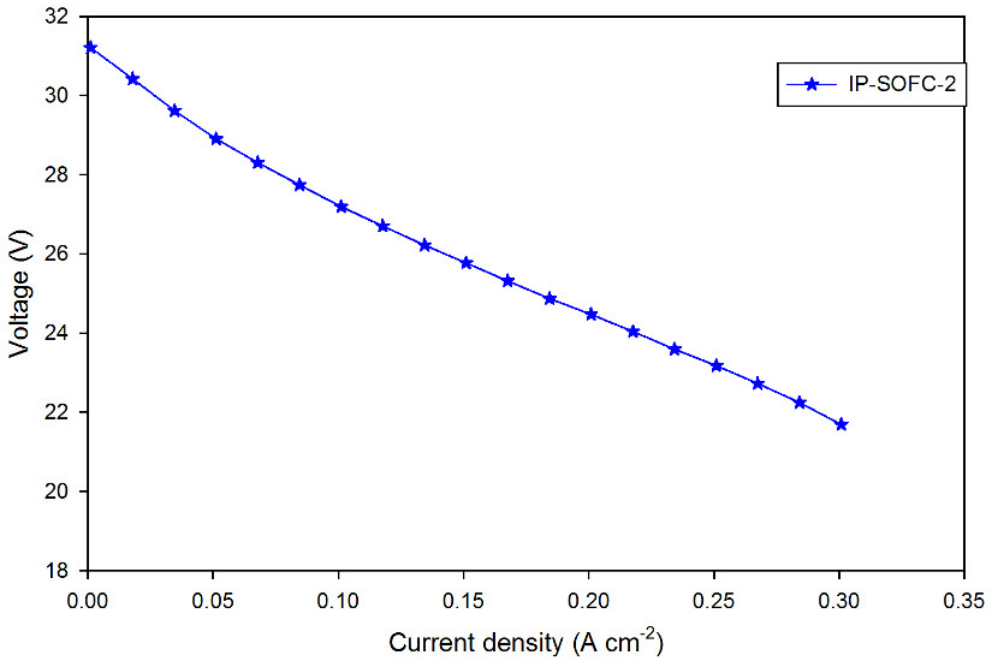

Figure 24: The initial IV curve for IP-SOFC-2, reduced at low flow rate.

4.4 Comparison of the two reduction methods

Figure 25 and Table 4 show the comparison results of the two reduction processes. The OCV is nearly constant for all three IP-SOFCs. The difference in the values of OCVs between the three IP-SOFCs is very small, at between 240 mV and 450 mV. This difference in voltage was recorded in the first IV curve, after the IP-SOFC had been left running for 24 hours to stabilize. It is worth noting that, even after 225 hours

of operation, the OCV of the three IP-SOFCs was still almost identical at around 31.45V.

At a high current density of 0.3 A per cm^2, there was a slightly lower initial voltage of IP-SOFC-2, which was noted in the second anode reduction process with low flow rate reduction. In IP-SOFC-2, the initial voltage was recorded at 21.68 V and decreased at the 1st step, which was then followed by a gradual increase in voltage. During the first 200 hours, the performance of IP-SOFC-2 improved slowly by 1.5%. In addition, the initial voltage value in IP-SOFC-1 and IP-SOFC-3, used in the first anode reduction with high flow rate, started at the same point (22.96 V), but the voltage for IP-SOFC-3 increased by a small amount and then continued to stabilise with IP-SOFC-1. Each IP-SOFC consists of 30 cells and the equivalent voltage was 0.723 V for each cell in IP-SOFC-2, whereas the equivalent voltage was 0.765 V for each cell in IP-SOFC-1and IP-SOFC-3. The voltages for all three IP-SOFCs were extremely similar, at around 22.77 V after 225 hours of operation.

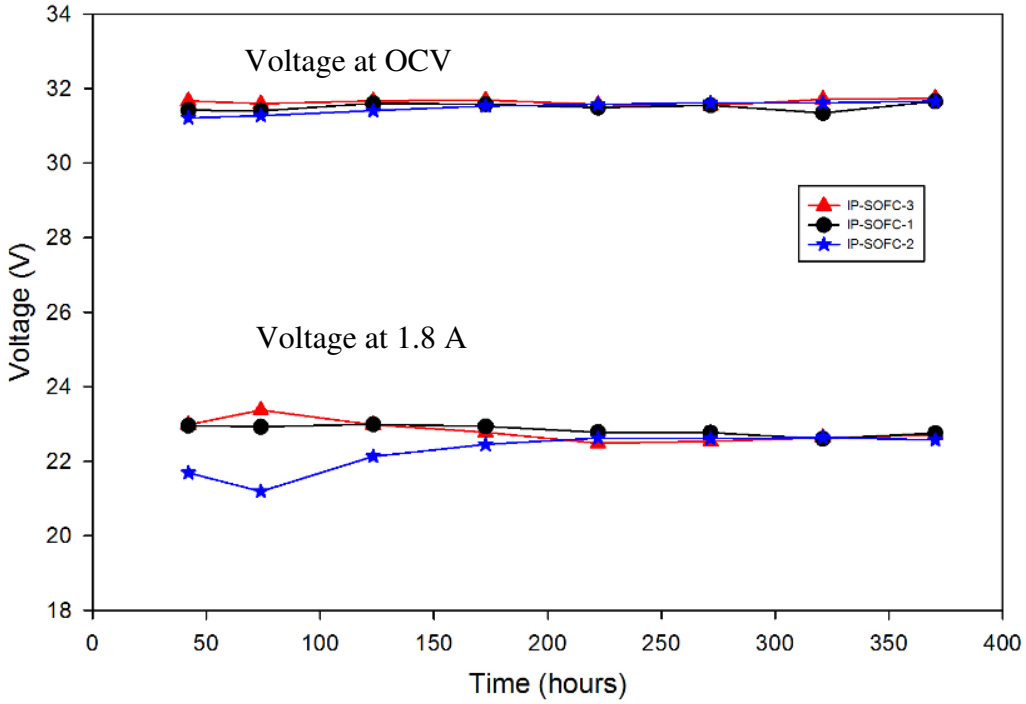

Figure 25: Voltage at OCV and 0.3 A per cm^2 (1.8 A for the cell) with different reduction process.

Table 4: Comparison of the voltages for the initial anode reduction results.

	OCV	Voltage at 1.8 A
IP-SOFC-1	31.42	22.96
IP-SOFC-2	31.21	21.69
IP-SOFC-3	31.62	23.44

The previous results show a similar result obtained for both methods. The OCVs of the three IP-SOFCs were almost equal in values which were between 31.2 and 31.6 V, with only a slight difference at the beginning of IP-SOFC-2 at the high current density as compared with two other IP-SOFCs. After the first 250 hours there was no significant change in cell voltage, no matter at OCV or at high current density of 0.3 A per cm^2, indicating that the flow rate in anode reduction process does not bring large difference to IP-SOFC performance. Furthermore, this extremely small difference between the three IP-SOFCs, and the highly stable voltages within nearly

400 hours confirms the high reproducible quality of these IP-SOFCs, indicating that the following results obtained on different IP-SOFCs can be accurately compared each other,

4.5 Conclusions

An examination has been made into the effects of two reduction techniques, high flow rate and low flow rate, on the performance of IP-SOFC.

The anode reduction process was clearly shown to not affect the structure of anodes at low and high flow rate reduction, where initial voltages at OCV or high current density of 0.3 A per cm^2 for three IP-SOFCs were almost identical. Besides this, during long period tests (nearly 400 hours of operation), three IP-SOFCs showed quite similar stable OCV and voltage at 0.3 A per cm^2, respectively, indicating the high reproducible quality of this kind IP-SOFC.

Chapter 5

Cycling durability studies of IP-SOFC

[1] Extracted from: Almutairi, G., K. Kendall, and W. Bujalski, Cycling durability studies of IP-SOFC. *International Journal of Low-Carbon Technologies*, 2012. 7(1): p. 63-68.

5 Cycling durability studies of IP-SOFC

A major obstacle to the implementation and widespread use of SOFC is that the cells can be damaged irreversibly during cycling operation in practical applications. The function of a cycling test is therefore to investigate fuel cell stability and degradation behaviour under this kind of non-steady operating condition in order to predict the lifetime of a SOFC. Cell quality tends to degenerate at greater numbers of cycles.

This work therefore seeks to test the behaviour of three RRFCS IP-SOFCs (IP-SOFC-1, IP-SOFC-2 and IP-SOFC-3), after the anode reduction process have been performed to them as discussed above in Chapter 4. The durability test of the IP-SOFC in this work was implemented through the use of accelerated ageing techniques, including current load cycling and thermal cycling. The effect of two differing reduction techniques on the long term performance of IP-SOFC tubes were further evaluated through these tests.

5.1 Experiment on current load cycling

After the reduction process, the cells operated under electronic load at 0 A for 1 day until the OCV stabilized. The OCV was recorded and then the first IV curve was drawn from 0 to 1.8 A, which constitutes the initial results. The IP-SOFCs were subsequently cooled down to 400 ^{o}C at a rate of 1 ^{o}C per minute, then pure hydrogen was changed to safe gas of N_2 at 1.425 litres per minute and H_2 at 0.075 litres per minute to enable further cooling to 60 ^{o}C.

The furnace was reheated to 400 ^{o}C at a rate of 1 ^{o}C per minute with safe gas N_2 at 1.425 and H_2 at 0.075 litres per minute, and the fuel was changed to pure hydrogen. After then the furnace temperature was increased to 900 ^{o}C at a rate of 1 ^{o}C per

minute. When the IP-SOFC reached 900 ^{o}C, the IP-SOFCs were stabilised at OCV for 24 hours. An IV curve was derived by cycling from 0 A to 1.8 A, and then looped back to 0 A. The applied current was restarted and steady operation was commenced at 1.0 A current load cycling. In order to track the performance of the IP-SOFCs, IV curves were drawn every 48 hours. The process was stopped after the application of 7 current load cycles and the performance of IP-SOFC was assessed. The SOFC Test Station was then switched off and restarted under the same conditions as above. These processes were repeated seven times, following the same operating conditions described above. The IV curves were taken at every current load cycle. This stage was applied to IP-SOFC-1, IP-SOFC-2 and IP-SOFC-3 with current load cycling. Figure 26 shows a part of sequence that was applied on IP-SOFC tubes for all processes that involved a start-up and shut-down of the station test, IV curves and current load cycling.

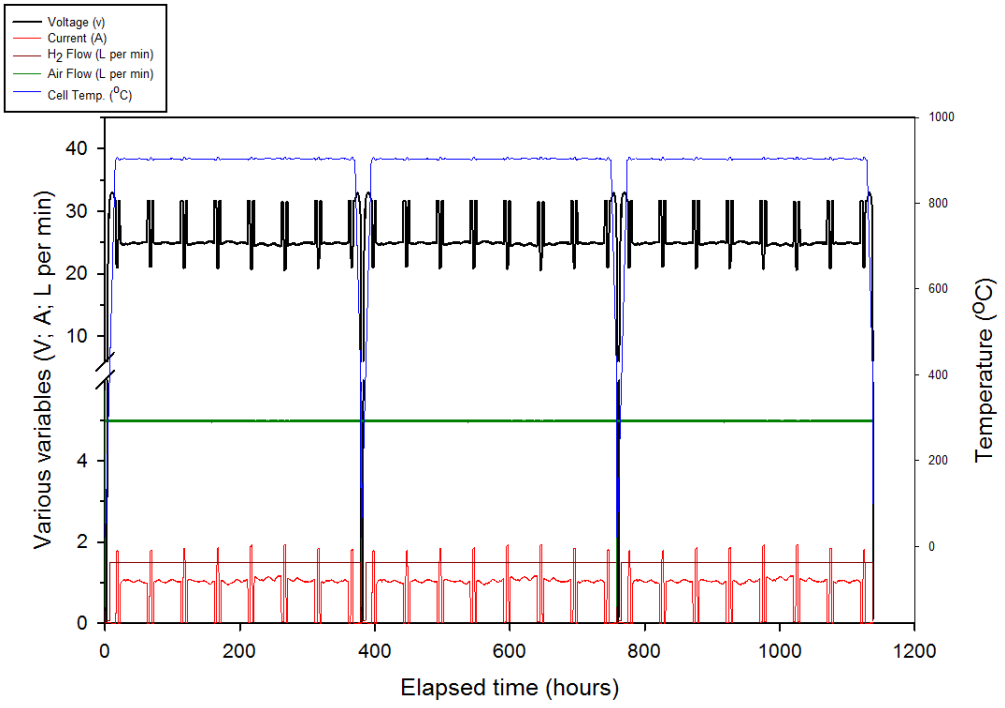

Figure 26: Durability test conditions for IP-SOFCs.

From Figure 25 in Section 4.4, the initial value for OCV and the voltage under maximum current (1.8 A) gives the perception that the IP-SOFC was not affected during the initial stages of operation (the first 100 hours of operation, as a steady state condition), except the IP-SOFC-2 which was affected by reduction techniques.

5.1.1 IP-SOFC-1

The durability study of IP-SOFC-1 was operated over 1200 hours, including 26 current load cycling and 3 shutdowns. These results were obtained by running on pure hydrogen and air, with flow rates of 1.5 litre H_2 per minute and 5.0 litre air per minute at 900 ^oC, respectively.

As can be seen in Figure 27 and Figure 28, the OCV of IP-SOFC-1 remained stable at 31.8 V throughout the testing phase, which was equivalent to 1.06 V for each single cell. This phase amounted to 1200 hours, including three restarts and shutdowns of the test station, and 26 IV curves where each IV curve is considered as a current load cycle.

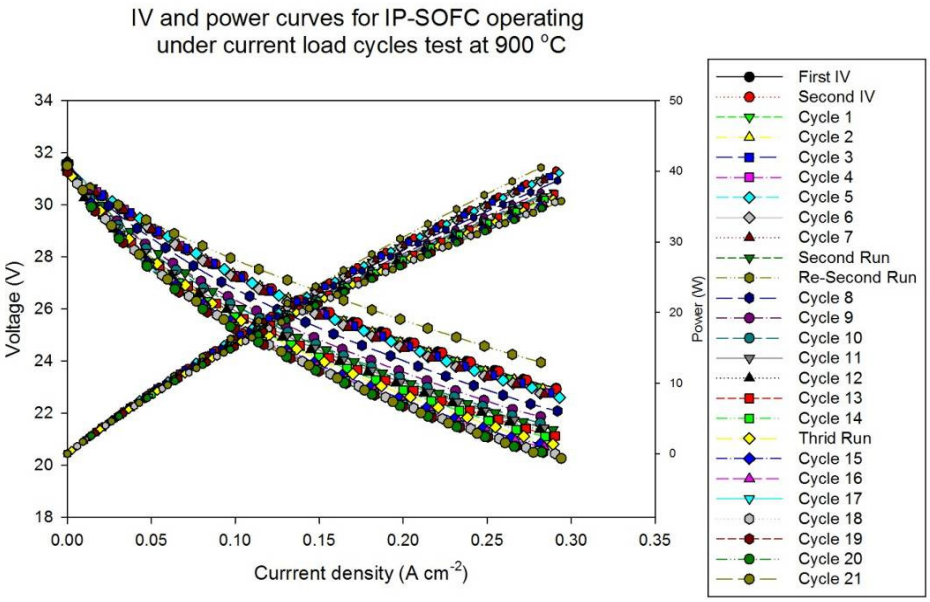

Figure 27: I-V and power curves for IP-SOFC-1.

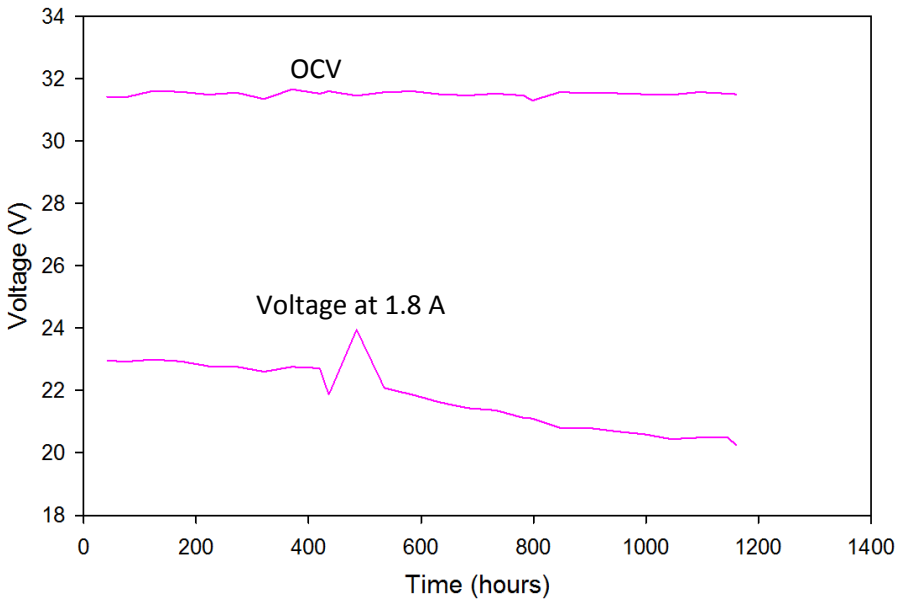

Figure 28: OCV and voltage at maximum current 1.8 A vs. time for IP-SOFC-1.

A slight decrease was recorded in the value of the voltage at maximum current of 1.8 A (with current density 0.3 A per cm^2). The voltage produced was close to around 22.96 V. This decline likely occurred as a result of the impact of current load cycles with restart and shutdown of the test station, affecting the performance of the cell during the 1st 436 hours. The voltage dropped by approximately 240 mV during this period.

After this point, the air supply was unexpectedly cut off from the station due to an accident of the overheating of the air compressor, resulting in the closing of gas supplies in station for safety reasons. The furnace and IP-SOFC-1 testing continued to work at a temperature of 900 °C for 16 hours at this condition before cooling down. IP-SOFC-1 did not appear to have been adversely affected by this situation, showing no obvious cracking or damage of the cell through visual inspection.

However, the working and cooling of the cell without gas for long periods of time could have resulted in the expansion of anode due to the oxidation of the nickel to nickel oxide, in which case restarting the IP-SOFC in a gas-rich environment could have also caused accelerated reduction due to the possible defects in the composition of the IP-SOFC material [154]. The destruction of an anode caused by the cut off of the fuel supply made the anode to undergo a relatively high partial pressure of oxygen. Additionally, this oxygen may end up oxidising the nickel component of the anode which forms into NiO, resulting in a higher volume than the surrounding scaffold [14]. The drawn load will differentiate as long as the stack is live and the electrocatalyst is needed for the current cycling. Any electrochemical defects will then be amplified by the faster cycling [183], and this was approved by the following cycling.

Every IV curve and power curve considered current load cycling with restart and shutdown as shown in Figure 27, demonstrating that there was relatively small decline in the performance of the cell over the first 436 hours, as a growth was seen in the number of current load cycles due to increased Ohmic resistance during operation. The maximum power of IP-SOFC-1 was 42 W, which was achieved at a current density of about 0.3 A per cm^2, after which it started to decline as a result of the accident mentioned earlier.

The cell voltage degradation rate (DR) was defined as the initial voltage and the voltage measured at operating time (t) which are considered V_o and V_t, respectively, as in the Equation 5-1 below [184]:

Cell voltage degradation rate (%) $$DR\% = \frac{V_o - V_t}{V_o * (t - t_o)} * 100\% \quad \text{5-1}$$

Figure 28 and Table 5 show the durability study over 1200 hours for OCV and voltage under applied current 1.8 A. The degradation rate of IP-SOFC-1 was between 1 and 4% during first 436 hours of operation after the afore-mentioned issue occurred. As a result, the degradation rate increased to around 10% during the 1200 hours operated.

Table 5: Electrochemical performance of IP-SOFC-1 for cycling 1-26.

Time (hours)	Cell voltage at 0 A (Volt)	Cell voltage at 1.8 A (Volt)	Degradation rate (% per 1000 hours)
24.00	31.42	22.96	0.00
73.91	31.40	22.92	2.14
123.32	31.60	22.92	1.28
172.73	31.58	22.78	4.56
222.13	31.49	22.78	3.55
271.54	31.55	22.77	3.10
320.94	31.34	22.60	4.84
370.35	31.66	22.76	2.37
419.75	31.52	22.72	2.53
436.00	31.60	21.87	10.93
534.81	31.57	22.08	7.16
584.22	31.60	21.87	8.16
633.63	31.50	21.62	9.20
683.03	31.46	21.43	9.73
732.44	31.52	21.37	9.48
781.84	31.46	21.12	10.23
798.09	31.30	21.10	10.15
847.50	31.57	20.80	11.10
896.90	31.53	20.80	10.49
946.31	31.53	20.69	10.45
995.71	31.50	20.60	10.32
1045.12	31.48	20.44	10.50
1094.53	31.57	20.49	9.83
1143.93	31.52	20.51	9.33
1160.18	31.50	20.26	10.14

The black line in Figure 29 shows the linear fit for the voltage obtained at maximum current of 1.8 A, between 24 and 436 hours operated. This region was not affected

by the problem mentioned above. The following Equation 5-2 shows the rate of decline in IP-SOFC-1:

$$V_t = -0.0008t + 23 \qquad 5\text{-}2$$

where V_t is the measured voltage at maximum current of 1.8 A and t is time in hour.

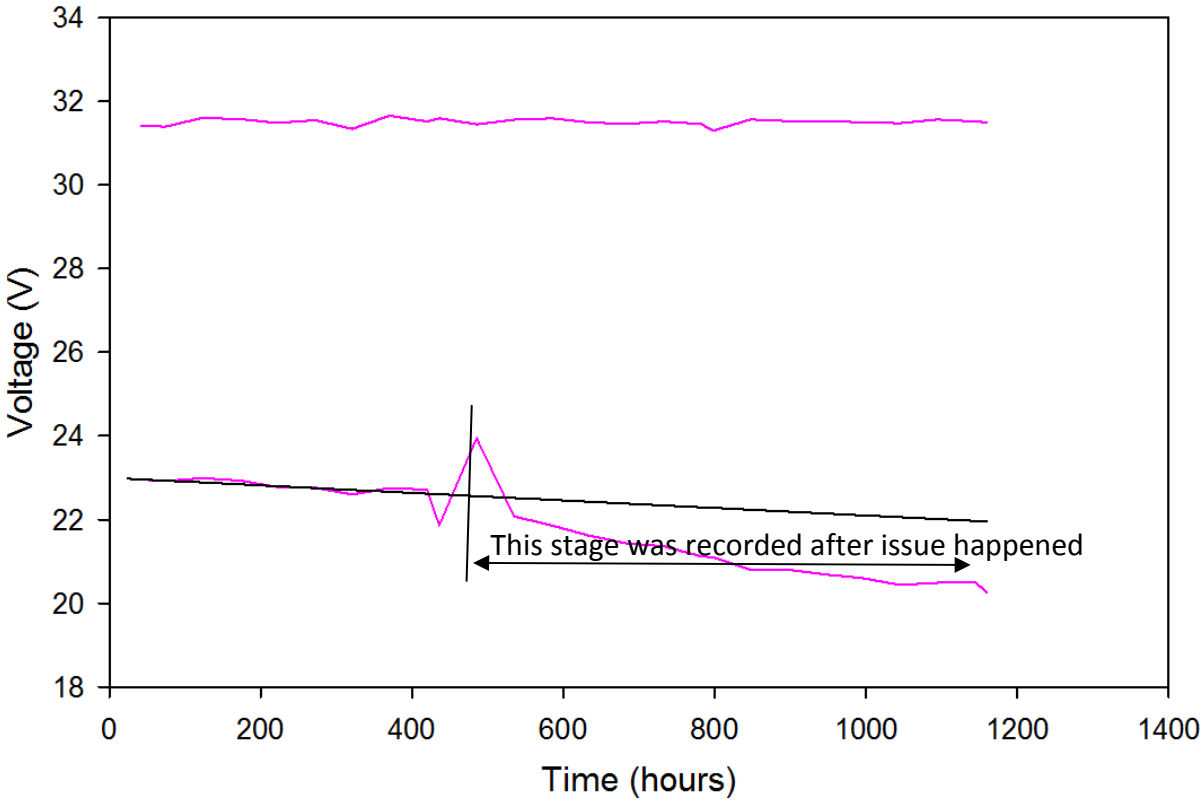

Figure 29: The voltage degradation fitting at maximum current of 1.8 A for the first 436 hours.

If nothing had happened to IP-SOFC-1, the voltage expected at 1200 hours operation would be ca. 22.04 V at the end. Instead, a value of 20.26 V was returned in the laboratory experiment, as a result of the problem.

The cell polarisation or over-potential is defined by the resulting drop in voltage from OCV ($E^o - V$) at the specific current density. Ohm's law states that the magnitude of

the voltage drop is proportional to the current, as shown in Equation 5-3:

$$V = IR \tag{5-3}$$

In order to do this, the equation should be expressed in terms of current density, meaning that the resistance must be multiplied by the unit area. This quantity is called the area-specific resistance (ASR). The Ohmic polarisation can be represented by Equation 5-4:

$$\eta_{ohm} = ir \tag{5-4}$$

Each *r* value is an area-specific resistance (ASR), including the ionic resistance of the electrolyte, the electric resistance of cell interconnects, and contact resistance between connecting parts and any other cell components. A definition of the ASR can be provided by the Equation 5-5 [185]:

$$ASR(r) = \frac{E^o - V}{i} \tag{5-5}$$

It can be assumed that the ASR is representative for the all resistances IP-SOFC. The ASR was evaluated using the equation described in Equation 5-6:

$$ASR = \frac{OCV_{\exp} - V_c}{i} \tag{5-6}$$

where OCV_{exp} is the experimental OCV, V_c is the measured voltage and *i* is the corresponding current density.

Estimated values of total Ohmic factors were obtained in the form of ASR, which can be unique in the IP-SOFC, regardless of the current density for durability test of IP-SOFC-1. These estimated values of ASR are summarised in Figure 30.

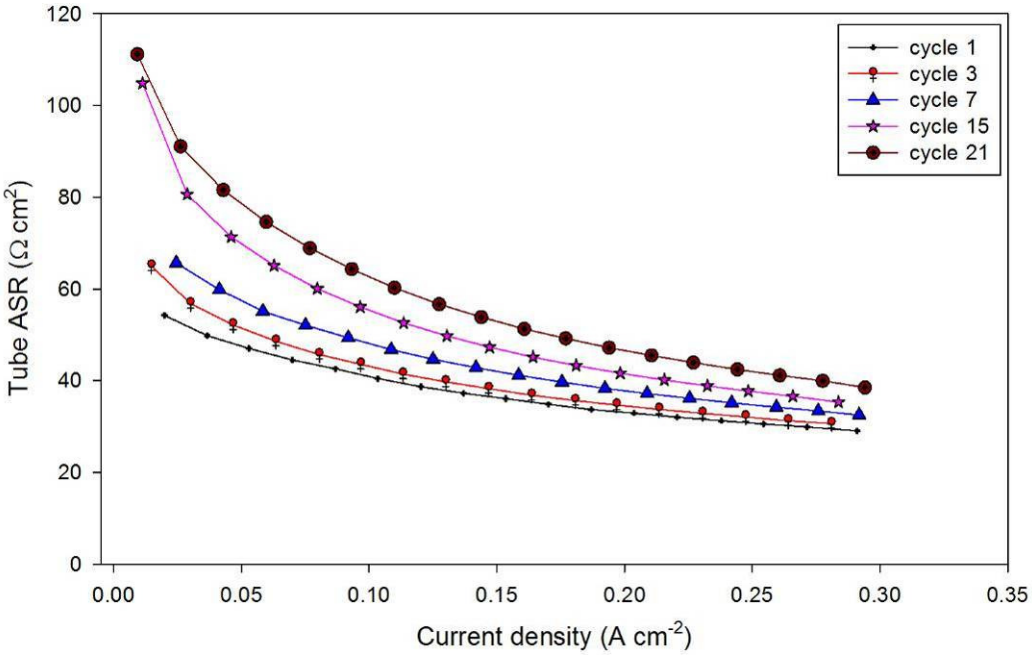

Figure 30: Measured area specific resistances for IP-SOFC-1.

Figure 30 shows that the ASRs of IP-SOFC-1 decreased rapidly at a low current density, whereas at higher current densities this became relatively slow, with a flat-linear shaped curve. Furthermore, the ASR of cycle 1 has a lower value than the other experimental cycles and all subsequent cycling values rose with increasing numbers of cycles.

As can also be seen in Figure 30, cycle numbers 15 and 21 show that the estimated values of ASR are very high compared with other ASR values which was recorded before the issue happen. This is due to the previously mentioned accident, where the ASR almost doubled from around 60 to 110 Ω cm^2. However, the ASR at high current density (300 mA per cm^2) just increased from 38 to 47 Ω cm^2 at cycle 1 and cycle 21, respectively, where the difference between them was only 9 Ω cm^2.

5.1.2 IP-SOFC-2

The durability study of IP-SOFC-2 was operated over 1140 hours, including 25 current load cycles and 3 shutdowns. These results were obtained by running on pure hydrogen fuel and air at 900 ^{o}C, where the flow rates were 1.5 litres per minute and 5.0 litres per minute for H_2 and air, respectively.

It can be seen in Figure 31 and Figure 32 that the OCV of IP-SOFC-2 started at a lower point than IP-SOFC-1 (31.21 V). This IP-SOFC consists of 30 cells and the equivalent voltage for IP-SOFC-2 was 1.04 V for each single cell. The figures show a slight improvement of OCV with operating time, increasing to 31.6 V where the equivalent voltage was 1.05 V for each cell. In general, the differences in OCV can be ignored here because the difference in OCV is around 0.01 V for each cell. As a result, it can be seen that the OCV remained stable. This phase amounted to a total period of 1140 hours, including three restarts and shutdowns of the test station, and 25 IV curves where each IV curve involves current load cycles. The voltage at 1.8 A (maximum current) started with a slight decrease at the beginning, with the recorded voltage close to around 21.69 V. The voltage under maximum current can be clearly seen to have increased by around 1.5% over the first 120 hours of operation of the output of IP-SOFC-2. This improvement in performance of IP-SOFC-2 remained stable until the IP-SOFC is restarted after 360 hours.

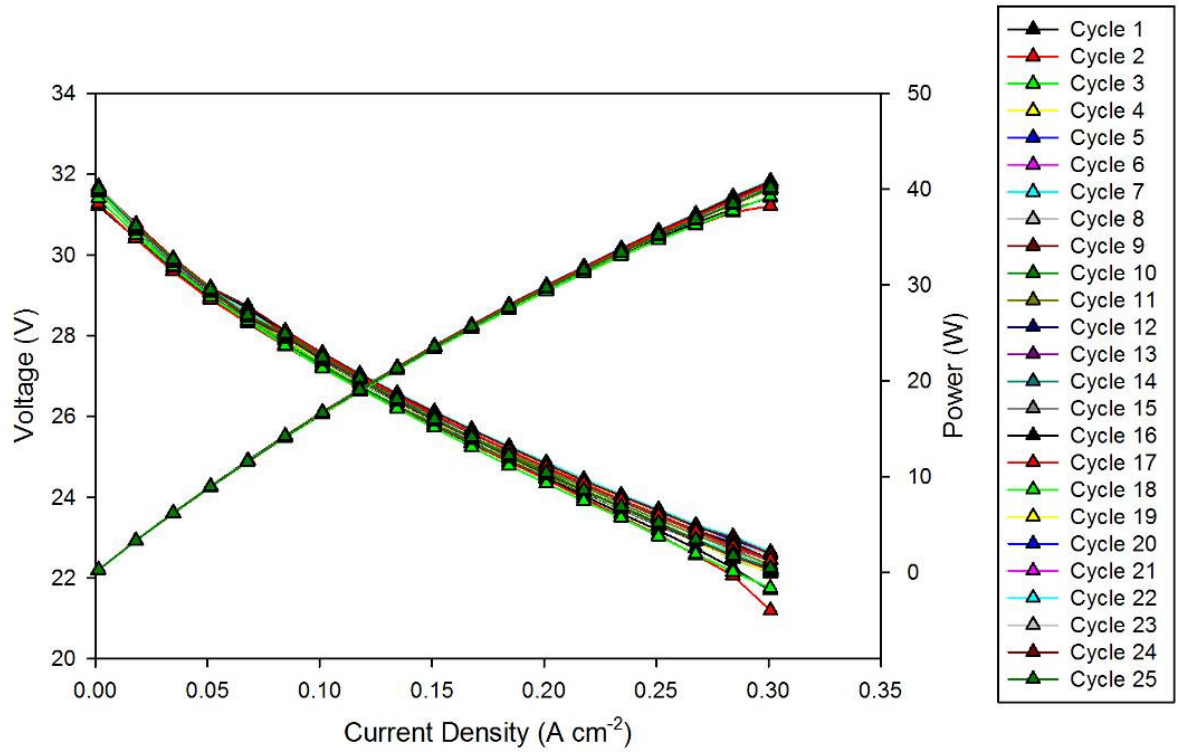

Figure 31: I-V and power curves for IP-SOFC-2.

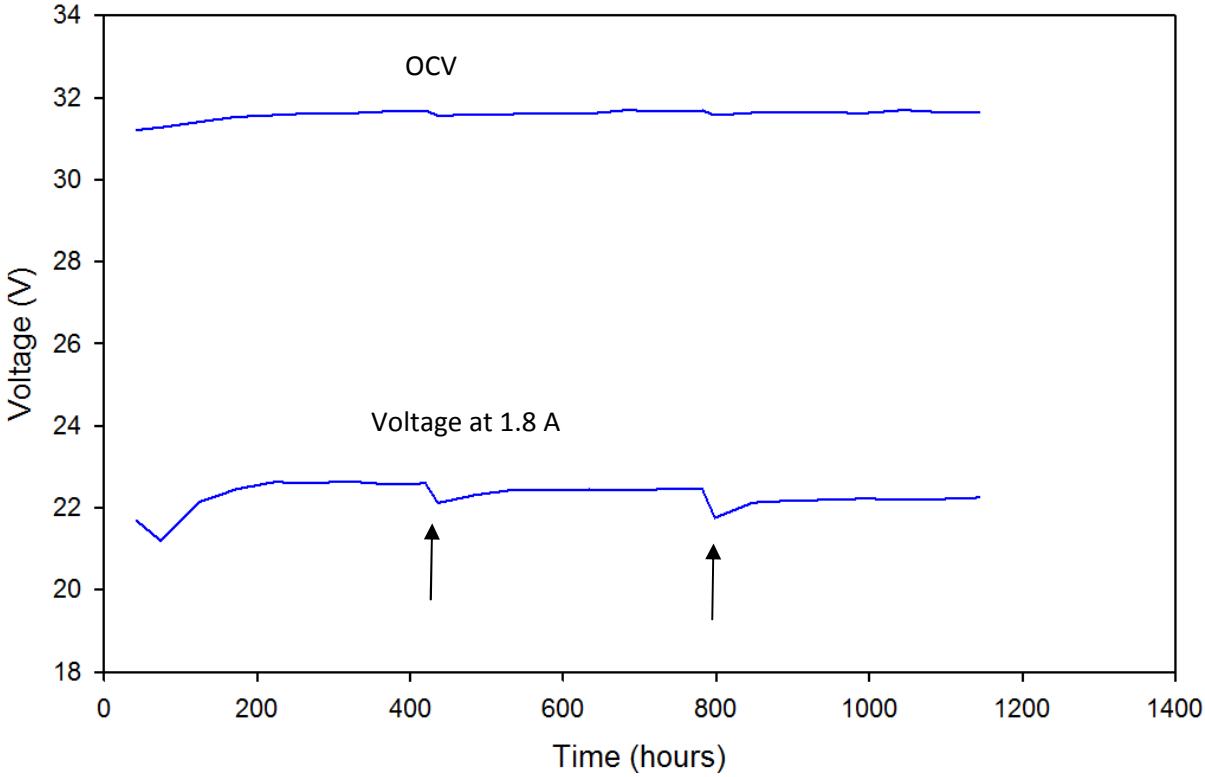

Figure 32: OCV and voltage at maximum current vs. time for IP-SOFC-2 (arrows show restarts of IP-SOFC)

After restating IP-SOFC-2, a clear decline in performance was noted. However, as the test proceeded, the performance of the IP-SOFC increased within the initial 100 hours. The same trend can be observed in the third restart: an initial drop in performance from the end of the last test followed by a continued improvement in performance throughout the test. This time, the performance levelled out after around 100 hours, as shown in Figure 32. It should be noted that this occurs as a result of the Ni oxidation to NiO because some air reaches IP-SOFC through the anode exhaust gas, then the NiO reduction results in a gain of Ni with the initial 100 hours, to show the sharpest rise in performance of IP-SOFC.

Table 6: Electrochemical performance of IP-SOFC-2 for cycling 1-25.

Time (hours)	Cell voltage at 0 A (Volt)	Cell voltage at 1.8 A (Volt)	Degradation Rate (% per 1000 hours)
42.08	31.21	21.70	~
172.72	31.53	22.45	~
222.130	31.57	22.62	0
271.54	31.62	22.60	2.19
370.35	31.66	22.57	1.60
436.00	31.56	22.11	10.55
485.41	31.59	22.31	5.23
534.81	31.60	22.44	2.67
584.21	31.61	22.43	2.40
633.62	31.61	22.45	1.91
683.03	31.70	22.43	1.84
732.44	31.66	22.45	1.51
781.84	31.69	22.45	1.39
798.09	31.57	21.75	6.70
847.50	31.63	22.12	3.55
896.90	31.66	22.18	2.95
946.31	31.63	22.19	2.63
995.71	31.62	22.23	2.28
1045.12	31.70	22.19	2.34
1094.5	31.64	22.21	2.10
1143.93	31.63	22.18	2.11

Figure 32 and Table 6 show the durability study for IP-SOFC-2 over 1140 hours, for OCV and voltage under applied current of 1.8 A. The voltage degradation rate can be calculated from Equation 5.1. As discussed above, the IP-SOFC voltage starts low and then improves over time. Therefore, it can be considered that in the first 172 hours of operation of the recovery phase, after cycling, voltage performance increases. As a result, the voltage degradation rate of IP-SOFC-2 was calculated from the highest voltage at the time of 222 hours, as shown in Table 6.

In general, the voltage degradation rate was 2.11 % per 1000 hours, during an operation that included 25 current load cycling and 3 restarts and shutdowns within 1143.91 hours. As can be seen from Table 6 and Figure 32, the voltage degradation rate gradually decayed over time. However, the voltage degradation rate increased at the restart of the experiment and then gradually decayed over time, at voltages at 436.0 and 798.1 hours of operation. This period considers the restarts and shutdowns.

Figure 33 shows the ASRs obtained from the IV curve in Figure 31. This includes 25 IV curves, where each IV curve was based upon current load cycles. The IP-SOFC-2 ASRs decreased rapidly at a low current density but the decrease was relatively slow, with the curve flattening at higher current density. Furthermore, the ASRs of IP-SOFC-2 rose with an increasing numbers of cycles, causing an increase in the electrolyte resistance and polarisation resistance.

These results are an indication that the level of current load cycling affects the

electrical performance of IP-SOFC. In general, the results for the measurement ASRs in IP-SOFC-2 were very close to the result of ASRs in IP-SOFC-1 before the problem occurred.

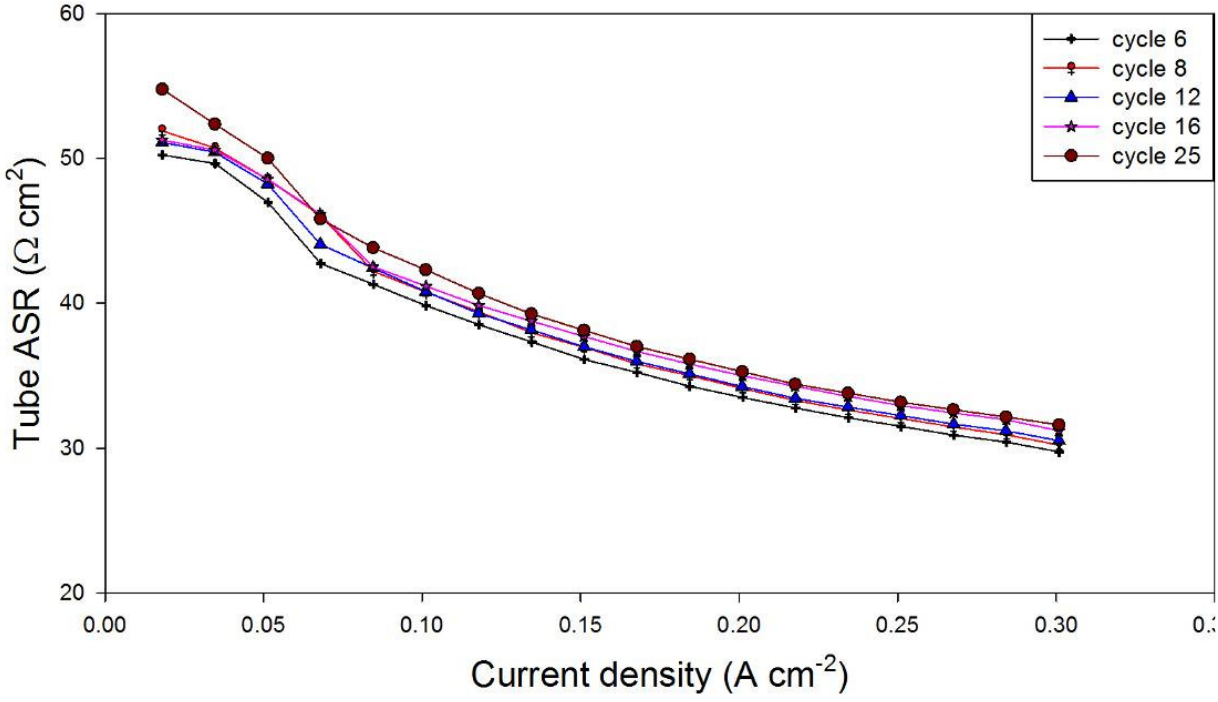

Figure 33: Measured area specific resistance for IP-SOFC-2.

5.1.3 IP-SOFC-3

The durability test of IP-SOFC-3 was conducted under a constant current at 1 A (0.17 A per cm^2) for more than 6000 hours of operation. Results were obtained by running on hydrogen at a rate of 1.5 litres per minute and air of 5.0 litres per minute at 900 ^oC. This took more than 6000 hours, including 133 current load cycles and 19 restarts and shutdowns. A sequence of long-term tests was applied on IP-SOFC-3, as shown in Figure 26.

Figure 34 shows the long-term durability test of IP-SOFC-3. The OCV remained almost steady at around 31.60 V, whereas a slight decline in the voltage can be seen under the design point load defined as 1.8 A (maximum applied current).

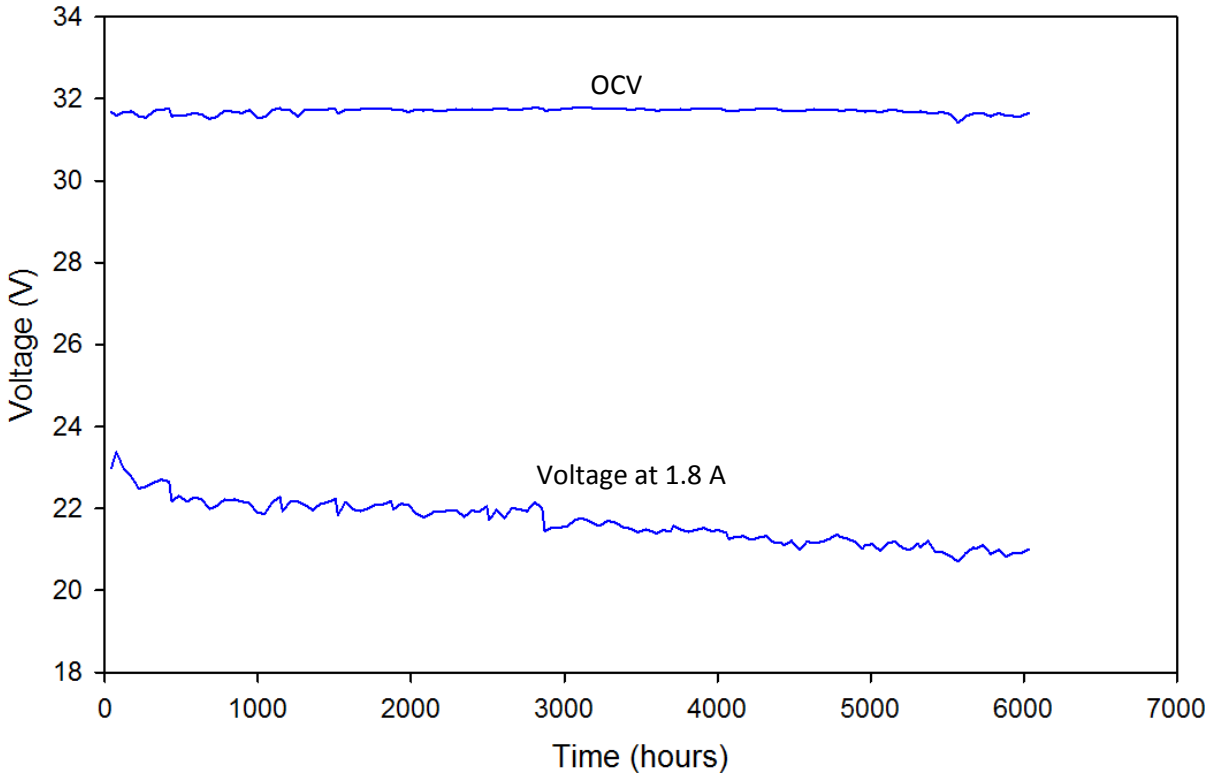

Figure 34: The OCV and voltage at maximum current vs. time for IP-SOFC-3

Table 7: Electrochemical performance of the IP-SOFC-3 at cycles 1-131.

Cycle	Time (hours)	Cell voltage at 0 A (Volt)	Cell voltage at 1.8 A (Volt)	Degradation rate (% per 1000 hours)
Initial test	42.0	31.67	22.98	0
Cycle 1	123.3	31.67	22.98	0 (no DR)
Cycle 8	485.4	31.58	22.30	6.01
Cycle 16	847.5	31.68	22.22	3.85
Cycle 24	1209.6	31.72	22.17	2.88
Cycle 32	1571.6	31.73	22.16	2.24
Cycle 40	1933.7	31.73	22.11	1.94
Cycle 46	2197.0	31.71	21.92	2.08
Cycle 53	2559.1	31.77	21.97	1.70
Cycle 61	2921.2	31.73	21.53	2.15
Cycle 69	3283.3	31.76	21.7	1.68
Cycle 77	3645.5	31.70	21.47	1.79
Cycle 81	3760.5	31.74	21.47	1.74
Cycle 89	4122.5	31.70	21.3	1.76
Cycle 97	4484.6	31.70	21.20	1.72
Cycle 105	4846.7	31.72	21.26	1.54
Cycle 109	5011.1	31.71	21.13	1.60
Cycle 117	5373.2	31.66	21.20	1.43
Cycle 125	5735.3	31.64	21.10	1.42
Cycle 131	6031	31.65	20.99	1.43

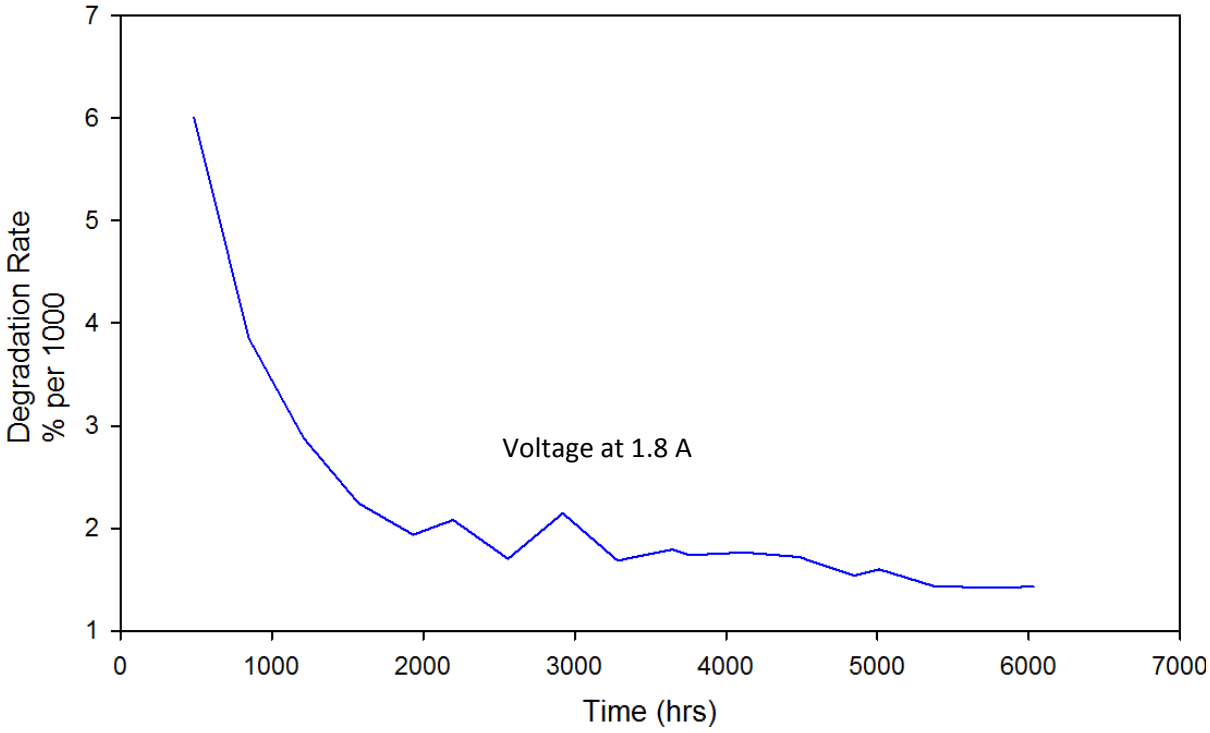

Figure 35: Degradation rate (% per 1000 hours) vs. time for IP-SOFC-3.

The Figure 35 and Table 7 provide a summary of the results of the cell voltage degradation rate (DR% per 1000 hours of operation) of IP-SOFC-3. It can be seen that there no cell voltage degradation was measured during the first of 123.3 hours of operation, which included cycle 1. After that, the maximum cell voltage degradation rate, 6% per 1000 hours, was obtained at 485.4 hours.

The cell voltage degradation rate then drastically decreased from 6 to 2.14% per 1000 hours between 485.4 and 2921.2 hours, which included cycle 8 to cycle 61. Between 3283.3 and 6031 hours (including cycle 69 to cycle 131), the cell voltage degradation rate remained small and highly stable, between 1.7% and 1.4% per 1000 hours.

Examination of the IV curves of IP-SOFC-3 shows how the IP-SOFC performs transiently. By plotting subsequent IV curves, transient performance as a function of

time can be assessed. Figure 36 shows the performance of IP-SOFC-3 in different cycles.

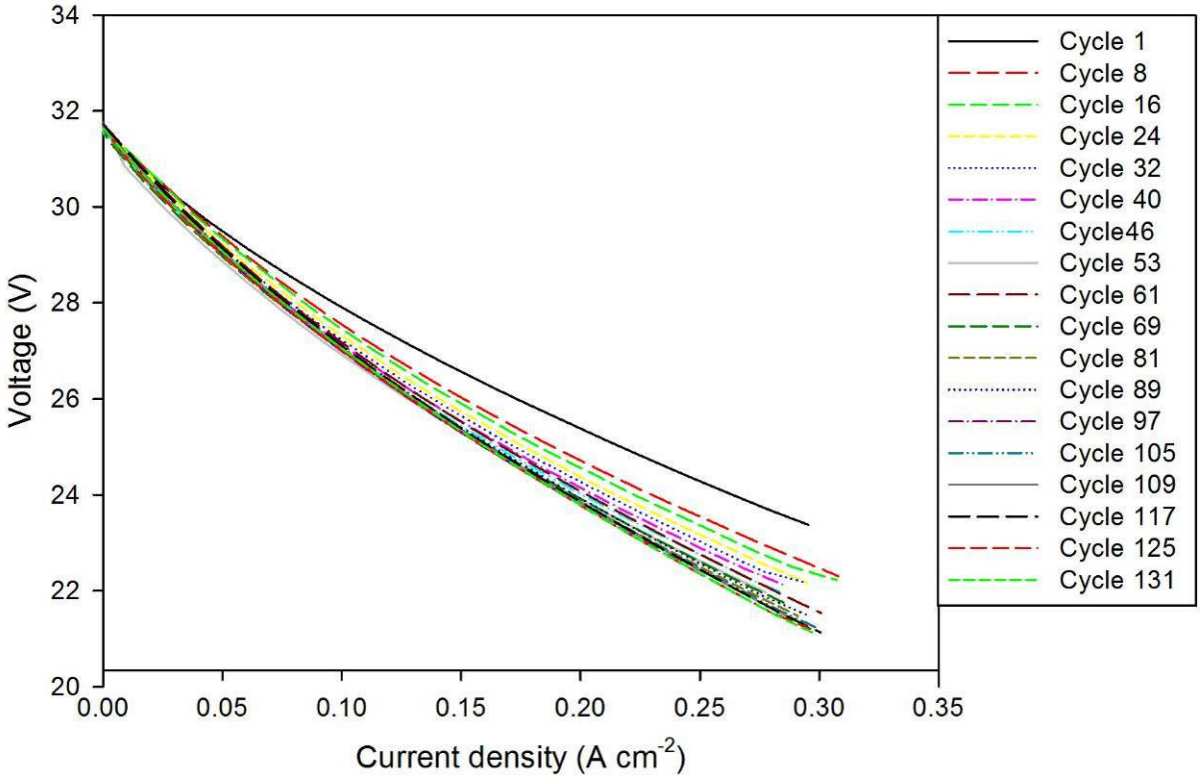

Figure 36: IV curves of IP-SOFC-3 in different cycles.

The IV curves were chosen to reflect the cycling values for each test sequence, and to show the discontinuation that occurred because of the degradation. Figure 36 shows a classical degradation, in that the initial IV curve taken shows the highest power density, expressed as the highest voltage at the highest current density. It is clear that a sharp decrease in performance of IP-SOFC-3 occurs from cycle 1 to 8 at the highest current density. Between cycle 8 and 61, the degradation rate is considerably lower than in previous cycles of IP-SOFC-3 performance. In contrast, the performance of IP-SOFC-3 evidently declines at a steady rate between cycle 61 and cycle 131.

As mentioned above in the section on durability studies, the process was stopped after 7 current load cycles and the SOFC Test Station was shut down and cooled to room temperature, after which it was restarted in accordance with the same conditions used in previous runs. Significant changes were observed in voltage at the maximum current (1.8 A), as shown in Figure 37. This highlights the difference in voltage of the IP-SOFC at the maximum current of 1.8 A. Here, the trend is clear, with IP-SOFC-3 losing voltage immediately after each restart, then the measured voltage only increased by a small amount throughout each session, although the effect of being restarted stayed with the IP-SOFC-3 and each test session saw a peak voltage lower than the previous session. For example, at the end of run 1 the voltage measured was 22.65 V and after restart run 2, the voltage was found to be 22.17 V, followed with a small increase over its previously measured voltage; this was 22.30 V (see Figure 37).

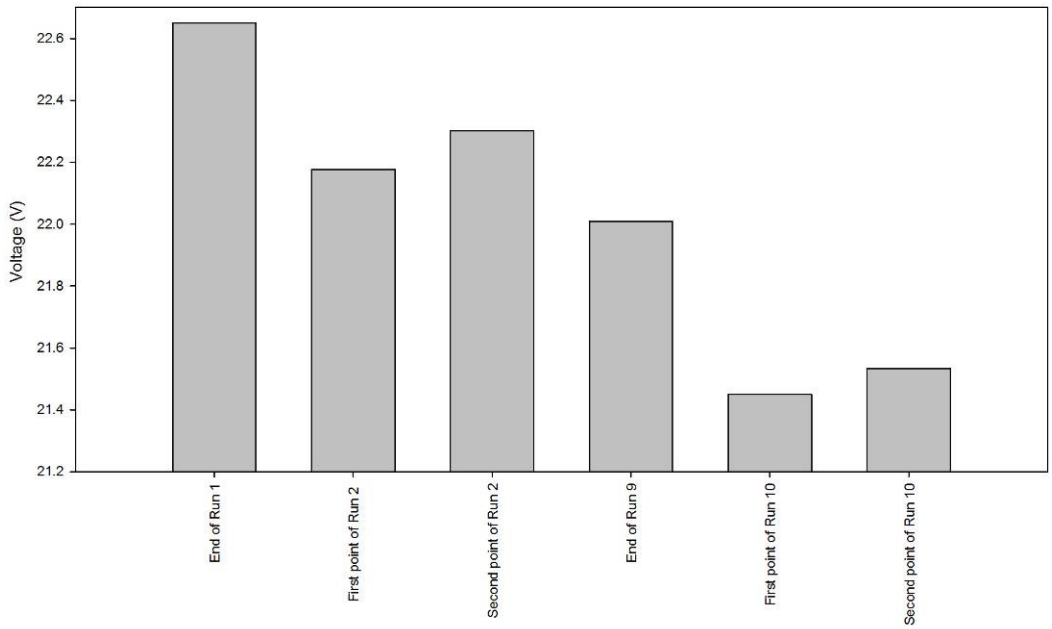

Figure 37: The voltage drop at high current for IP-SOFC-3 after restart.

As shown in Figure 34 the whole period of the durability test of IP-SOFC-3 was more than 6000 hours and the data was recorded every 4 seconds, resulting in a very large data set. This data is difficult to read and have therefore been smoothed using an averaging method for each cycle. Figure 38 shows the average voltage for each cycle at a constant current of 1 A, with each cycle being recorded over a period of 2 days. It can be noted that the average voltage output of IP-SOFC-3 remains highly stable. The temperature also showed a slight increase of about 5 ^{o}C at around 900 ^{o}C, which results from the exothermic reactions of the fuel cell due to the applied current load of the IP-SOFC. This will be explained in more detail in the next section.

The voltage output of IP-SOFC-3 at a constant current of 1 A remained stable at around 25.5 V. However, increasing the load current cycling and restarting the IP-SOFC had an effect on the performance of IP-SOFC-3. As a result the voltage output decreased by around 0.5 V after 13 restarts and shutdowns, which included 90 load current cycles.

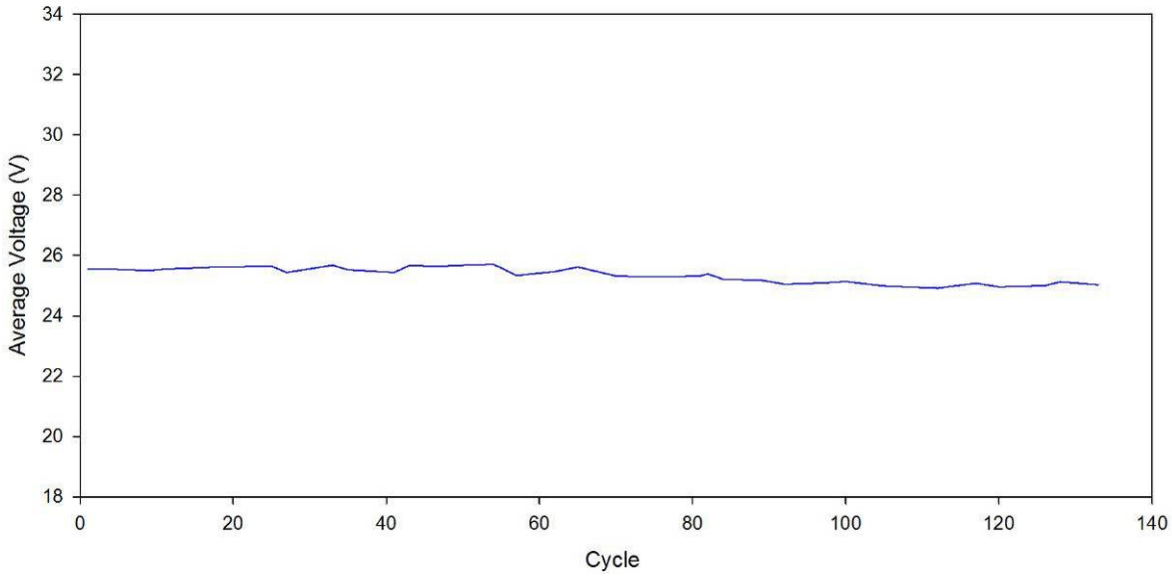

Figure 38: The average voltage for each cycle at 1 A

The resistance can be found by solving for the slope of the polarisation curve. In a SOFC operating on hydrogen, the overall polarisation curve is quite linear and dominated by Ohmic effects. It is therefore very important to select the appropriate region. The activation region can be avoided by starting the calculation of the slope from 0.1 A. Figure 39 shows the Ohmic resistance for each current load cycling, which was calculated from the slope of the polarisation curve in Figure 39. The Ohmic resistance started at 4.43 Ω and increased to 5.5 Ω; after initially rising rapidly, the increasing rate of the Ohmic resistance then slowed down considerably.

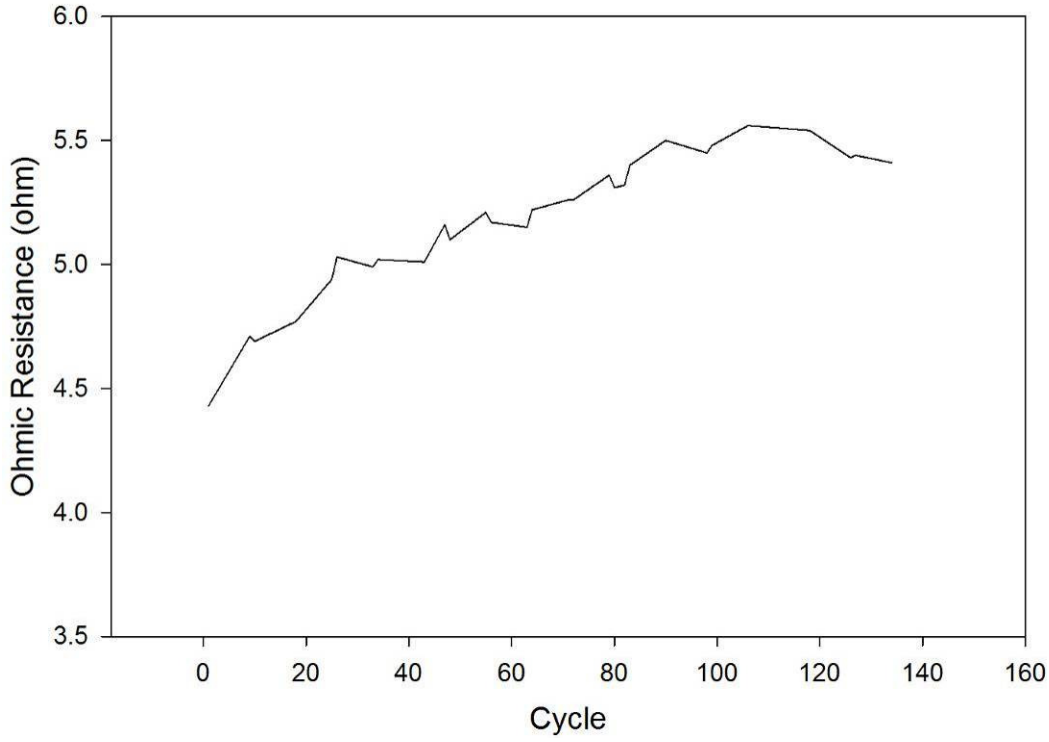

Figure 39: The Ohmic resistance of IP-SOFC-3 in each current load cycle.

This method should yield the maximum possible value for the Ohmic resistance, because the slope calculated in the middle region of the polarisation curve is solely as a result of ionic losses. In fact, activation and concentration polarisation losses also contribute to the voltage loss in the middle region, although for these high-

temperature fuel cells the approximation is very close. The increasing resistance of the IP-SOFC may be due to a number of reasons mentioned earlier, one of which relates to the structures of the components.

5.2 Comparison between the three IP-SOFCs

All three IP-SOFCs were operated in the same sequence, as discussed above, with the main difference being the anode reduction process. Figure 40 shows the OCV and voltage at 1.8 A vs. time for the three IP-SOFCs, with IP-SOFC-1 and IP-SOFC-2 being operated for ca. 1100 hours, and the IP-SOFC -3 was operated for ca. 6000 hours, including current load cycling at every 48 hours and start-up and shut-down every 366 hours.

At 436 hours, the voltage at maximum current of 1.8 A of the three IP-SOFCs were almost equal, as was their OCV. Because of the problem mentioned earlier, the performance of IP-SOFC-1 was affected after the first 436 hours, and exhibited a somewhat different behaviour and performance than the two other IP-SOFCs. The results of IP-SOFC-2 and IP-SOFC-3 were very consistent with each other, in terms of both the OCV and the voltage at 1.8 A.

In general, all results were very close despite small variations. In addition to any other conclusions, this proves the excellent quality of the RRFCS IPSOFCs. The comparison also demonstrates that the slight differences in the anode reduction process did not show any big influence on the performance of the IP-SOFCs for long term test.

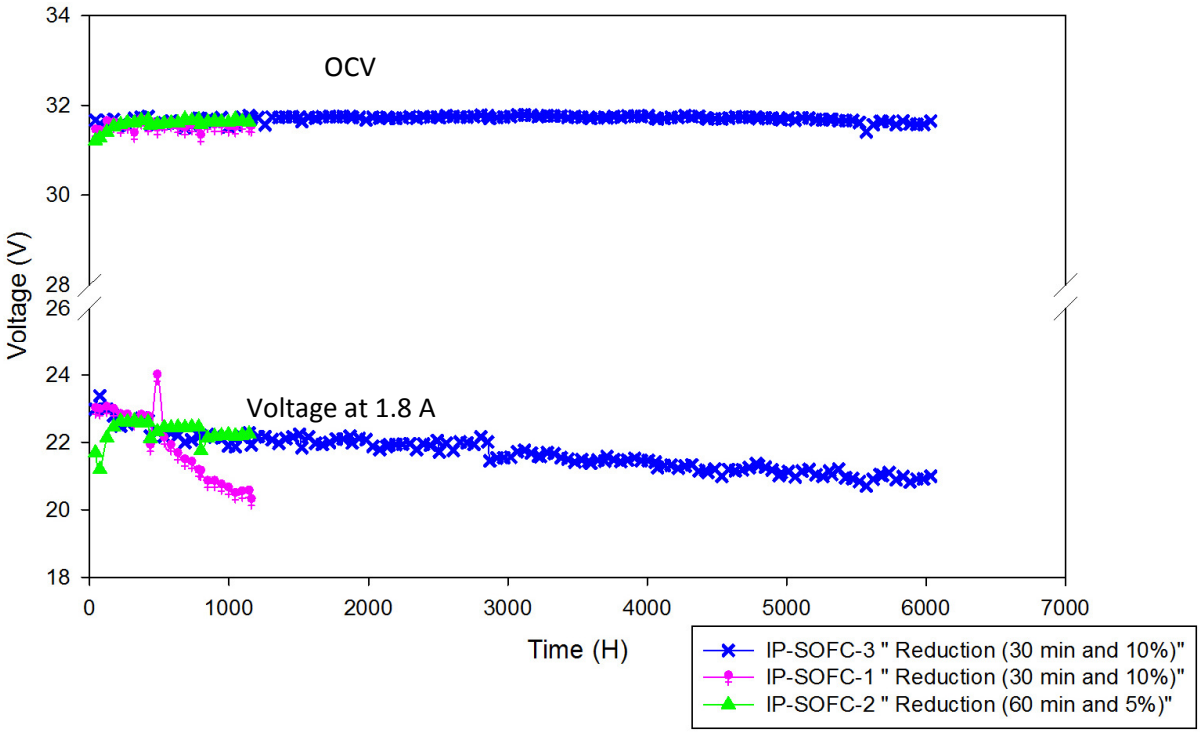

Figure 40: The comparison between the OCV and the voltage at current 1.8 A vs. time for the three IP-SOFCs.

Figure 41 and Figure 42 show the outside surface of the IP-SOFC before running and after 1000 hours of operation, respectively. Comparison of the two SEM images suggested that the outside surfaces of components changed and some dissociation of materials occurred. This is as expected, because each IP-SOFC experienced a long-term test, as well as many current load cycling and restart.

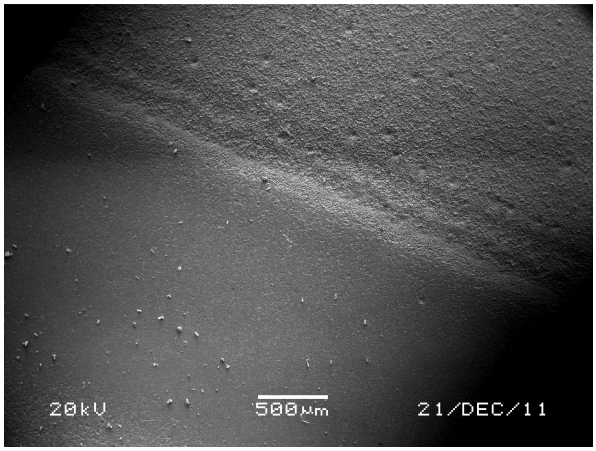

Figure 41: The outside surface of the IP-SOFC before running

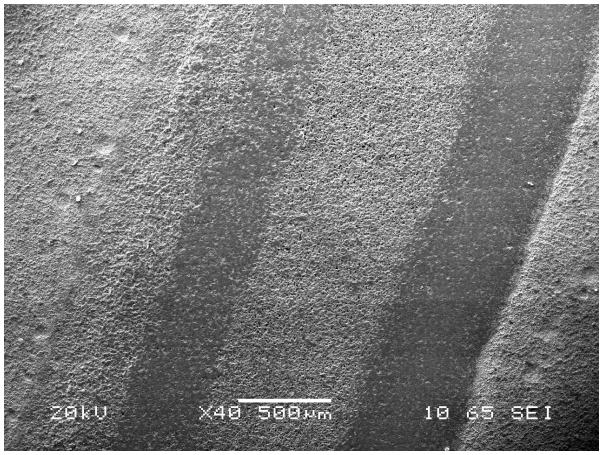

Figure 42: The outside surface of the IP-SOFC after 1000 hours running.

The photos in Figure 41 were taken for the fresh IP-SOFC and the one after 1000 hours of operation. The two IP-SOFC pictures, in particular the area highlighted by the red circle, show that there is a clear damage to the material, where some components have been destroyed (see Figure 42). This indicates that the IP-SOFC in Figure 42 has some of its material destroyed, which is almost certainly due to long-term testing (more than 1000 hours) and exposure to numerous current load cycling tests. This load concentrates the oxygen reaction (Equation 1.2) into the intact area, causing an increase in polarization and Ohmic resistance. As discussed, the voltage degradation rate was 2.11% and 1.43% per 1000 hours of operation for IP-SOFC-2 and IP-SOFC-3, respectively. This shows that there was a change in the microstructure of the IP-SOFC tube.

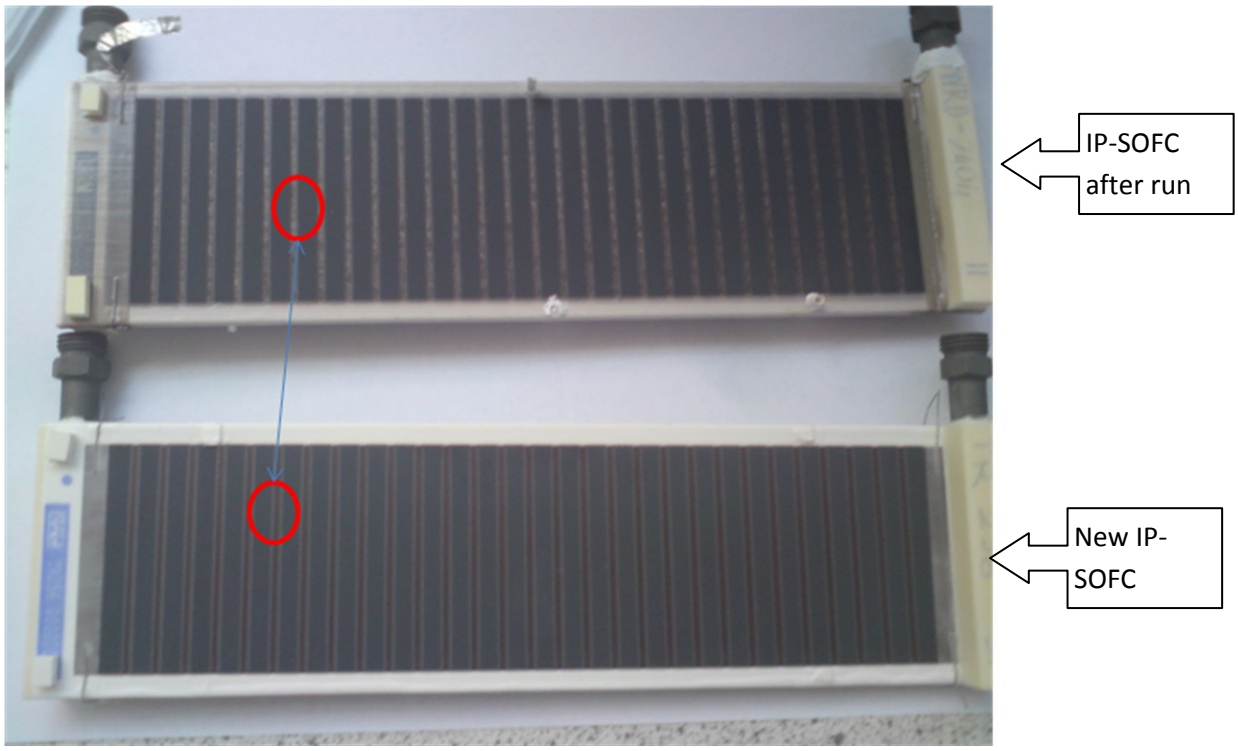

Figure 43: The photos of the fresh IP-SOFC and the one after 1000 hour run.

In all IP-SOFCs, this type of test has been shown to result in serious damage, with the restarting and shutdown of IP-SOFC resulting in the entry of a quantity of oxygen to the anode surface, partially like a redox cycling. This exposure results in oxidization of Ni to NiO, causing a decrease in the performance of IP-SOFC at restart, when large value of Ni changes to NiO. This change resulting from the oxidation of Ni, resulting in the catastrophic failure or gradual performance degradation of the cermet anode [186]. Another degradation process associated with the Ni-YSZ anode is the loss of Ni as a result of humid atmosphere leading to formation of volatile $Ni(OH)_2$ as shown in Equation 5-8.

$$Ni + 2OH \rightarrow Ni(OH)_2 \qquad 5\text{-}7$$

5.3 Theoretical description of Current Load Cycling result

The performance degradation of fuel cells occurs over a period of time and is linked with interfacial reactions between various cell components and the deterioration of material properties. SOFC degradation due to electric load cycling can be quantified as described by the following paragraphs.

There is usually no current flow when a fuel cell is not connected to an external load, and the open circuit voltage or the maximum reversible cell voltage may be obtained by using the equilibrium Nernst potential, V_{Nernst} for the particular electrochemical reaction system [187]. The V_{Nernst} is obtained by using the chemical species partial pressure at the cell outlet or inlet. On the other hand, it is more suitable to obtain an average of the outlet and inlet values, V^{o}_{Nernst} and V^{i}_{Nernst}, where superscripts *o* and *i* represent the outlet and inlet locations.

$$V_{Nernst} = \frac{1}{2}(V^{o}_{Nernst} + V^{i}_{Nernst}) \qquad 5\text{-}8$$

$$V^{i}_{Nernst} = -\frac{\Delta G^{o}}{n_e F} - \frac{RT}{n_e F}\ln\left[\frac{P^{i}H_2O}{P^{i}H_2\sqrt{P^{i}O_2}}\right] \qquad 5\text{-}9$$

$$V^{o}_{Nernst} = -\frac{\Delta G^{o}}{n_e F} - \frac{RT}{n_e F}\ln\left[\frac{P^{o}H_2O}{P^{o}H_2\sqrt{P^{o}O_2}}\right] \qquad 5\text{-}10$$

Where $\Delta G^{o} = -RT\ln[K(T)]$ and is referred to as the change in Gibbs free energy at standard conditions. K is the equilibrium constant, T is cell temperature, and R is universal gas constant.

n_e = the number of electrons taking part in the electrochemical reaction

F = Faraday's constant

P = the partial pressure of respective species

When a fuel cell is connected to an external load, it begins to supply electric current and its operating voltage drops as result of the irreversibilities related to internal resistances. The difference between open circuit voltage (V_{open}) or the maximum reversible cell voltage and the operating voltage (V_{OCV}) is referred to as polarization degradation/loss (η_{ohm}) [188]. The cell performance relies on three things: the general cell reaction, type of reactants at the electrodes, and products of the reaction. Akkaya [189] gave a detailed description of polarization degradation/losses. Operating cell total polarization degradation composes of 3 dominant sections: ohmic resistance polarization (η_{ohm}), charge transfer or activation polarization (η_{act}), and diffusion or concentration polarization that include chemical reaction polarization (η_{conc}).

$$\eta = \eta_{ohm} + \eta_{act} + \eta_{conc} \qquad 5\text{-}11$$

Degradation is considered as a function of two operating parameters: the increase of area specific resistance (ASR) and decrease of cell voltage [190]. ASR is the most useful metric for understanding and quantification of degradation. It is purely a physical property relying mainly on the temperature of the cell, but also being somewhat dependent of current and voltage. The degradation rate is normally specified as a change of resistance or voltage with time as represented in the following Equations [190, 191]:

$$V_{cell}(t; j) = OCV\ (t) - i\ (t)\ R_{sec}(t) = OCV\ (t) - j\ (t)\ ASR_{sec}(t) \quad 5\text{-}12$$

Where OCV (t) and j (t) are constant.

The goal of this section is to improve voltage degradation of SOFC stack assessment methods, and to find a relation between voltage degradation at constant current over time with other parameter such as active area, number of cells and OCV of SOFC stack.

5.3.1 Experiment result of theoretical description

Ohmic losses is a linear function between the cell voltage and current density, but activation and concentration losses are logarithmic functions of current density [188], as shown in Figure 9 in Chapter 2. In the SOFC, resistance arises from the transportation of ions and electrons through the electrolyte, electrodes or interconnects in most of the fuel cell. The cell polarisation or over-potential is defined by the resulting drop in voltage from open circuit voltage ($E^o - V$) at the specific current density. The resistance can be found by solving for the slope of the polarisation curve. This is a resistance associated with all resistances that hinder the transmission of oxygen ions. In a SOFC operating on hydrogen, the overall polarisation curve is quite linear and dominated by Ohmic effects. It is therefore very important to select the appropriate region. The activation region can be avoided by starting the calculation of the slope from 0.1 A. Figure 44 shows that the ohmic resistance increase with time.

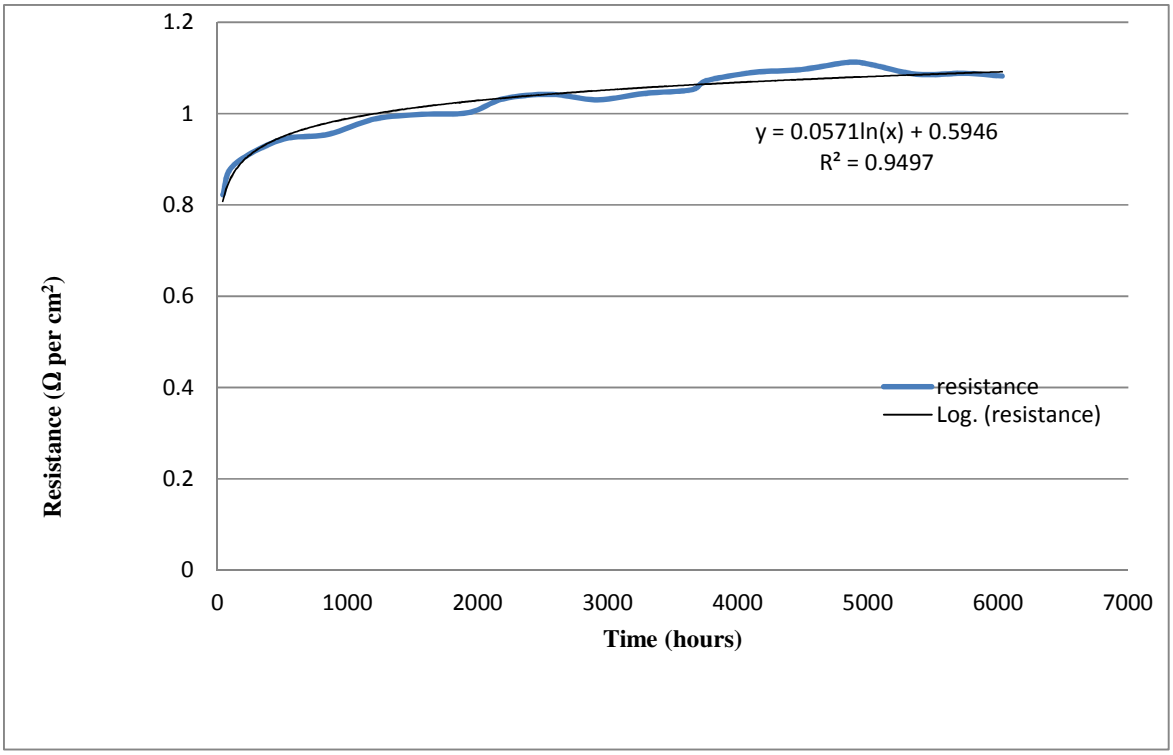

Figure 44: Ohmic resistance with time

The black line in Figure 44 shows the fit line for ohmic resistance with logarithm time, as shown in below Equation 5-13.

$$R_t = 0.0571\ln(t) + 0.5946 \qquad 5\text{-}13$$

Where R is ohmic resistance and *t* is time (hour), as mentioned before ohmic resistance was the slope of the polarisation curve.

$$R = \frac{A(V_1 - V_2)}{N(I_2 - I_1)} = 0.0571\ln(t) + 0.5946 \qquad 5\text{-}14$$

Here, *A* suggests the area of cell, the number of cell is given by *N*, *V* and *I* is voltage and current, respectively.

Assume the I_1 equal zero, as a result the V_1 will be equal open circuit voltage (OCV). The polarisation curve was measured at constant current, and then I_2 will be indicated to maximum current I_{max}. The above equation can be represented as the Equation 5-15:

$$R = \frac{A(OCV - V_2)}{N(I_{\max} - 0.0)} = 0.0571\ln(t) + 0.5946 \qquad 5\text{-}15$$

The ohmic resistance was increasing with time, the Equation 5-15 can be rewriting as following Equation 5-16

$$R_t = \frac{A(OCV - V_t)}{N * I_{\max}} = 0.0571\ln(t) + 0.5946 \qquad 5\text{-}16$$

The above equation 5-16 can give the new one which can be calculated the voltage, as a function of time, under maximum current at any time, as given by Equation 5-17.

$$V_t = OCV - \frac{N * I_{\max}}{A}(0.0571\ln(t) + 0.5946) \qquad 5\text{-}17$$

Figure 45 shows the voltage calculated from previous data using Equation 5-17, on 30 cells IP-SOFC-3 (6 cm^2 per cell active areas) operated at maximum current 1.8 A and the OCV was 31.6 V. It was plotted along with the experimental data in and showed good agreement for long term testing of IP-SOFC-3 as compared with previous data shown in Figure 34.

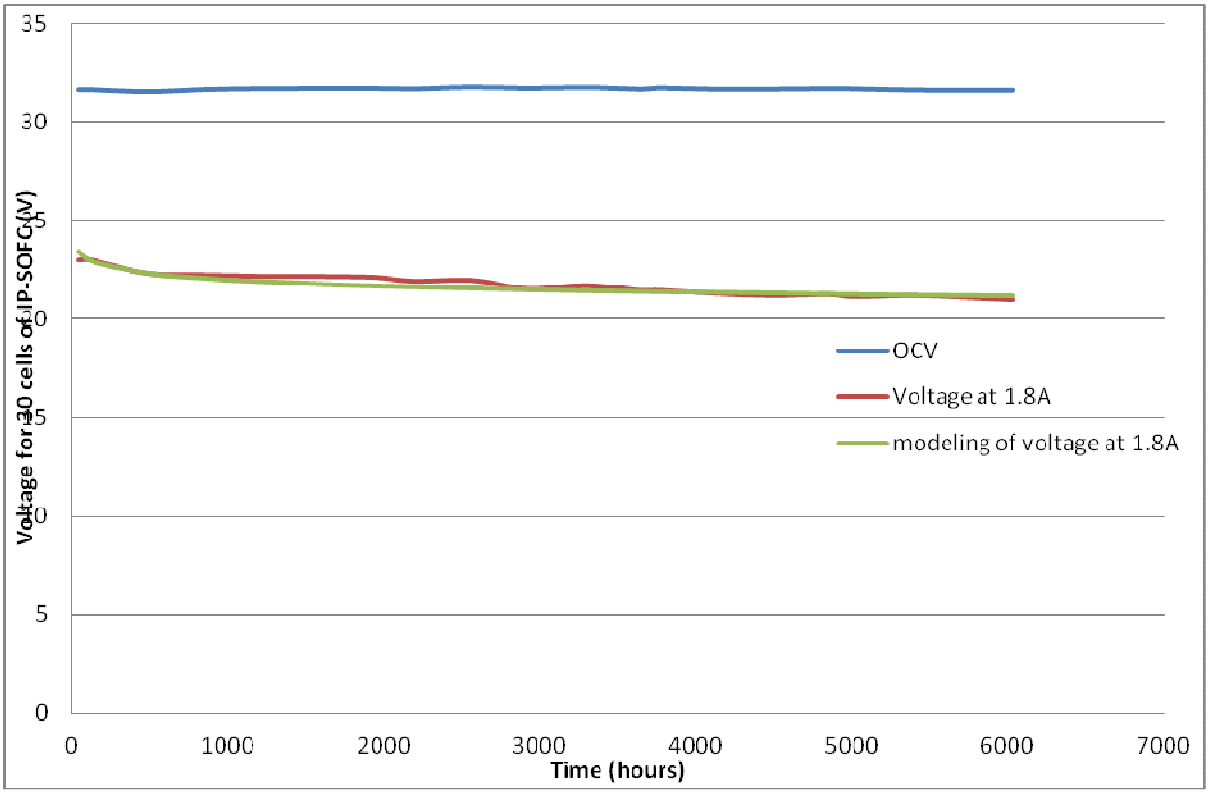

Figure 45 : The OCV and voltage of IP-SOFC-3 at maximum current vs. time for comparison with equation 5-17.

To check equation 5-16 in the evaluation of the performance and degradation rate of SOFC, available experimental data for long term testing is employed here. This kind of testing has been done by Greg et.al [192]. Figure 46 shows their long-term test results (ca 3500 hours) for 5-cell stacks tested in SOFC with the active area of 100 cm^2 per cell. A durability test was conducted at 750 ^oC with operating at constant current of 36.5 A. The voltage degradation rate was shown to be < 2% per 1000 hours of operation.

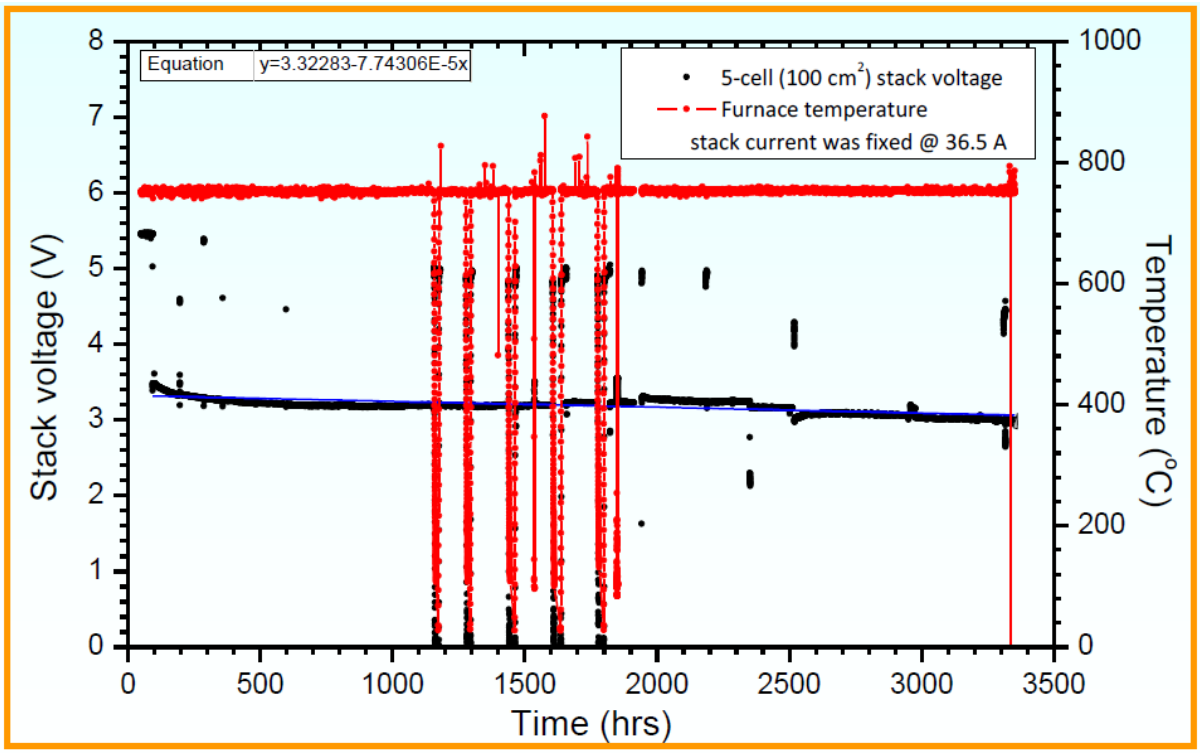

Figure 46: Cell voltage of 5 cell stacks of SOFC [192].

Figure 47 shows the voltage degradation rate calculated from Figure 46 data using Equation 5-17, on 5 cells stack (100 cm^2 per cell active areas) operated at fixed current mode 36.5 A and the OCV was 5.5 V.

As can be seen from Figure 47, the cell voltage gradually decreases over time. The voltage degradation calculated is slightly higher compared with original result to that shown in Figure 46. At 3500 hour of operation, the stack voltage was 3.1 V at original result, whereas the stack voltage was 3.5 V at the stack voltage calculated.

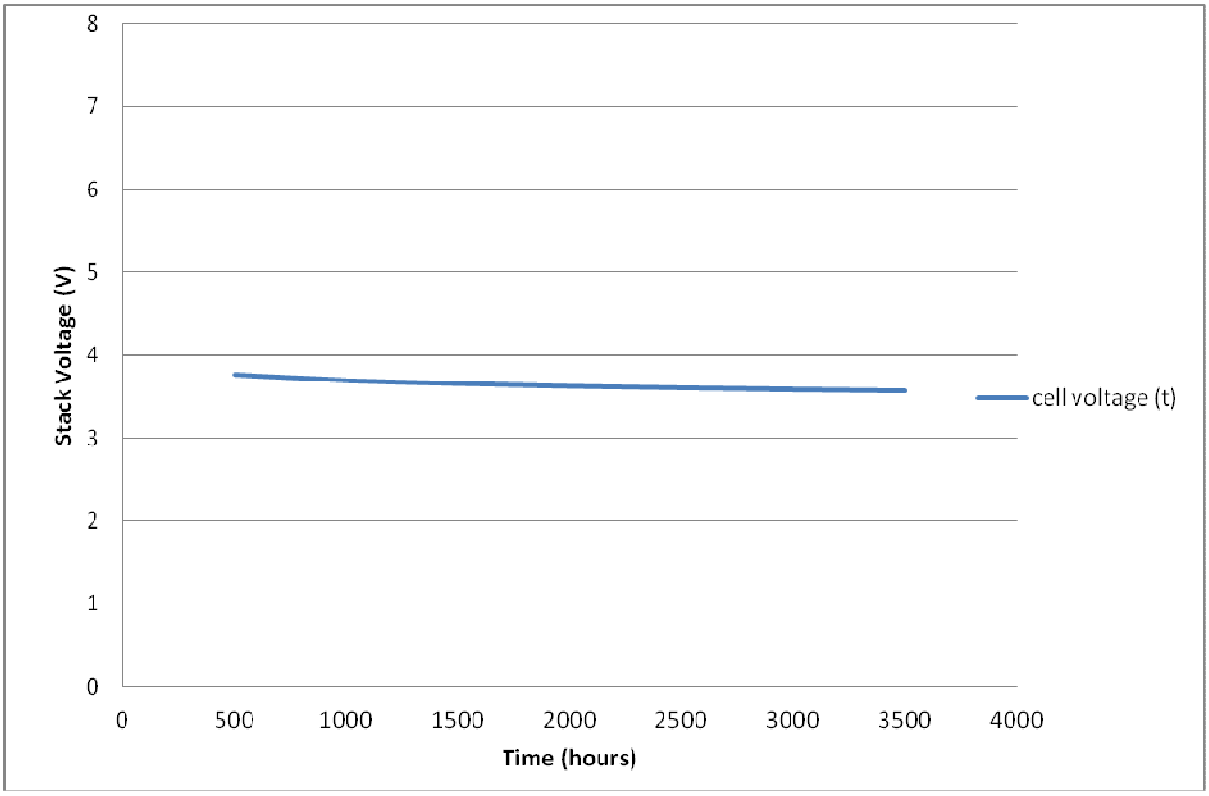

Figure 47: Voltage degradation rate calculated from Figure 46 data.

From Figure 45 and Figure 47, the Equation 5-17 was a good result compared with the original data. Finally, the Equation 5-17 form of voltage degradation can be helpful in meeting the specific needs of the future work. Regarding this work to find relation for voltage degradation over time, the assessment method proposed here requires more work.

5.4 Temperature cycling associated with current load cycles

This section considers the effects of temperature changes on IP-SOFCs due to exothermic reactions. The change in current can be associated with a change in the temperature of the IP-SOFC. Therefore, a reference test was carried out, where the temperature of the IP-SOFC was cycled. The cycling values were based on the following considerations: Differences in the temperature of the IP-SOFC were

measured between high and low current density and were found to be in the range of +10 ℃ maximum. The measured differences in the temperature of IP-SOFC over the cell during the test varied from one point to another, as shown in Figure 48. This is because the thermocouples inside the furnace take different positions. However, the real temperature differences could be larger than these measured values, because the thermocouples did not directly touch the IP-SOFC surface, instead being placed about 2.0 cm above the cathode surface. This situation comes from the exothermic reactions of the fuel cell, as a result of applied current load of the IP-SOFC. In Figure 48, the IP-SOFC voltage is shown for the test, with cycling temperature as a function of operating time and compared to a cell test at constant current and temperature. The IP-SOFC voltage trend was not affected by the cycling of the temperature under these conditions.

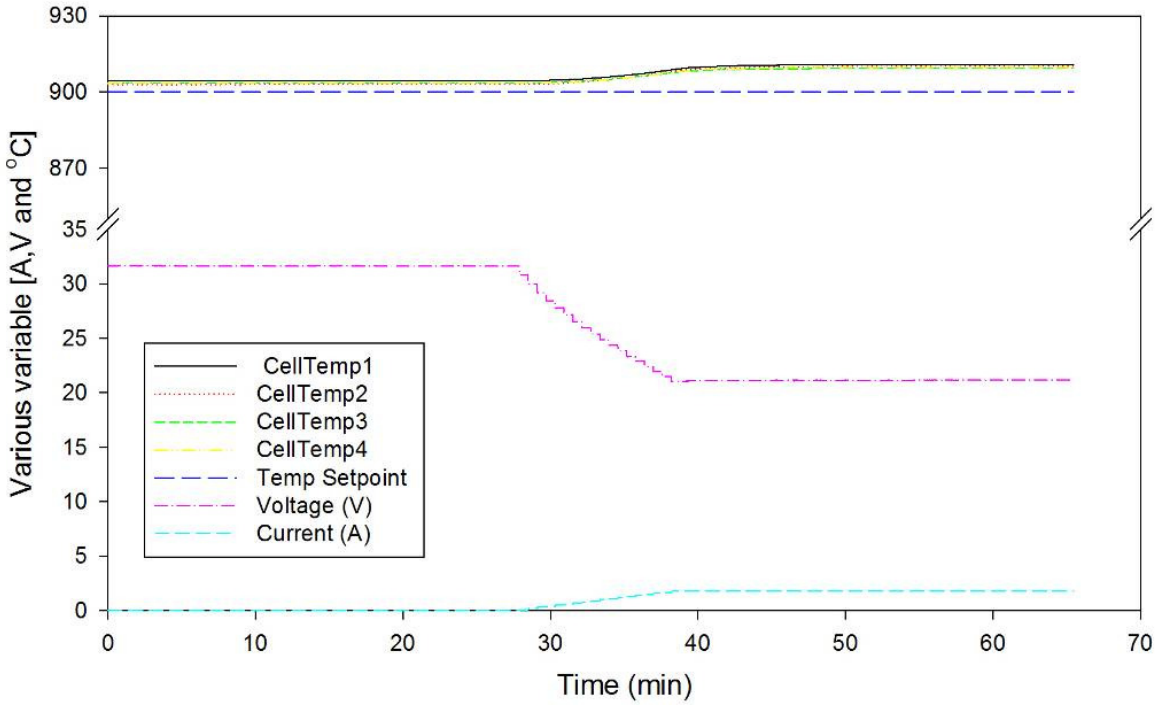

Figure 48: The effect of cycling the temperature on the voltage of the IP-SOFC.

The chief reason for micro-cracking or destruction of material in SOFCs is the abrupt changes in temperature causing failure. The temperature increases during the operating due to the leakage of fuel or increasing load current, creating stress between IP-SOFC materials, as expressed in Equation below.

$$\sigma = -E\,\alpha\,(T_2 - T_1) \qquad 5\text{-}18$$

σ thermal stress, α is the CTE and the magnitude of the thermal gradient is given by (T_2-T_1).

So, in this work, the current load cycle period was as long as 48 hours, which could effectively avoid large temperature gradients and hotspots causing micro-cracking and failure in SOFC.

5.5 Thermal cycling

Thermal cycling is also known as temperature cycling, in which the cycling proceeds through extreme temperatures. The main aim of this section is to find out the exact mechanism of IP-SOFC degradation when it is subjected to thermal cycling. According to the literature [165], there is a rise in temperate threshold throughout the start-up and shutting down. These changes keep proceeding throughout transient circumstances like thermal cycling leading to delamination and accumulation of stress at the crossing point.

This experiment is of vital significance as SOFCs are capable of undergoing different cycles of heat under real life contexts, e.g. they are used for the CHP devices and other systems that are helpful in generation of stationary electricity.

5.5.1 Theory of degradation due to thermal cycling

The experiments were based on the theory which suggested that ceramic objects in the cells have flaws. However, there imperfections can be exacerbated by limiting the pathways of current, which causes enhanced stress; these factors could result in a breakage due to brittleness of the material. Another study [154] proved that some of the materials present in these fuel cells meet up the coefficient of thermal expansion when there is a uniform rise in temperature. However, the situation is usually not 'uniform' as supposed as by this theory, for instance if the sample heats up quickly or if it is not allowed to expand then in such cases a huge amount of thermal stress is experienced. But, this theory was a pretty acceptable as there was no damage reported when the temperature condition is uniform.

Stress becomes tensile when cooled, leading to extreme contractions due to temperature fall, as shown in Equation 5-18.

5.5.2 Experiment on thermal cycling

IP-SOFC-1 was used in the thermal cycling test in order to clarify the effects of thermal fluctuations on IP-SOFC performance.

The IP-SOFC was ramped to its operating temperature of 900 ^{o}C in increments of 5 ^{o}C per minute and then kept running for one hour at OCV. An IV curve was then derived by cycling from zero current to a maximum current of 1.8 A, then back to 0 A. Following this, the IP-SOFC-1 was allowed to cool to room temperature through a process of natural cooling. This process was repeated five times, as illustrated in Figure 49.

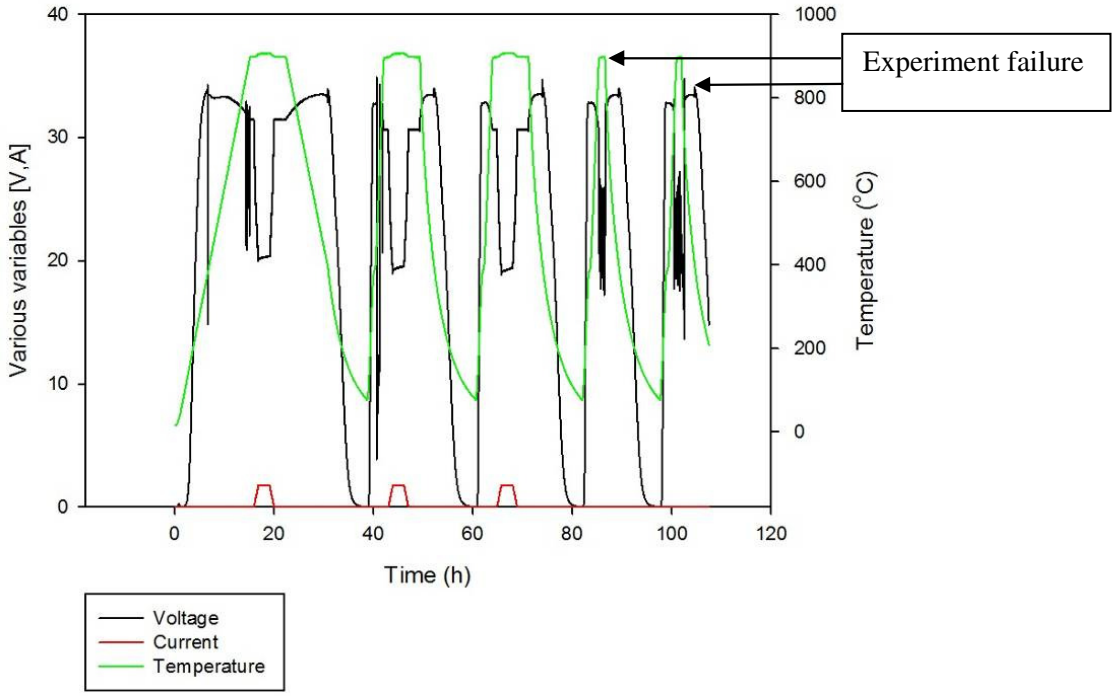

Figure 49: Test profile for thermal cycling tests of IP-SOFC-1(the temperature rate was 1 ^{o}C per minute in first run whereas it was 5 ^{o}C per minute in others runs).

As shown in Figure 50, it is clear that the first OCV was at 31.62 V, although this value dropped in the second and third runs. In the fourth and fifth runs, the test station did not draw the IV curve due to experiment failure, because it was programmed that the station would operate above 18 voltage. Once below this point, the IV curve would stop being drawn and the sequence would go on to the next step.

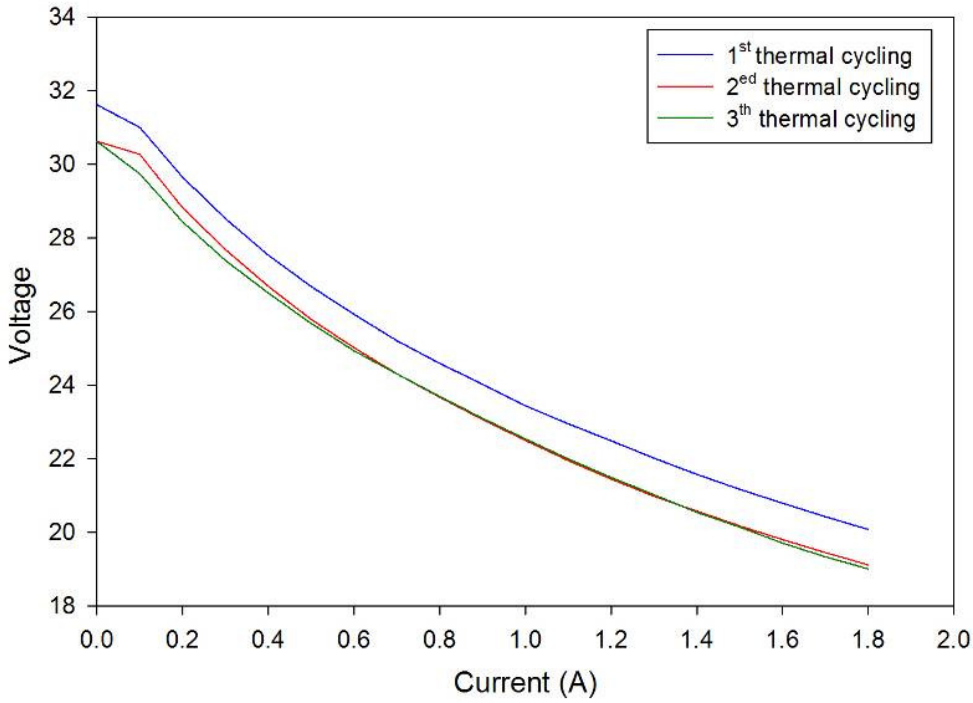

Figure 50: The IV curve for thermal cycling of IP-SOFC.

Comparing between the first and second running of the thermal cycling test, the OCV was reduced slowly from 31.62 V to 30.62 V as shown in Figure 50. The voltage degradation rate was 3.1% at OCV, which then increased with increasing current, until it reached the maximum value of 5.0% at 1.8 A, after three operations. This occurs as a result of increased cathode polarisation resistance over time. This change leads to a voltage drop during the operation of the cell, which results in an increase in Ohmic resistance, because of the cracking in IP-SOFC layers as shown in Figure 51 [156].

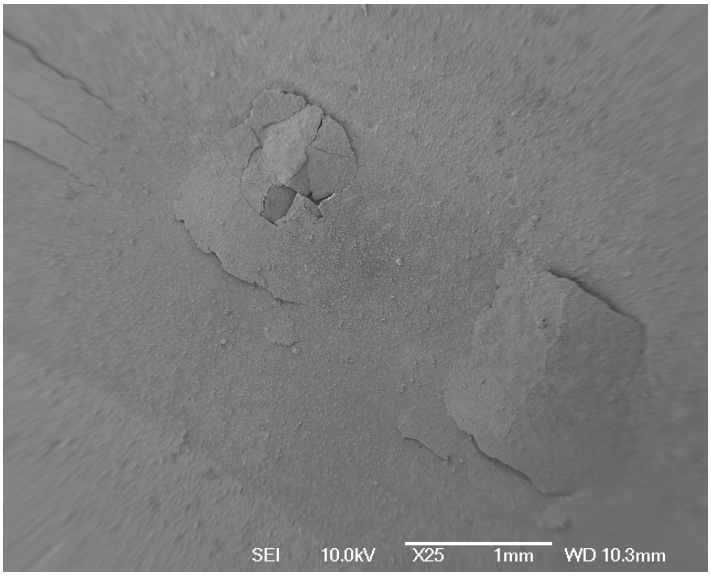

Figure 51: SEM image of IP-SOFC layer.

After three thermal cycles, the voltage of IP-SOFC-1 dropped to zero. To understand the reason for this, the station was switched off and the IP-SOFC-1 was removed from the furnace and checked. Figure 52 shows there were two large cracks on the surface of IP-SOFC. This cracking occurred in both sides of the surface of IP-SOFC-1 and extended though the whole cell; the length of cracking was around 1 cm. This damage was observed through visual inspection. This crack of the IP-SOFC-1 formed during the thermal cycling test finally resulted in a gradually decrease of the IV curve after each test.

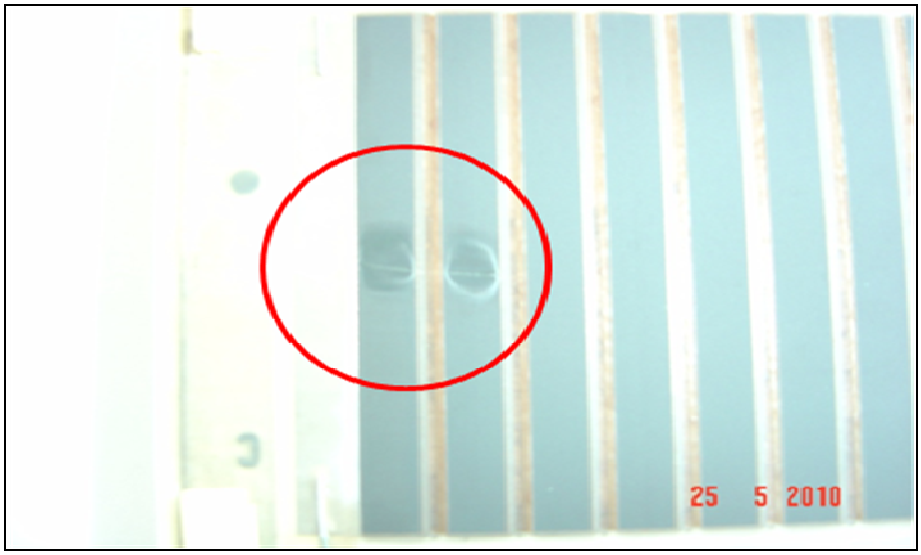

Figure 52: Large cracking on the surface of the IP-SOFC-1.

5.6 Conclusion

In this chapter, an investigation was performed to check the microstructure changes in IP-SOFCs due to the current loading and thermal cycling. The obtained results of IP-SOFC performance was discussed on basis of Ohmic resistance and physical structure changing of fuel cells.

The degradation of IP-SOFC performance observed in these tests may have occurred for many reasons, such as the temperature gradient leading to degradation during a run, with varying expansion coefficients between components, especially in anode materials [193]. Another factor was the increasing Ohmic resistance (as shown in Figure 39), which is likely to occur because of the operation of the cell over a long period, adversely affecting the stability of materials (especially interconnected materials), leading to the degradation of cell performance.

Durability testing of the IP-SOFCs has shown that degradation of the performance

occurs under steady operation and as a result of cycling temperature. IP-SOFCs 2 and 3 ran steadily and gave voltage degradations of 2.11% and 1.43% per 1000 hours of operation, respectively, when operated at a constant current over long period (ca. 1200 hours for IP-SOFC-2 and 6030 hours for IP-SOFC-3). In contrast, the rapid deterioration in the performance of the IP-SOFC-1 seems to have been caused by the accident mentioned above.

In the investigation into the durability of IP-SOFCs, it has been shown that the deterioration of IP-SOFC performance accelerates with increasing Ohmic resistance and damage to the interconnected materials, which must also be taken into account. However, thermal cycling was shown to be a particularly serious problem, with the effect of temperature change resulting in particularly high levels of mechanical damage to IP-SOFC materials, when restarting or cooling. In addition, the restart and shutdown of the IP-SOFC test was also shown to cause serious problems, with oxygen gaining entry to the anode surface, leading to the oxidization of Ni to NiO and resulting in a decreased performance of the IP-SOFC at restart.

Chapter 6

IP-SOFC Operated with Methane

[2] Almutairi, G, A. Dhir and W. Bujalski, Direct operation of IP-Solid Oxide Fuel Cell with hydrogen and methane fuel mixtures, submitted to *Fuel Cells*.

6 IP-SOFC operated with methane

An important advantage of SOFCs is that they can function with alternative hydrocarbon fuels, such as methane, ethanol and carbon monoxide, rather than being solely limited to hydrogen as that to low temperature fuel cells. The hydrocarbons are particularly advantageous over hydrogen fuel, having benefits that include lower cost and ease of storage. For this reason, it is expected that these gases will be the increasingly suitable fuels in the near future. However, the major problem with running hydrocarbons directly in the SOFC is that carbon deposition occurs on the surface of the anode catalyst. The resulting deactivation of electrocatalytic area because of carbon deposition then results in a decreased cell performance.

There are many reactions that are likely to occur for methane with the passing of oxygen ions through the electrolyte [194]. The methane gas at anode and the oxygen ions that pass through the electrolyte to interface the anode/electrolyte cause the following reactions 6-1 to 6-12:

$$CH_4 + 4\ O^{--} \rightarrow CO_2 + 2\ H_2O + 8e^- \qquad 6\text{-}1$$

$$CH_4 + 2\ O^{--} \rightarrow CO_2 + 2\ H_2 + 4e^- \qquad 6\text{-}2$$

$$CH_4 + O^{--} \rightarrow CO + 2\ H_2 + 2e^- \qquad 6\text{-}3$$

$$CH_4 + 2\ O^{--} \rightarrow C + 2\ H_2O + 4e^- \qquad 6\text{-}4$$

The products of these reactions lead to further reactions with the oxygen ions passing through the electrolyte to interface the anode/electrolyte, leading to the following reactions:

$H_2 + O^{--} \rightarrow H_2O + 2e^-$ 6-5

$CO + O^{--} \rightarrow CO_2 + 2e^-$ 6-6

$C + O^{--} \rightarrow CO + 2e^-$ 6-7

$C + 2\,O^{--} \rightarrow CO_2 + 4e^-$ 6-8

As a result of the presence of available gases, there can be other competing reactions, the most common of which are Equations 6-9 and 6-10, which form on the anode surface. In addition, the pyrolysis of hydrocarbon as in Equation 6-11 can form carbon on the anode and the resulting carbon deposition can be removed by reaction in Equation 6-12. All these reactions are shown below [194]:

$H_2O + CO \rightarrow H_2 + CO_2$	Water gas shift	6-9
$2CO \rightarrow C + CO_2$	Boudouard reaction	6-10
$CH_4 \rightarrow C + 2H_2$	pyrolysis	6-11
$C + H_2O \rightarrow CO + H_2$	steam gasification	6-12

So, after evaluating the IP-SOFC performance with pure hydrogen, this chapter presents a series of experiments that sought to test the IP-SOFC with mixture fuels containing various methane contents, thus forming a baseline for a comparison between two types of fuels for IP-SOFC operation.

6.1 Testing profile

6.1.1 Effect of CH_4 on IP-SOFC

In the first experiment, the effect of CH_4 on the degradation of the IP-SOFC-2 was studied by operating the fuel cell at 900 ^oC with various H_2 – CH_4 fuel mixtures as

shown in Table 8. The furnace was heated from ambient temperature to 400 ^{o}C at a rate of 1 ^{o}C per minute with 1.425 litres per minute N_2 and 0.075 litres per minute H_2. After the furnace temperature reached 400 ^{o}C, the fuel was changed to pure hydrogen and the furnace temperature was increased further to 900 ^{o}C at the same rate of 1 ^{o}C per minute. When the IP-SOFC temperature reached 900 ^{o}C, the fuel cell was operated for 24 hours using pure H_2 until a steady voltage was reached and the IV curve was recorded as a reference.

After this stage, CH_4 was introduced. The volume flow rate of H_2 was decreased while that of CH_4 was increased to achieve various fuel compositions as shown in Table 8 while the total volume flow rate of fuel mixtures was kept constant at 1.5 litres per minute.

Every run tested four fuel mixtures. For each fuel mixture, the IP-SOFC was operated for 2 hours and then the IV curve was recorded. The humidity of H_2 and H_2-CH_4 fuel mixtures were set to 3%, in accordance with the operating conditions recommended by the manufacturers. At the end of each run, the IP-SOFC was shut down and the temperature lowered to room temperature at a cooling rate of 1 ^{o}C per minute. This procedure was repeated four times.

Table 8: Mixture flow rates for hydrogen and methane.

Composition	Hydrogen flow rate (litres per minute)	Methane flow rate (litres per minute)
100% H_2	1.500	0.000
95% H_2 + 5% CH_4	1.425	0.075
90% H_2 + 10% CH_4	1.350	0.150
85% H_2 + 15% CH_4	1.275	0.225
80% H_2 + 20% CH_4	1.200	0.300

Steam gasification:

$C + H_2O \rightarrow CO + H_2$ 6-13

Oxidation:

$C + 1/2\ O_2 \rightarrow CO$ 6-14

$C + O_2 \rightarrow CO_2$

In this experiment, steam gasification was used to remove the carbon from the TPB at the anode surface at the end of run 2. During steam gasification, the humidifier was set at 5%, instead of 3% during operation, for 3 hours before run 3 was started.

At the end of run 3, the carbon deposition was not removed by using oxidation method. Air, rather than oxygen, was used for this purpose. The first step in this process was to ensure that all gas connections in the test station were cleaned of

hydrogen to avoid any risks from explosive reaction between hydrogen and oxygen. This was achieved by flowing 10 litres per minute of nitrogen for 10 minute. Subsequently, 3 litres per minute of air was fed to the anode side for re-oxidisation for 5 min, and then nitrogen gas was used again to avoid the previous problem. The humidity during oxidation process was set at 3 %.

6.1.2 Current load cycle

In the second experiment, the effect of current load cycle on the durability of IP-SOFC-3 was studied. Two fuel mixtures were used in this study, i.e. 95% H_2 – 5% CH_4 and 80% H_2 – 20% CH_4. The furnace was heated from room temperature to 900 ^oC using the same method as described previously. Initially, the IP-SOFC was fed with pure H_2 for 48 hours at a current load of 1 A and the IV curve was recorded as a reference. Subsequently, the IP-SOFC-3 was fed with the first fuel mixture, i.e. 95% H_2 – 5% CH_4, at the same flow rate and operated for 48 hours at a current load of 1 A. The current load was then decreased to 0.0 A for 30 minute. This load cycle with 95% H_2-5% CH_4 fuel mixture was repeated seven times. The fuel was then changed to pure H_2 again and the IP-SOFC-3 was operated at a current load of 1 A for 48 hours. The fuels flow rates were maintained at 1.5 L per minute and the IV curve was recorded throughout the experiment. Finally, the furnace was cooled down to room temperature at a cooling rate of 1 ^oC per minute to inspect visually any signs of damage on the IP-SOFC. This procedure was repeated one more time with the same fuel mixture, i.e. 95% H_2 – 5% CH_4. At the end of the second run, the IP-SOFC-3 was cooled down to room temperature.

After the IP-SOFC-3 had been operated for 800 hours using the first fuel mixture (95% H_2 and 5% CH_4), the experiment was carried out with the second fuel mixture comprised of 80% H_2 and 20% CH_4. The total flow rate of the fuel mixture and other operating conditions were the same as those in the experiment with first fuel mixture. The current load cycle was only repeated 2 times and the IV curves were recorded for every current load cycle in order to assess the performance (degradation) of IP-SOFC-3. At the end of load current cycles, the fuel was changed from 80% H_2 and 20% CH_4 fuel mixture to pure H_2 and the experiment was run for 48 hours and then IV curves were recorded for comparison purpose.

6.2 Results and Discussions

6.2.1 Effect of CH_4 on the performance of IP-SOFC

Figure 53 shows the effect of CH_4 concentration on the polarization of the IP-SOFC-2 operated with H_2 – CH_4 fuel mixtures in the first run. In all CH_4 concentrations, the voltage of the IP-SOFC-2 falls gradually as the current passing to the cell increases due to polarization. However, the voltage of the IP-SOFC increases with higher CH_4 concentration. The OCV of IP-SOFC-2 running on 80% H_2 – 20% CH_4 fuel mixture is 15.6% higher than that running on pure H_2 as shown in Table 9. This increase in OCV is as expected since the change in the Gibbs free energy (ΔG^o) and standard equilibrium voltage for methane is higher than that for hydrogen, as shown in Table **9**. The standard equilibrium voltage, considered as the OCV (E^o), can be evaluated from the following Equation 6-15:

$$E^o = -\frac{\Delta G^o}{nF}$$ 6-15

where *n* is the molar number of electrons being transferred and *F* is Faraday's constant.

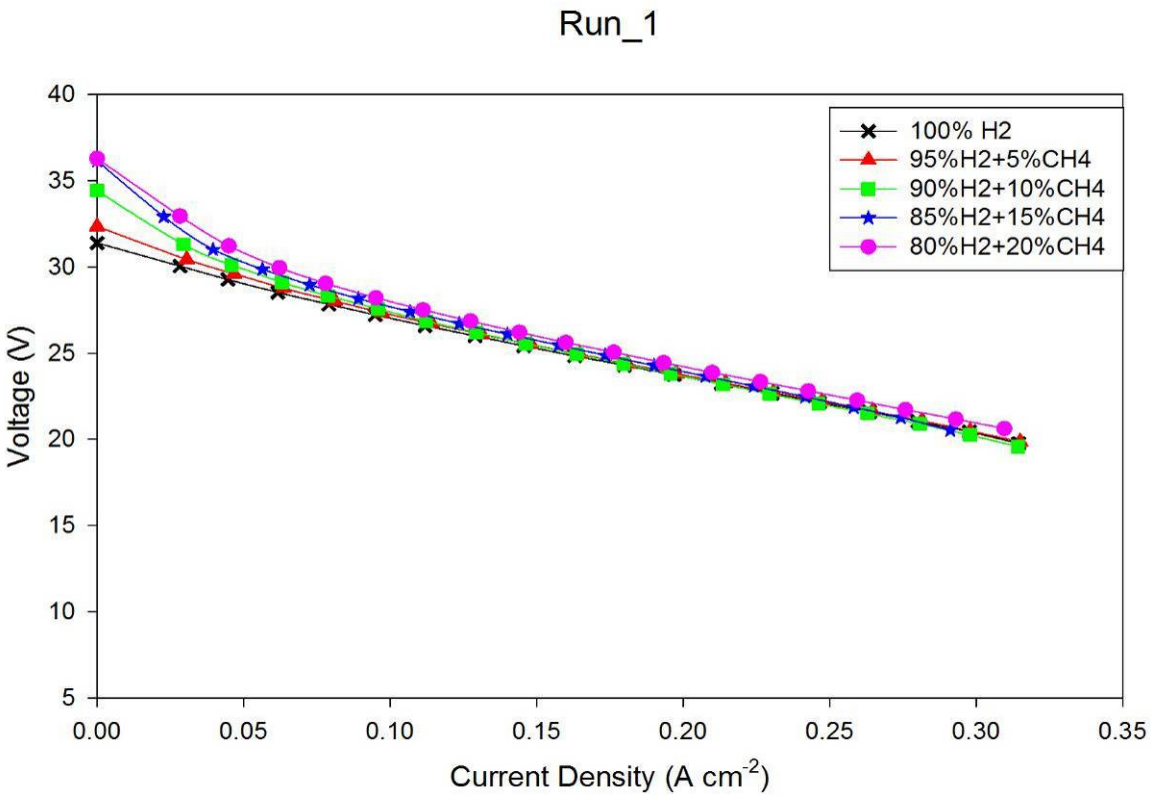

Figure 53: Effect of CH_4 concentration on the polarization curve of IP-SOFC-2 in the first run.

Table 9: Overall chemical reaction and change in Gibbs energy.

	Methane	Hydrogen
Overall Reaction	$CH_4 + 2\ O_2 \rightarrow CO_2 + 2\ H_2O$	$H_2 + 1/2\ O_2 \rightarrow H_2O$
ΔG^o	-818 kJ mol^{-1}	-237 kJ mol^{-1}
E^o	1.41 V	1.23 V

However the voltage differences between IP-SOFC-2 operated with H_2 – CH_4 fuel

mixtures and that with pure H_2 decrease as the current densities increase (Figure 53). At 0.2 A per cm^2, the voltage difference between 80% H_2 + 20% CH_4 fuel mixture and pure hydrogen is only around 0.64 V compared to 4.90 V at OCV. At the maximum current applied (1.8 A, with current density of 300 mA per cm^2), the voltage difference between the fuel mixture containing 20% CH_4 and pure hydrogen was only 4.1%. At smaller CH_4 concentrations (5, 10 and 15%), however, the voltage differences with that of pure H_2 are less than 1% as shown in Table 10.

Table 10: Open circuit voltage (OCV) and voltage at maximum current of IP-SOFC-2 operated with H_2-CH_4 fuel mixtures

Fuel Regime	**At OCV**			**At 1.8 A (Max Current)**		
	Total voltage (V)	Voltage/ cell (V $cell^{-1}$)*	% increase	Total voltage (V)	Voltage/ cell (V $cell^{-1}$)	% increase
H_2	31.39	1.04	-	19.77	0.659	-
95%H_2 – 5% CH_4	32.35	1.08	3.1%	19.87	0.662	0.5%
90%H_2 – 10% CH_4	34.42	1.15	9.7%	19.88	0.662	0.5%
85%H_2 – 15% CH_4	36.16	1.21	15.2%	19.89	0.663	0.6%
80%H_2 – 20% CH_4	36.29	1.21	15.6%	20.62	0.687	4.1%

*Number of cells = 30

The polarization of the IP-SOFC-2 fuel cell tends to decrease with the number of run as shown in Table 11. The decline in voltage in the second run compared to that in the first run is because of the carbon deposition on the surface of the anode. The deposited carbon particles block the pores on the anode deactivating the catalyst. However, Figure 54 shows that there seems to be no evidence of micro-cracking and

also because the OCVs are very similar in the first and second run.

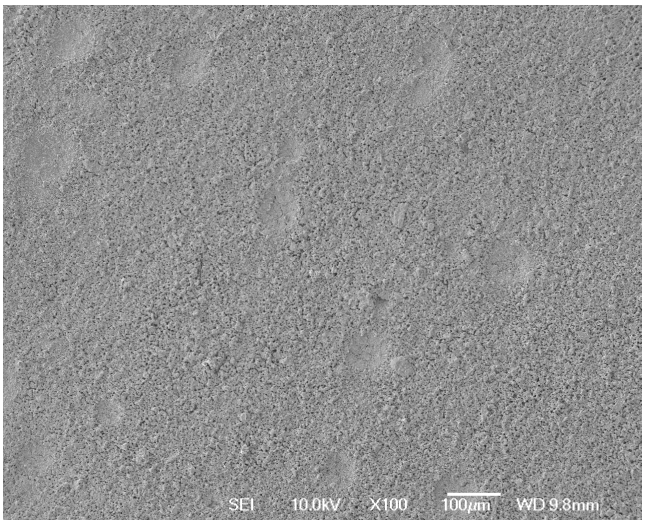

Figure 54: SEM image of IP-SOFC-2

Table 11: The results of the OCV and the voltage at maximum current (1.8 A) for run 1, 2 and 3.

% Flow rate	100% H_2		95% H_2 + 5% CH_4		90% H_2 + 10% CH_4		85% H_2 + 15% CH_4		80% H_2 + 20% CH_4	
	OCV	V **	OCV	V **	OCV	V **	OCV	V **	OCV	V **
1st run	31.4	19.8	32.4	20.0	34.4	19.9	36.2	19.9	36.3	20.6
2nd run	31.3	19.0	32.3	19.5	34.6	18.0	35.4	17.6	35.7	16.3
3rd run	30.6	16.6	31.2	16.5	33.2	16.0	34.0	14.2	34.0	11.7
Deg.. rate %	2.5	16.0	3.3	16.9	3.6	18.1	5.9	23.8	6.4	43.5

** Voltage (V) at maximum current (1.8 A)

The third run was carried out after carbon removal step with steam gasification,

however, the IP-SOFC-2 did not show any improvement in performance. In fact, the performance of IP-SOFC-2 in the third run is worse than that in the second run as shown in Table 11. The reduction in OCV in the third run is relatively small, i.e. only 2.5% for pure H_2 and 6.4% for 80% H_2 – 20% CH_4 fuel mixture. However, there is significant voltage reductions at the highest current of 1.8 A. For pure H_2, the voltage at the highest current decreases by about 16% in the third run compared to that in the first run, however, at the highest CH_4 concentration, the voltage decreases by 43%. The high methane concentration (80% H_2 + 20% CH_4) seems to have caused continual carbon deposition on the surface of the anode especially at the highest current since the reaction rate is the fastest.

Although the fourth run was carried out after carbon removal step by oxidation, the performance of IP-SOFC-2 decreased at a faster rate especially at the highest current. The results are shown in Figure 53.

The reductions in OCV for all fuel mixtures in the fourth run are about 10% lower than that in the first run while those in the second and third runs are less than 5 – 6%. At the maximum current, the voltage decreases by 55% for pure H_2 compared to that in the first run and by 52% for 80% H_2 – 20% CH_4 fuel mixture. The maximum voltage and current of the IP-SOFC-2 in the fourth run are only around 10 V and 1.2 A, respectively, corresponding to the maximum power of about 12 W (Figure 55).

This is much lower compared to about 37 W in the first run. Cracking on the IP-SOFC-2 layers near the fuel inlet region (Figure 56 and Figure 57) were observed after the fourth run and this contributes significantly to the degradation of IP-SOFC-2 in addition to carbon deposition.

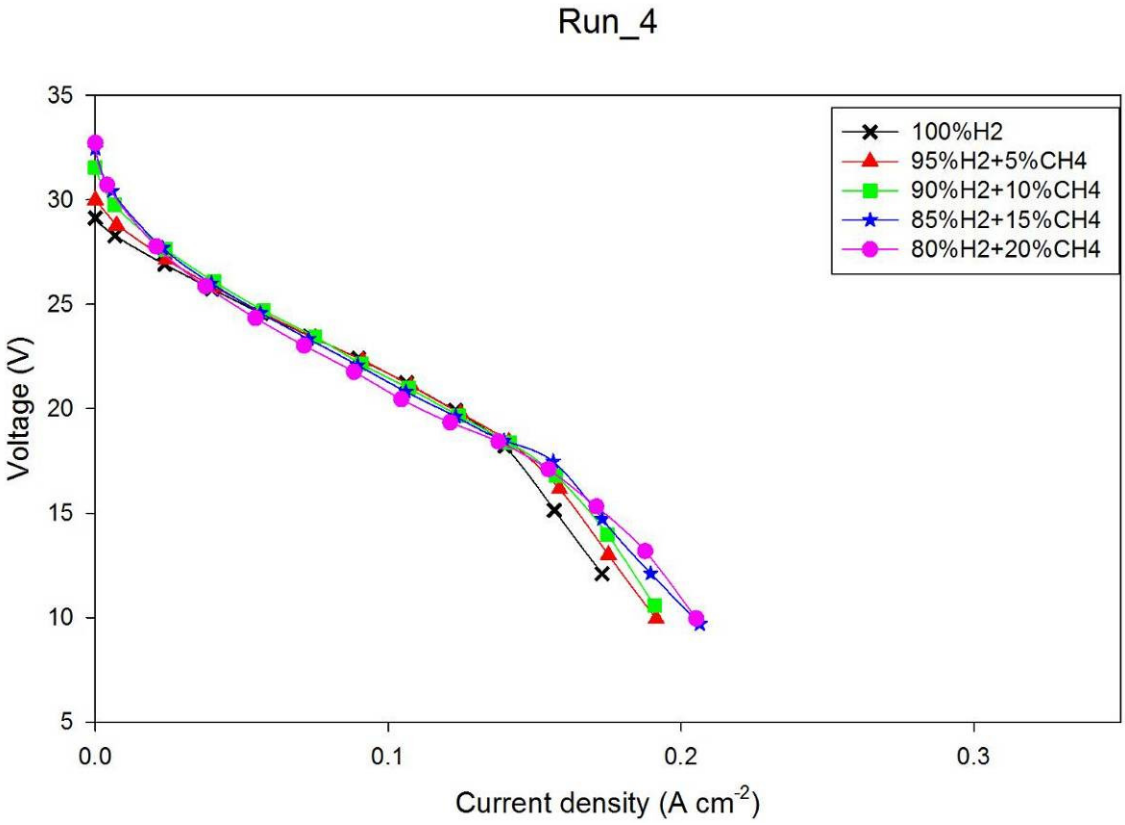

Figure 55 : Run 4 for IP-SOFC-2 with different fuel mixtures

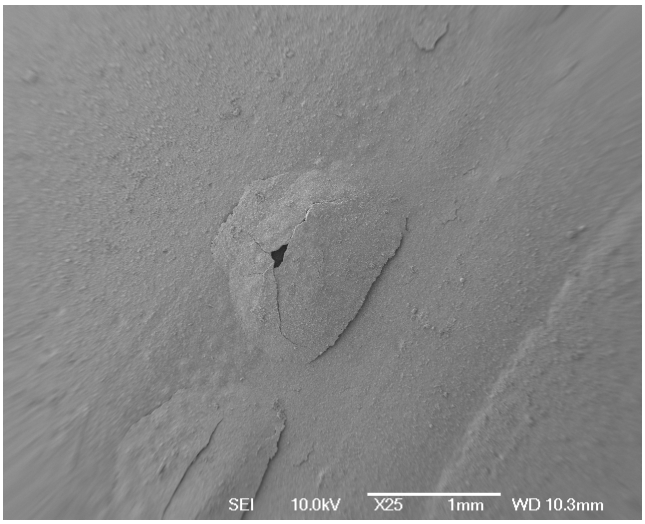

Figure 56: cracking on IP-SOFC caused Carbon deposition.

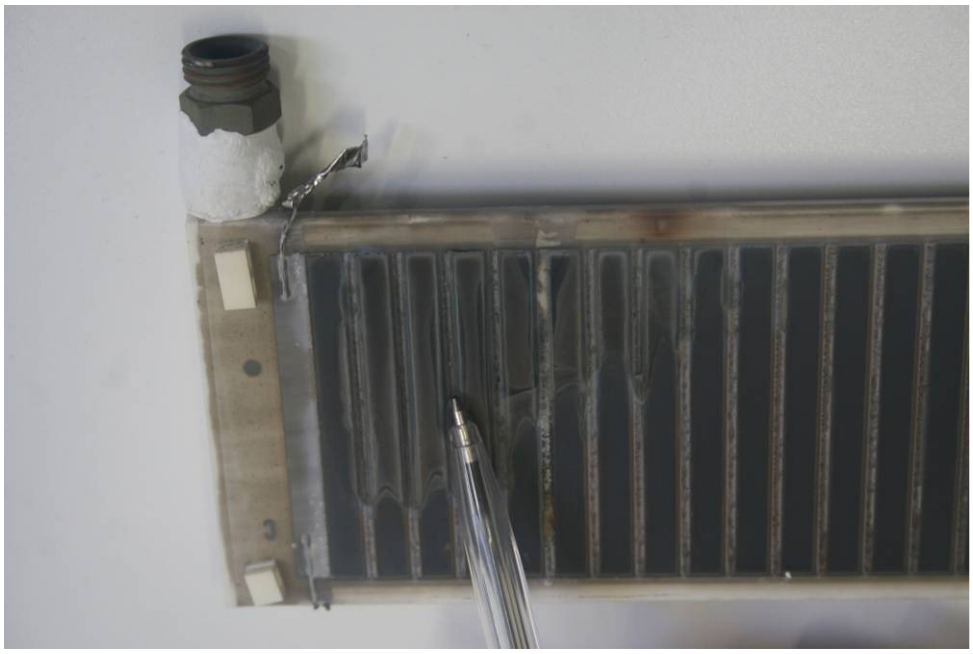

Figure 57: Cracking on IP-SOFC-2 layer.

This may have occurred because the IP-SOFC was printed on a porous ceramic support that has great resistance to the flow of fuel to reach the anode surface as shown in Figure 58. The accumulation of products, especially carbon, increases the resistance in the ceramic support creating fuel leakage to the cathode side. The leaked fuel will increase furnace temperature as it reacts with oxygen. As a result, the LSM in the cathode will react with the YSZ electrolyte [50] creating cell damage as shown in Figure 57.

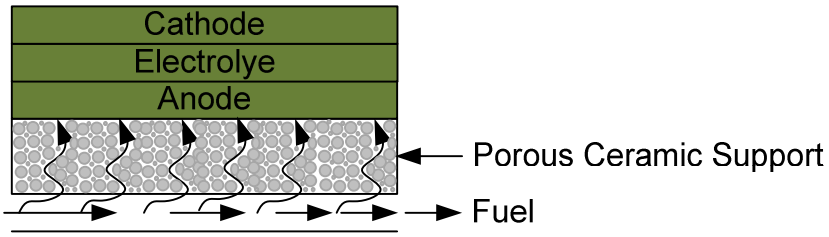

Figure 58: Fuel direction in the porous ceramic support of the IP-SOFC.

6.2.2 Effect of current load cycle on the durability of the IP-SOFC with 95% H_2 – 5% CH_4 fuel mixture

Figure 59 shows the polarization curves of the IP-SOFC-3 operated with 95% H_2 and 5% CH_4 fuel mixture. The polarization curves of the IP-SOFC operated with H_2 before and after current load cycles with H_2-CH_4 fuel mixture are also shown as reference (1st and 9th curves). The difference of the OCVs between the pure hydrogen and fuel mixture is very small which is in agreement with previous results. The OCV was 31.5 V when the IP-SOFC-3 is operated with pure hydrogen and 32.5 V when it is operated with a 95%H_2 – 5% CH_4 fuel mixture. This difference is due to the change in Gibbs free energy (ΔG^o) for methane and hydrogen as explained previously, and therefore, the small differences in the OCV are due to low concentration of CH_4 in the fuel mixture. Figure 59 shows that all the IV curves between runs are also very similar at current densities between 0.05 and 300 mA per cm^2 indicating that the IP-SOFC does not have any sensitivity to a low methane concentration in the fuel mixture (95% H_2 - 5% CH_4) when operated for the first time. No degradation on the performance of the IP-SOFC is observed over 490 hours cycling operation when the CH_4 concentration in the fuel mixture is low.

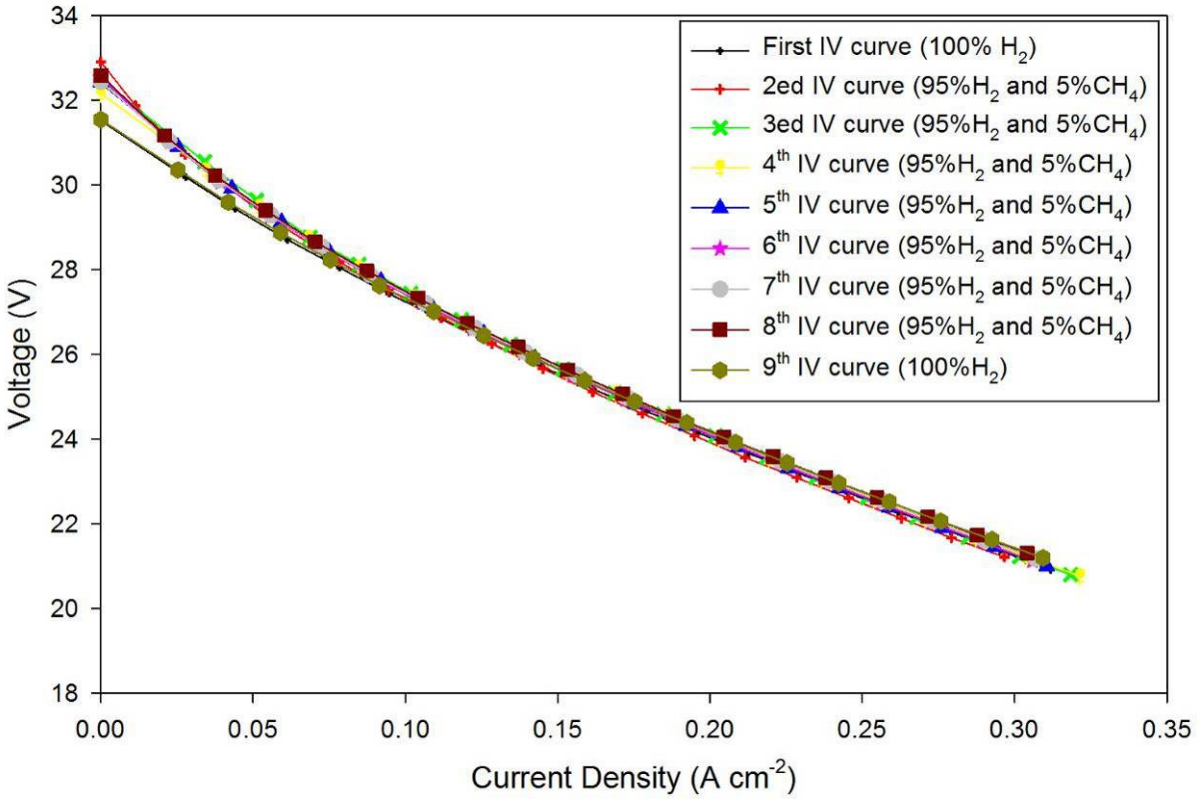

Figure 59: IV curves of the IP-SOFC-3 operated with 95% H_2 and 5% CH_4 during the first run of load cycling test.

The polarization curves of IP-SOFC-3 operated with 95%H_2 – 5% CH_4 fuel mixture in the second run are shown in Figure 60. The polarization curves with pure H_2 are also shown as the reference. As shown in Figure 59, the OCVs are stabile similar to those in the first run, where the OCVs were 31.5 V for pure hydrogen and 32.45 V for 95% H_2-5% CH_4 fuel mixture fuel. In addition, all IV curves were stable until the current density reached 150 mA per cm^2. However, a minimal difference was observed at maximum current density, where the voltage was 20.5 and 19.5 V in the 2^{nd} and 5^{th} IV curves, respectively. This suggests that the IP-SOFC-3 starts to degrade after 800 hours when 95% H_2 – 5% CH_4 fuel mixture is used.

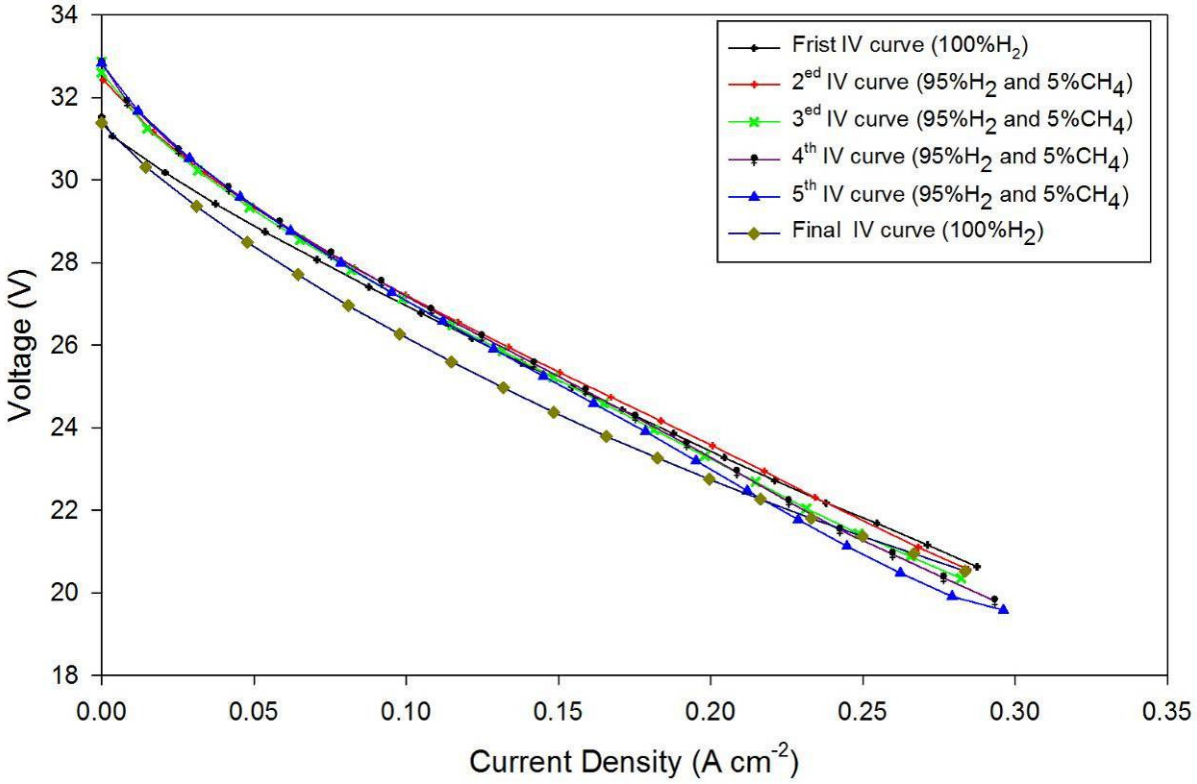

Figure 60: IV curves of the IP-SOFC-3 operated with 95% H_2 and 5% CH_4 during the second run of load cycling test.

A comparison of IV curves with pure H_2 between the first and second run is shown in Figure 61. The red curve represents the final IV curve recorded at the end of first run, while the blue curve represents the first IV curve for the second run. The OCVs are almost the same at 31.5 V, however, there is a relative large difference at high current density between the final IV curve of the first run (21.68 V) and that of the second run (20.68 V) after one time run for 800 hours. This was likely due to the impact of the fuel mixture on the performance of the IP-SOFC-3. The degradation of the IP-SOFC-3 performance is acceptable considering that the IP-SOFC-3 contains 30 small cells and therefore the voltage degradation at high current density is 3% per cell.

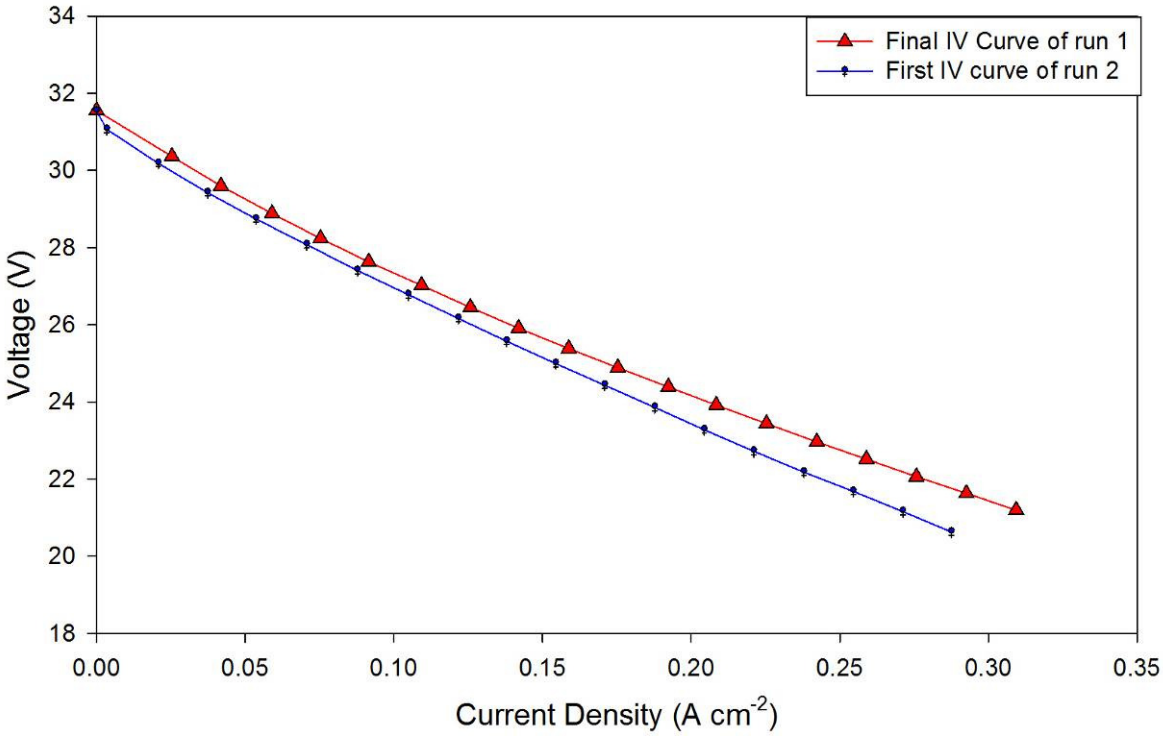

Figure 61: A comparison between IV curves in run 1 and run 2.

The durability test of the IP-SOFC-3 was conducted by running on the fuel mixture (95% H_2 and 5% CH_4) under a constant current of 1 A (170 mA per cm^2). This took more than 800 hours, including 16 current load cycles and two restarts and shutdowns. It can be seen from Figure 62 that the OCV has almost no change, giving the impression that there were no leaking of gas. However, there was approximately 10.3% degradation in voltage at maximum current of 1.8 A. The degradation in the voltage occurs at the beginning of the second run of current load cycle (after 490 hours) and this could be due to temperature shock during restart and shutdown between the first and second runs although the heating and cooling have been carried out at 1 ^oC per minute.

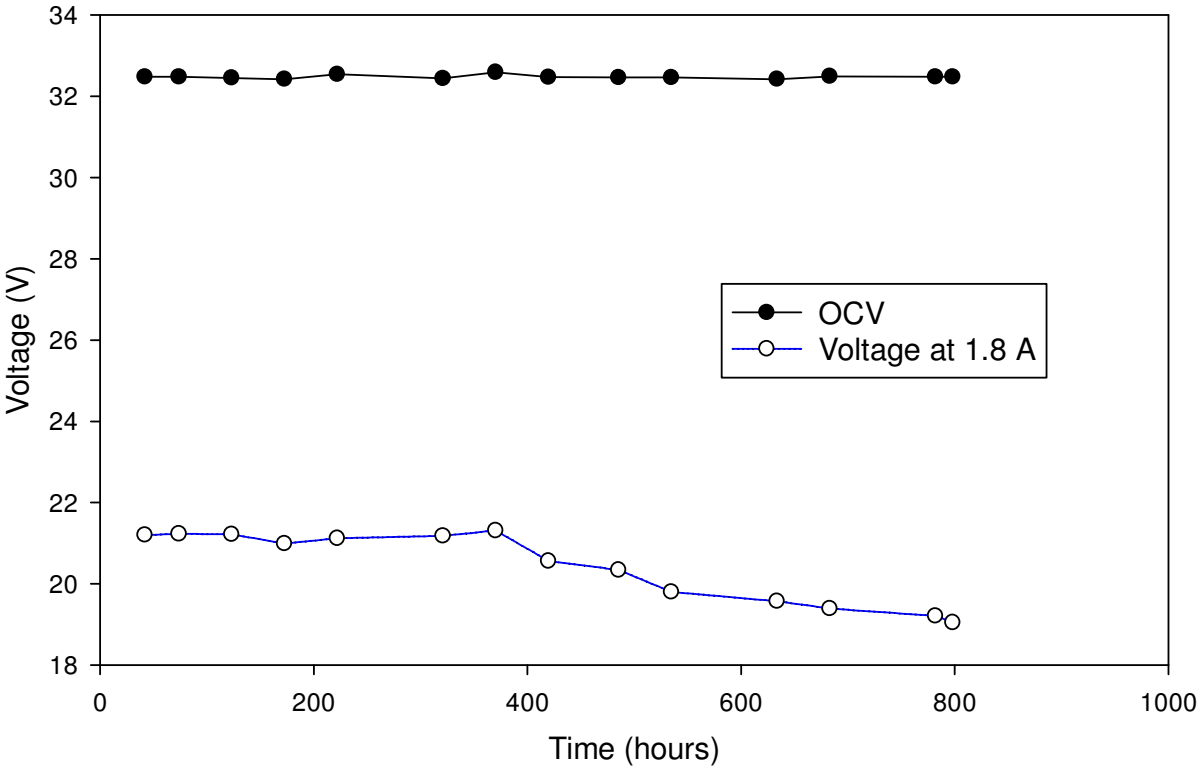

Figure 62: OCV and voltage at a maximum current of 1.8 A as a function of time.

6.2.3 Effect of current load cycle on the durability of the IP-SOFC with 80%H_2 – 20%CH_4 fuel mixture

After the IP-SOFC-3 had been operated for 800 hours using the first fuel mixture (95% H_2 and 5% CH_4), the fuel was replaced with the second mixture comprising of 80% H_2 - 20% CH_4. Figure 63 shows the average output voltages of the IP-SOFC-3 at a constant current of 1 A during the first and second load cycles with 80% H_2 – 20% CH_4 and the final stage with pure H_2 for a short period of time (around 5 hours) marked by a green circle. The first cycle gave the best average voltage around 25.7 V at a constant current of 1 A for a period 48 hours. In the second load cycle the voltage decreased to 18.48 V at a constant current of 1 A. The voltage decreased further by 1 V when the IP-SOFC-3 was operated with pure H_2 at the final

stage (marked by green circle).

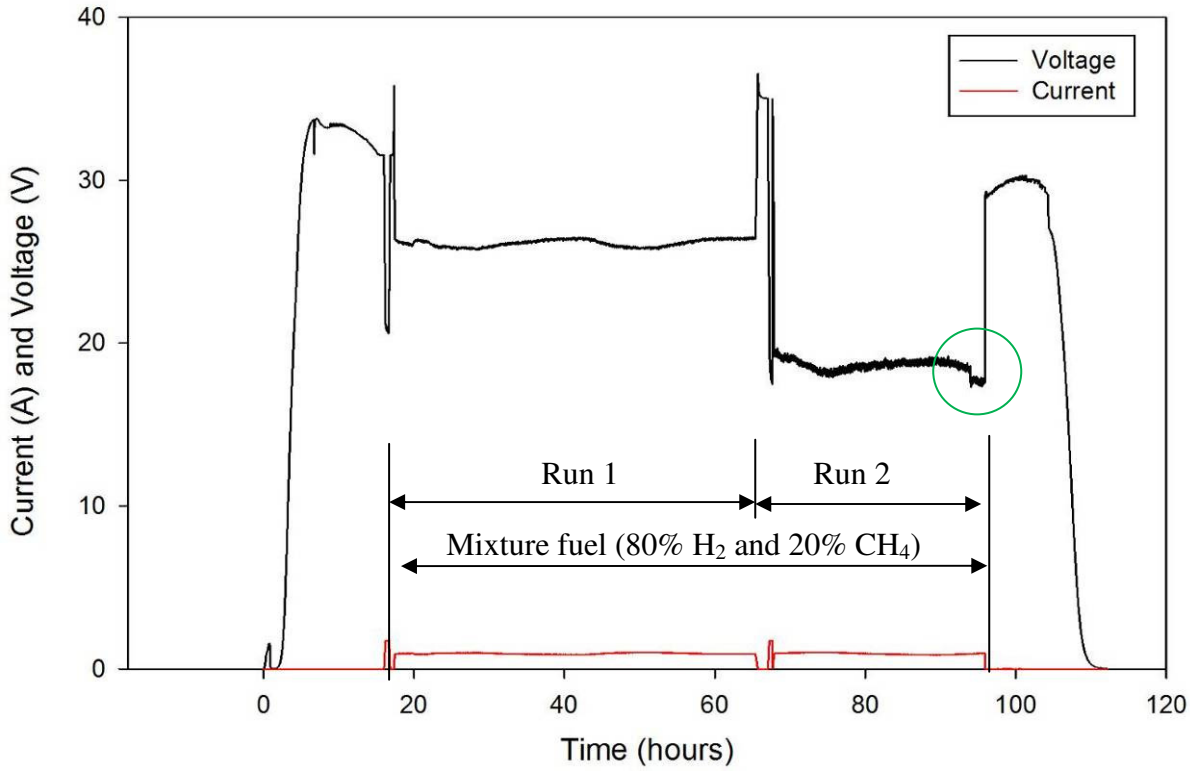

Figure 63: Currents and voltages of IP-SOFC-3 during the first and second runs with 80% H_2 - 20% CH_4 fuel mixture and final stage with pure H_2 (marked by green circle).

Figure 64 shows the IV curve for the first load cycle with 80% H_2 and 20% CH_4 (after 48 hours of operation) (red curve) and that for pure H_2 (blue curve) after the second current load cycle.

There is a significant 10.6% increase in the OCV when the IP-SOFC-3 is operated with the 80% H_2 - 20% CH_4 fuel mixture instead of the pure H_2. The OCV is 31.7 V when the IP-SOFC-3 is operated using pure hydrogen, whereas it is 35.05 V when it is operated with the fuel mixture due to a change in Gibbs free energy (ΔG^o) for

methane and hydrogen as mentioned previously. However, the increase in OCV is lower compared to those in Table 10 where the OCV of IP-SOFC-3 operated with 80% H_2 – 20% CH_4 is about 15% higher than that operated with pure H_2.

The IV curve of the mixed fuel was also shown to be higher than the IV curve of pure hydrogen, but at a current density higher than 240 mA per cm^2 the IV curve of the fuel mixture started to decline significantly due to carbon deposition on the anode surface as explained previously.

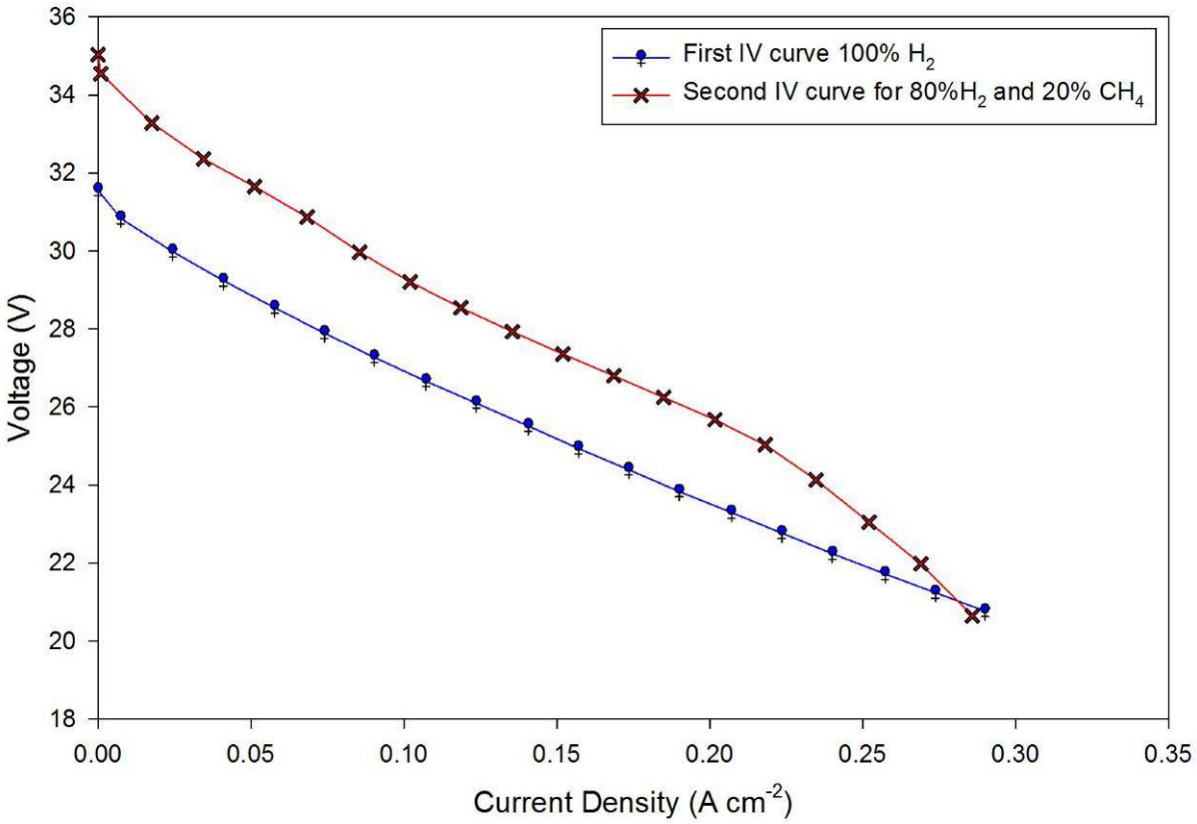

Figure 64: IV curves for 80% H_2 and 20% CH_4.

Figure 65 shows the comparisons of current and voltage of IP-SOFC-3 operated with 95% H_2 - 5% CH_4 and 80% H_2 - 20% CH_4 fuel mixtures. No change in voltage is observed in the beginning of both tests when the IP-SOFC was restarted and operated with pure H_2 for 15 hours. However, the voltage of the IP-SOFC-3 operated with 80% H_2 – 20% CH_4 fuel mixture at a constant current of 1 A is around 26.47 V, whereas that with 95% H_2 – 5% CH_4 fuel mixture is only 23.89 V. This represents about 11% increase in the IP-SOFC output voltage. However, the durability of the IP-SOFC-3 decreases drastically when 80% H_2 – 20% CH_4 fuel mixture is used. Decrease in the voltage is observed in the second run with 80% H_2 – 20% CH_4 fuel mixture, whereas the voltage is stable up to 7 cycles with 95% H_2 – 5% CH_4 fuel mixture (Figure 62). In addition, the OCV also increase slightly from 33.15 V to 35.05 V when the CH_4 concentration in the fuel mixture is increased from 5% to 20% (Figure 65).

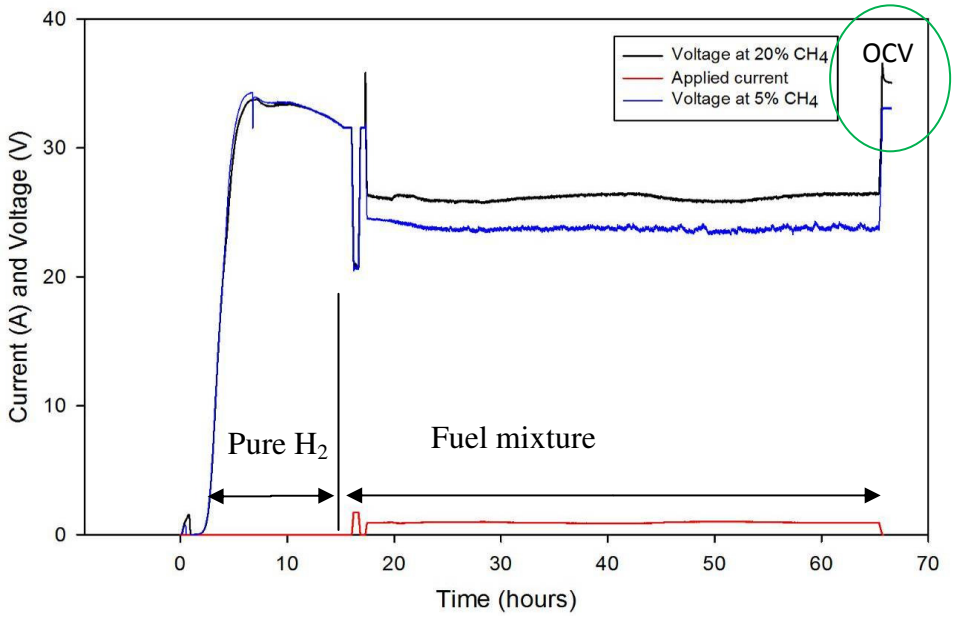

Figure 65: Comparisons of current and voltage of IP-SOFC-3 operated with 95% H_2 - 5% CH_4 and 80% H_2 - 20% CH_4 fuel mixtures.

This IP-SOFC-3 after operating with methane was cut into pieces to analyse carbon deposition, which will be discussed in greater detail in chapter 7. In addition, the analysis of the exhaust gas will be discussed in next section.

6.3 Exhaust gas analysis

As discussed above, the fuel mixture (hydrogen and methane) reactions occurred on the anode (as shown above). The anode consists of Ni metal, one of the well-known commercial catalysts for this type of reaction.

Figure 66 shows the exhaust gas analysis for helium and hydrogen at room temperature, where the anode IP-SOFC exhaust gas was connected to an online mass spectrometer running on a helium flow rate of 20 millilitres per minute and a hydrogen flow rate of 7 millilitres per minute. The mass spectrometer recorded the data every 3 seconds, with a scan time period comprising more than four hours. This test was performed to confirm that the anode IP-SOFC exhaust gas did not contain an air leak in the system, as this would have affected the exhaust gas analysis. The exhaust gas analysis result shows that it contains 0.75% helium and 0.25% hydrogen, as can also be calculated from the flow rate.

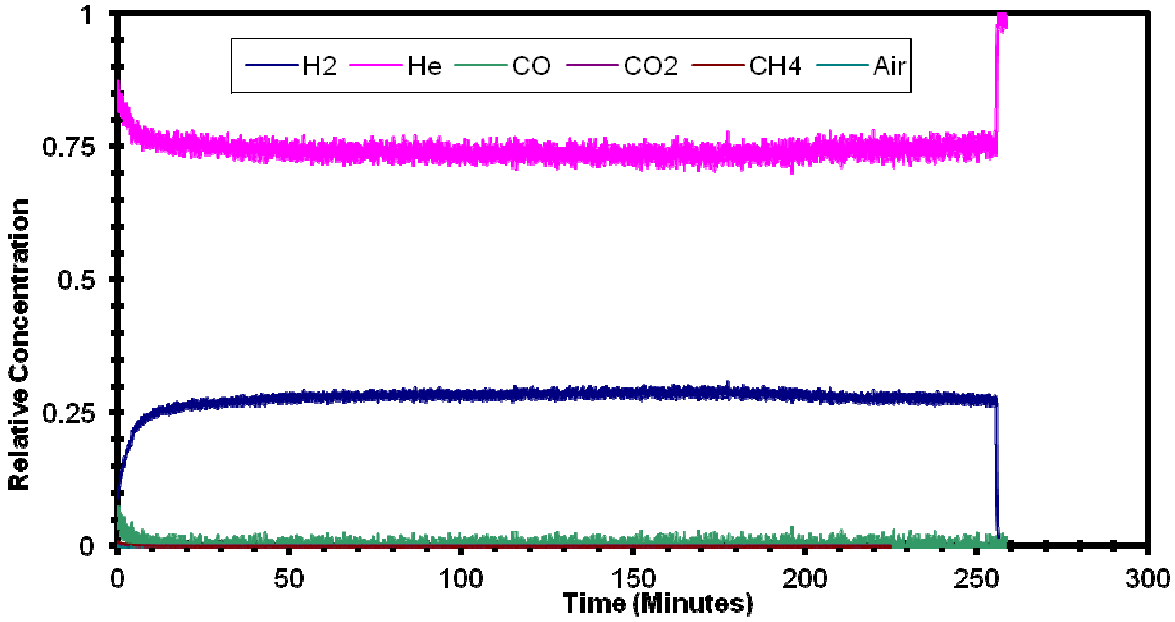

Figure 66: Exhaust gas analysis for helium and hydrogen at room temperature.

As discussed above, methane gas reacts with oxygen ions to produce water, carbon monoxide, and carbon dioxide, and is also likely to produce carbon leading to carbon deposition. Figure 67 shows the exhaust gas analysis for helium and the fuel mixture, where the IP-SOFC-3 was operated at 900 ^{o}C with an online mass spectrometer running on a helium flow rate of 20 millilitres per minute and a fuel mixture flow rate of 7 millilitres per minute. The mass spectrometer recorded the data every 3 seconds, meaning that each scan time period represents more than one day.

It is clear from Figure 67 that the exhaust gas analysis result shows that it contains hydrogen, carbon monoxide, methane and very little carbon dioxide, where the methane gas produces carbon monoxide and carbon dioxide. Particular attention should be paid to the area highlighted by the red circle, which demonstrates that the amount of carbon monoxide decreases at OCV, because the current load is zero and the number of oxygen ions decrease.

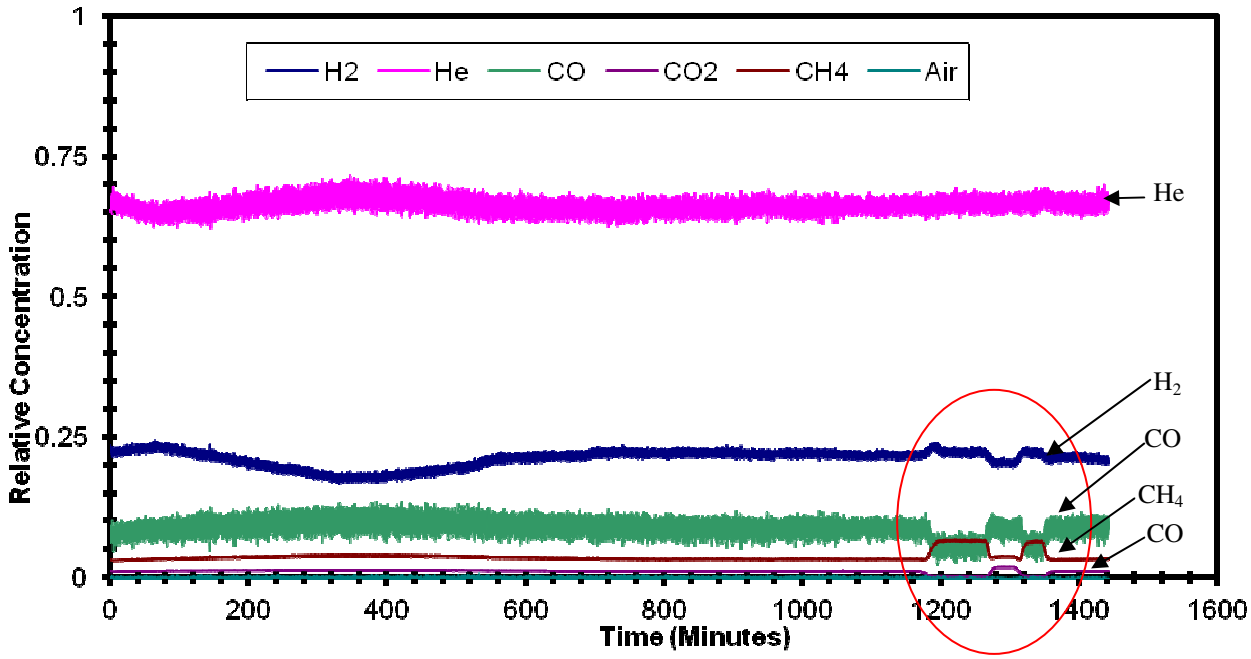

Figure 67: Exhaust gas analysis for helium and fuel mixture at 900 °C.

6.4 Conclusion

In order to investigate the degradation behaviour of the IP-SOFC, it was operated using the hydrogen-methane fuel mixture with up to 20% methane concentration at 900 °C. During short term operation, high methane concentration increased the voltage of the IP-SOFC. However, it degraded the performance of the IP-SOFC in long term operation, which is probably attributable to carbon deposition on the anode surface.

Durability tests using various fuel mixtures of H_2 and CH_4 have demonstrated that the degradation of the IP-SOFCs performance occurs under steady operation and as a result of cycling. The current load cycle tests were conducting using 95% H_2 – 5%

CH_4 and 80% H_2 – 20% CH_4 fuel mixtures at 900 ^oC with a constant current of 1 A. At low methane concentrations (5 % CH4), the decrease in the IP-SOFC voltage was observed after nine current load cycles (400 hours). At higher methane concentration (20% CH4), the voltage of IP-SOFC decreased by almost 30% after just one current load cycle (48 hours), due to more rapid carbon deposition. This degradation occurred due to the formation of solid carbon deposits inside the pores of the anode, which impeded fuel diffusion and electrochemical reaction on the anode side in the IP-SOFC.

Due to the IP-SOFC being constructed from a porous ceramic support, the removal of carbon is very difficult and complex. Both steam gasification and oxidation methods have been proven to be ineffective. Further work must therefore be performed to investigate the mechanisms of carbon deposition on Ni/YSZ anode of IP-SOFC.

Chapter 7

Carbon deposition

[3] Almutairi G., A. Dhir and W. Bujalski, *Analysing carbon deposition on Ni/YSZ anode of Integrated Planar Solid Oxide Fuel Cell (IP-SOFC)*, submitted to *Journal of Power Sources*.

7 Carbon deposition

The previous chapter demonstrated that the performance of the IP-SOFC, which utilises a Ni/YSZ based anode, is affected over time using a hydrogen-methane mixture fuel. This process produces carbon, which deposits on the surface of the anode and blocks the area of activation for important reaction processes. The aim of this chapter is therefore to characterize the carbon that is formed as a result of the presence of the methane in the mixture fuel. The amount and distribution of deposited carbon is studied and analysed through all parts of the IP-SOFC cells, in order to better understand the behaviour of this technology and support future development in this area.

Carbon deposition occurs due to the fact that Ni is an excellent catalyst for these kinds of reactions, such as methane cracking (Equation 7-1), reduction of carbon monoxide (Equation 7-2) and disproportionation of monoxide (Equation7-3). As a result, Ni catalysts can be deactivated by the carbon deposited, resulting in rapid cell degradation [127].

$$CH_4 \rightarrow C + 2H_2 \qquad 7\text{-}1$$

$$CO + H_2 \rightarrow C + H_2O \qquad 7\text{-}2$$

$$2CO \rightarrow C + CO_2 \qquad 7\text{-}3$$

7.1 Experiment

As the IP-SOFC has a ceramic support, a high speed diamond cut-off saw was used to cut the IP-SOFC into small parts (Figure 69) to enable appropriate testing and to give comprehensive, detailed results. The IP-SOFC consists of 30 cells; the cell numbers 5, 10, 15, 20, 25, and 29 were cut into two pieces, as shown in Figure 68.

One piece was used as the top cell and the second piece as the bottom cell. The effective cell area of one such piece is approximately 3 cm^2.

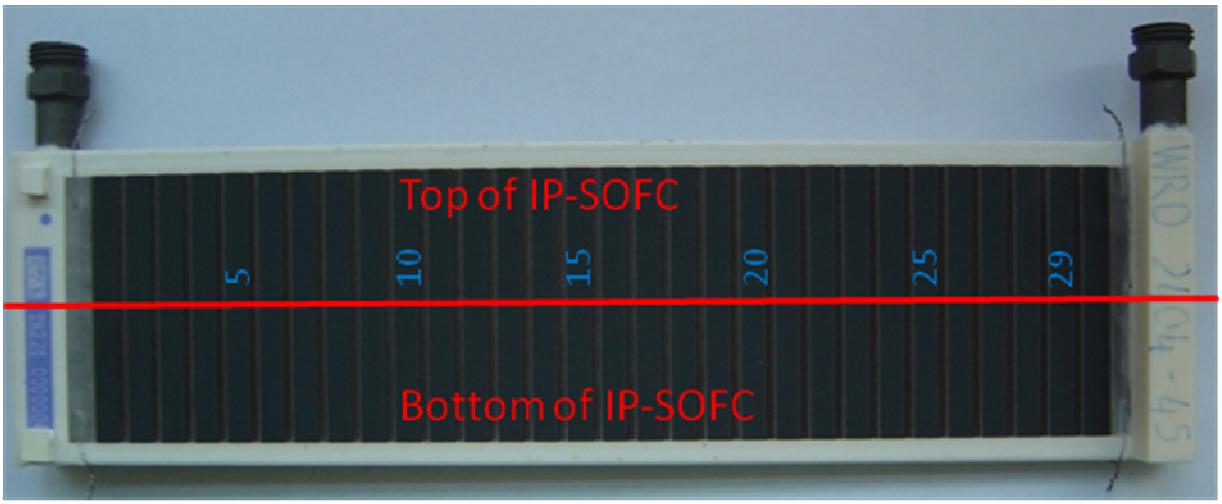

Figure 68: The top and bottom parts of the IP-SOFC, indicating the cells that were cut into half.

Figure 69: A small piece of cutting IP-SOFC.

The temperature-programmed oxidation (TPO) experiment was completed by packing the IP-SOFC pieces into a quartz glass tube reactor, which was then put into a furnace, as shown in Figure 70. Initially, IP-SOFC pieces were crushed into a powder to study the carbon deposition, but this powder did not give stable results because the nano particles of ceramic material caused a blockage preventing the

gases reaching the mass spectrometer. However, the IP-SOFC pieces were preferentially used in this analysis.

Figure 70: The IP-SOFC piece inside a quartz tube in furnace.

The TPO process was then used to study the formation of carbon deposition on the anode surface. TPO was applied through the application of a constant flow of helium (20 millilitres per minute) and oxygen (5 millilitres per minute) to the quartz tube, which contained the small pieces of the IP-SOFC tube. The furnace was then heated to 900 ^{o}C at a rate of 10 ^{o}C per minute. The outlet of the quartz tube was connected to an on-line mass spectrometer in order to evaluate the exhaust gases. The peak of CO_2 and CO measured on the mass spectrometer trace was then used to quantify the formation of carbon deposition. Using this process all of the carbon is oxidised to CO + CO_2, giving full detecting on the amount of carbon deposited on the surface.

7.1.1 Carbon amount calibration

CABOT carbon black was used to calibrate the amount of carbon that had been deposited. Varying amounts of carbon black was exposed to oxygen in order to form carbon dioxide and carbon monoxide. The variation in the amount of carbon black was then analysed through the use of the TPO technique, where known amounts of carbon black give a relationship between the area under the CO and CO_2 peaks (see Figure 18), and the amount of carbon oxidised. This experiment used eight samples of 0.9, 1.5, 2.3, 3.8, 5.4, 6.7, 9.8 and 11.2 mg of carbon black.

Figure 71 shows the relative concentration versus temperature for the produced spectra for the CO and CO_2 peaks for each sample.

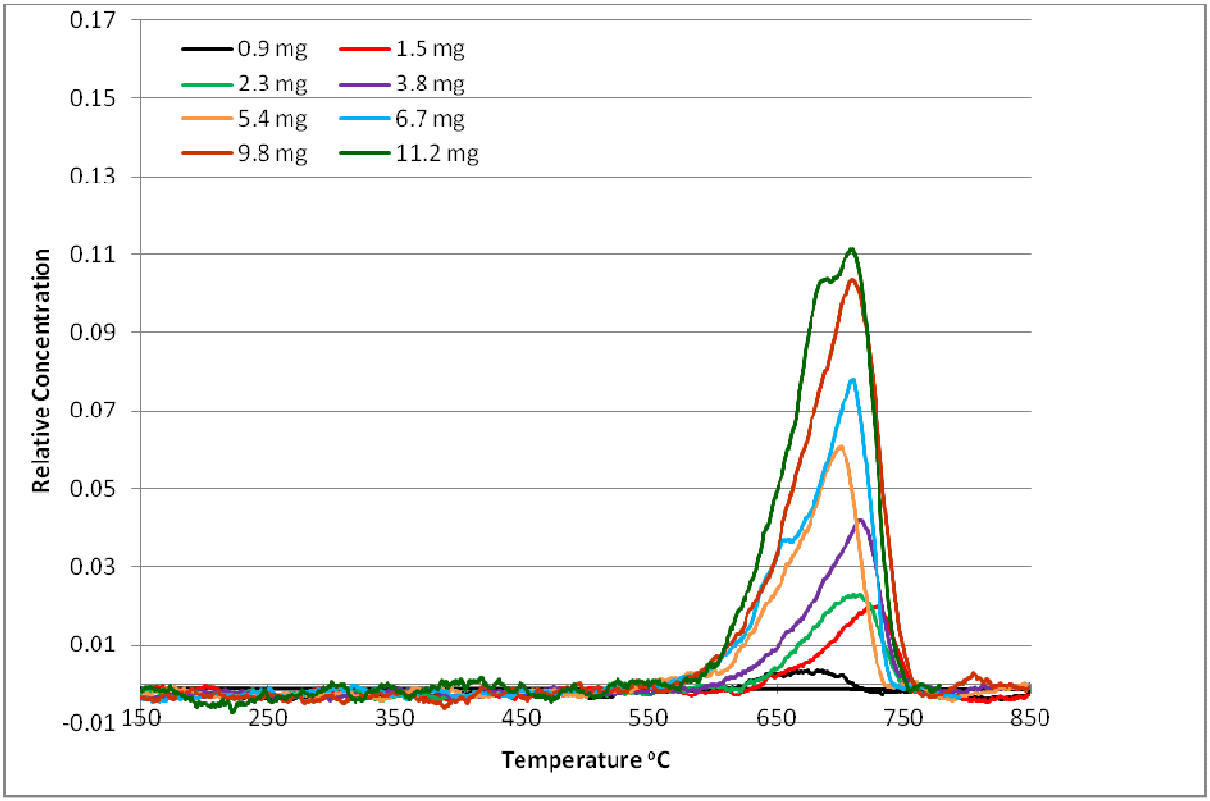

Figure 71: TPO spectra of CO plus CO_2 peaks of different amount of carbon black.

The area under the peaks for each sample was calculated by the trapezoidal rule, using the Sigmaplot programme macros, which are frequently used to calculate area under a curve, as shown in Table 12.

Table 12: The area under a curve for each sample of carbon black for CO plus CO_2 peaks.

Amount of Carbon (mg)	Area under the peak
0.9	0.3189
1.5	0.9988
2.3	1.3723
3.8	2.4786
5.4	3.784
6.7	5.1008
9.8	7.6196
11.2	8.6629

The level of deposition of carbon in IP-SOFC can be determined using the results of the calculations given in the second column of the area under the peaks for each sample. The plot of the weight of the eight samples of carbon black against the area under the curve is shown in Figure 72.

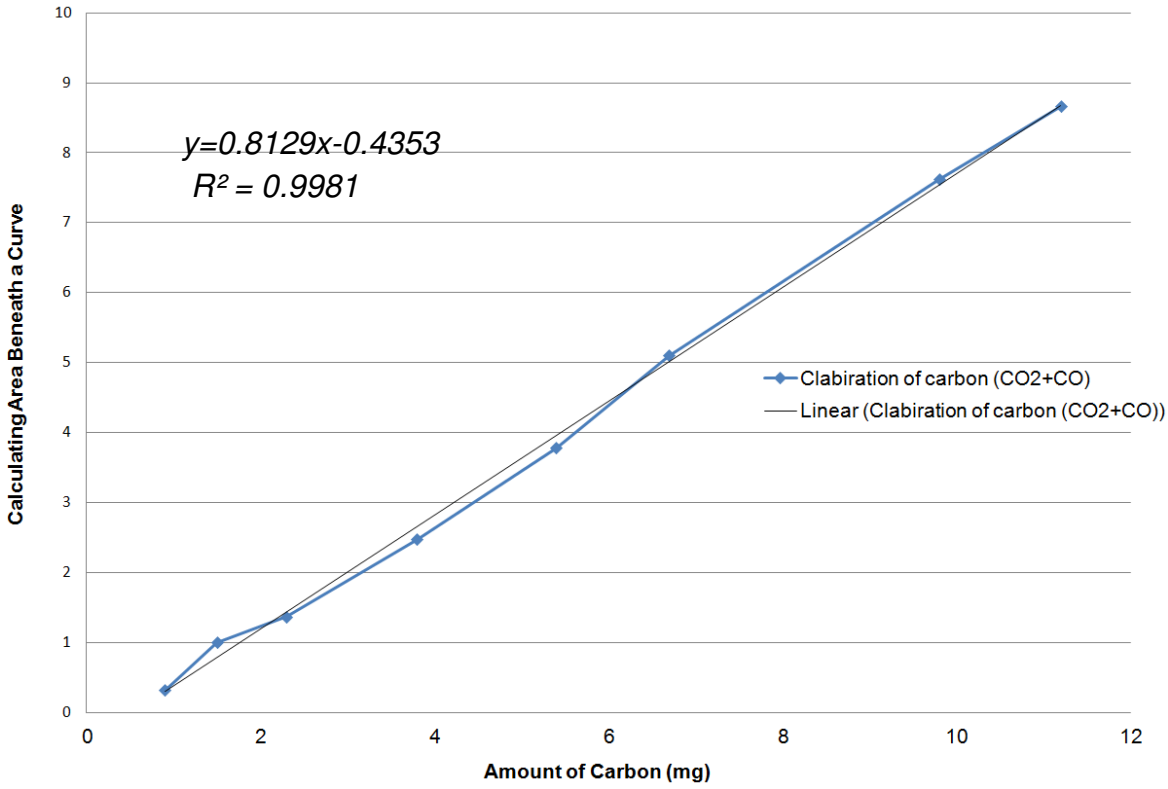

Figure 72: Equilibrium curve of carbon black.

The black line in Figure 72 shows the linear fit for equilibrium curve as given in Equation 7-4 :

y=0.8129x-0.4353 *R² = 0.9981* 7-4

Therefore, the amount of deposition carbon (*w*) can be calculated using the Equation 7-5 below:

$$w = \frac{y + 0.4353}{0.8129} \qquad 7\text{-}5$$

where, *y* is the area under the peak for the testing sample.

7.2 Analysis of carbon deposition in IP-SOFCs

The TPO technique was used to measure the carbon deposition on the IP-SOFC anode surface. The cells of the IP-SOFC (5, 10, 15, 20, 25, and 29) were cut into two pieces, which were then used to form the top and bottom part of the IP-SOFC, as shown in Figure 68.

This experiment avoided the beginning and the end of the IP-SOFC region for use in the calculation of the carbon deposition, as these regions had been damaged by exposure. These pieces were put inside the quartz tube and then exposed to oxygen with increasing temperatures ranging from 25 to 900 ^{o}C.

The peak of carbon dioxide emission produced by all of the cells was measured by the mass spectrometer. Figure 73 shows the TPO spectra of CO_2 plus CO for the top part of the IP-SOFC cells, while Figure 74 shows the TPO spectra of CO_2 plus CO produced for the bottom part of the IP-SOFC cells. In both diagrams, two peaks are evident at temperatures between 150 and 550 ^{o}C, and between 550 and 780 ^{o}C. These peaks represent the two types of carbon: amorphous carbon, peaking in the range of ~350 to ~430 ^{o}C and graphitic carbon, peaking between ~650 and ~750 ^{o}C. Through the use of these peaks it becomes possible to calculate the mass of carbon deposited on the particle surface in the anode of the IP-SOFC.

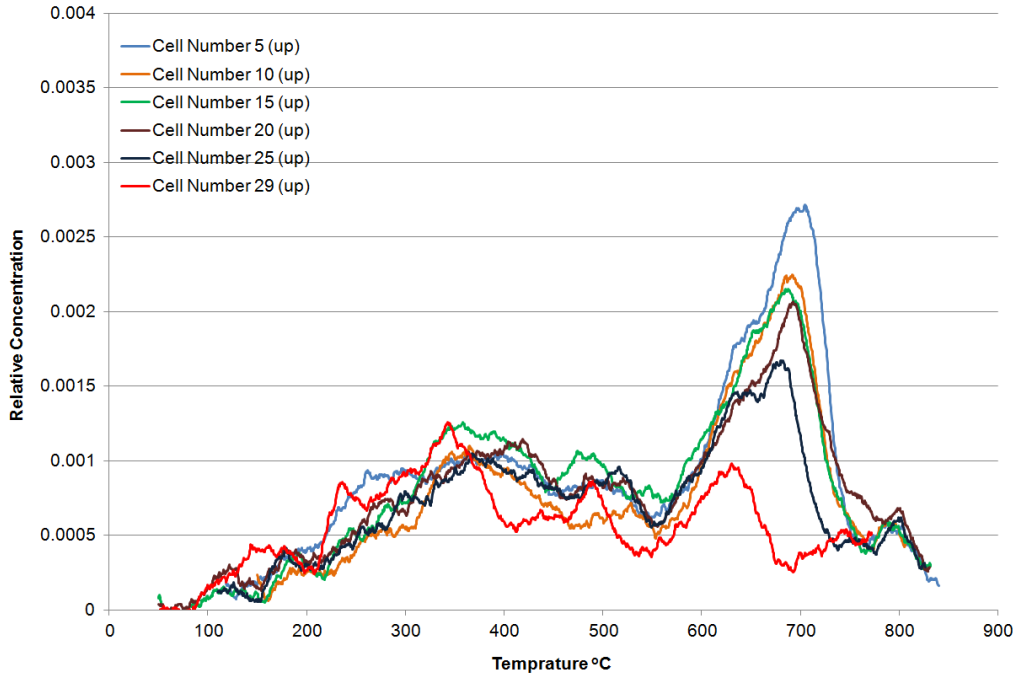

Figure 73: TPO spectra of CO_2 plus CO for top part of IP-SOFC cells.

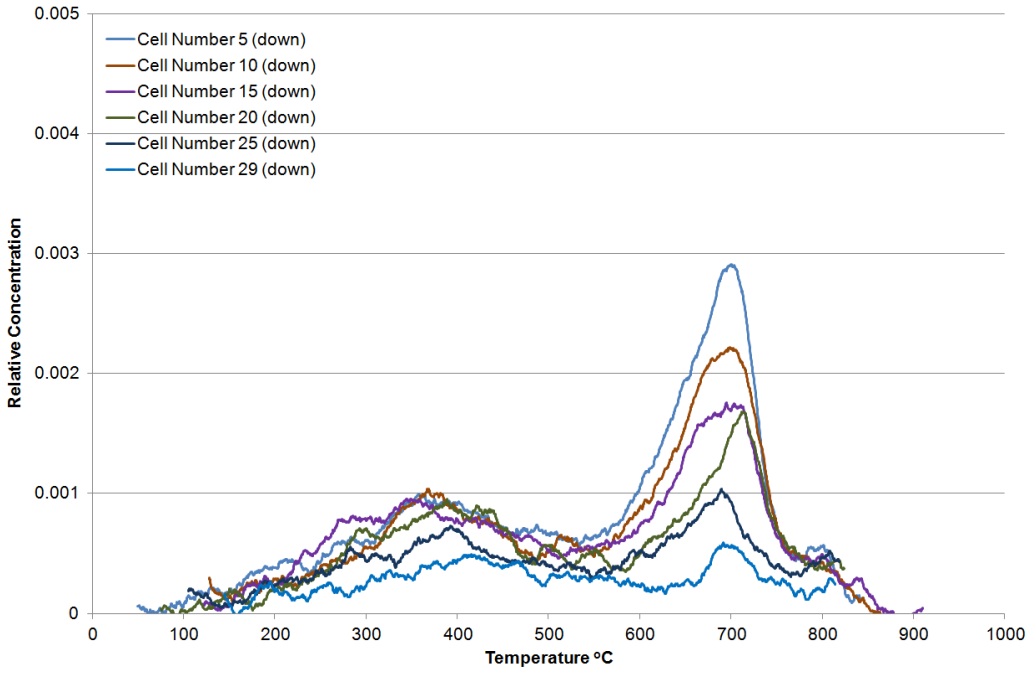

Figure 74: TPO spectra of CO_2 plus CO for bottom part of IP-SOFC cells.

The plots show two peaks: the lower temperature peak represents amorphous carbon, whereas the higher and sharper peak in the relative concentration is due to

graphitic carbon. These different of carbon type and their deposition vary depending on the reaction conditions, such as reaction temperature. While amorphous carbon oxidise at a low temperature around 300 ℃, graphitic oxidises at a higher temperature around 600 ℃. At an early stage of cell temperature operation, the amorphous carbons appeared to form and carbons were accumulated transformed into graphitic carbon due to the destroying of the integrated structure of the IP-SOFC.

The Trapezoidal rule was used to calculate the areas under the peaks between 550 ℃ and 780 ℃ in Figure 73 and Figure 74, the graphitic regions. The amount of carbon deposition was calculated by using Equation 7-5 for both top and bottom of IP-SOFC regions. Where the surface areas of each sample differ from each other, the amount of carbon deposition is divided by the area of sample in order to calculate the specific area carbon deposition, which facilitates comparison with other samples. Table 13 shows the carbon amount in the top region of the IP-SOFC (graphitic carbon, 550-780 ^{o}C), whereas Table 14 shows the amount of carbon in the bottom region of IP-SOFC (graphitic carbon, 550-780 ^{o}C).

Table 13: The amount of graphitic carbon in the top region of the IP-SOFC.

Cell number	Cell area (cm^2)	Area under curve	Amount of carbon (mg cm^{-2})
5	2.6	0.330	0.369
10	2.6	0.282	0.339
15	2.8	0.285	0.317
20	3	0.274	0.291
25	3	0.257	0.284
29	3	0.148	0.231

Table 14: The amount of graphitic carbon in the bottom region of the IP-SOFC.

Cell number	Cell area (cm^2)	Area under curve	Amount of carbon (mg cm^{-2})
5	3	0.343	0.319
10	3	0.288	0.297
15	2.8	0.205	0.281
20	2.9	0.188	0.265
25	2.7	0.134	0.259
29	2.6	0.062	0.235

Using the results of the calculations given in Table 13 and Table 14, the total amount of graphitic carbon deposition in cells 5, 10, 15, 20, 25 and 29 for the top and bottom region of IP-SOFC has been plotted in Figure 75.

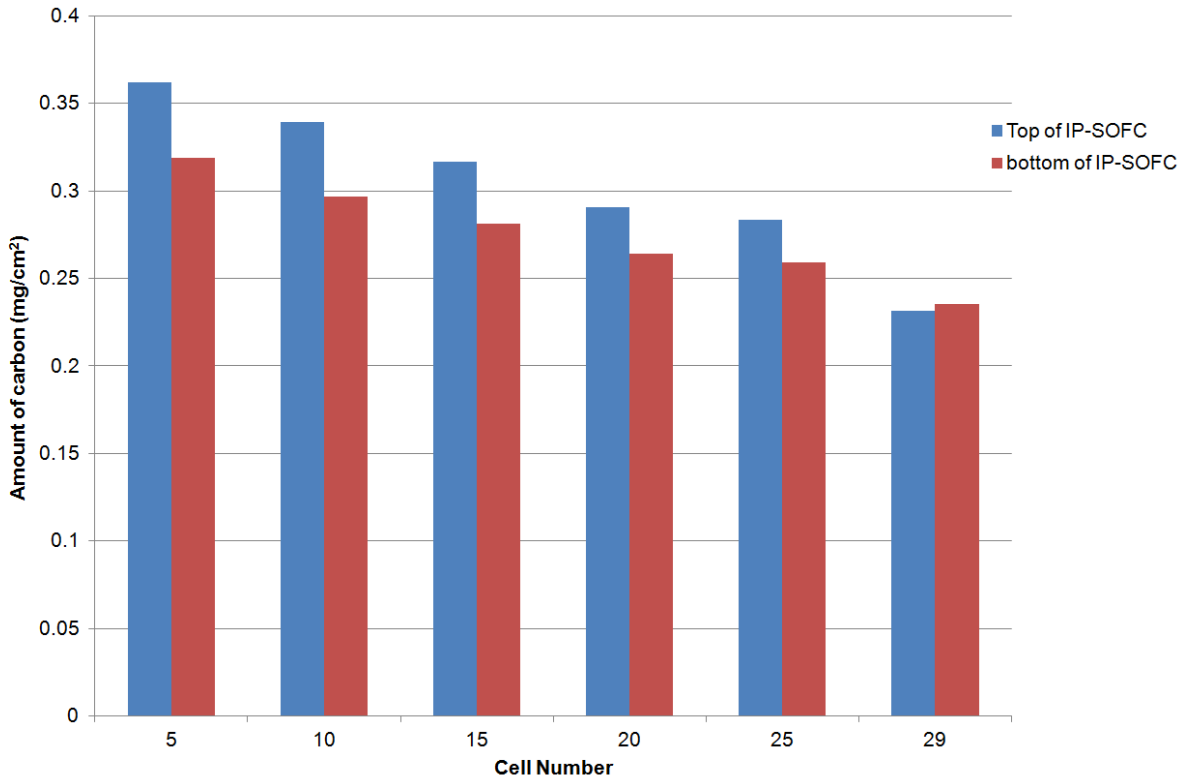

Figure 75: Histogram of the amount of graphitic carbon deposition in cells 5, 10, 15, 20, 25 and 29 in the top (blue) and bottom (red) regions of the IP-SOFC.

In Figure 75, in the top cells, the total amount of graphitic carbon was 369 µg per cm^2 at cell number 5. The level of carbon deposition gradually decreases to a total amount of carbon of 231 µg per cm^2 at the top of cell number 29. Similarly, in the bottom cells, the total amount of graphitic carbon decreases from 319 µg per cm^2 in cell 5 to 235 µg per cm^2 in cell 29. This decrease in the total of amount of graphitic carbon probably occurred because the methane was consumed along the gas channels in the IP-SOFC.

The second type of carbon is amorphous carbon, which oxidises at around 300 ℃, as shown in Figure 73 (top of the IP-SOFC) and Figure 74 (bottom of the IP-SOFC). From these diagrams, the area under curves (between 150 and 550 ^oC) was also calculated using the Trapezoidal rule in order to deduce the amount of amorphous carbon deposited on the anode surface of the IP-SOFC. Two types of carbon black from Cabot Company and other carbon black from Sigma-aldrich were tested to calibrate amorphous carbon peaks, but neither showed any peak between 150 and 550 ^oC. Where they peak between ~650 and ~750 ^oC, this denotes graphitic carbon. Table 15 shows the equivalent amount of total measure of amorphous carbon deposition in the top region of the IP-SOFC (amorphous carbon, 150-550 ^oC);

Table 16 shows the equivalent amount of total carbon deposition in the bottom region of the IP-SOFC (amorphous carbon, 150-550 ^oC). An equivalent amount was calculated by dividing the area under each curve with the piece area in cm^2 in order to facilitate comparison with other equivalent amount values.

Table 15: The equivalent amount of amorphous carbon in the top region of the IP-SOFC.

cell Number	cell Area (cm^2)	Area under curve	Equivalent amount of carbon
5	2.6	0.3158	0.1210
10	2.6	0.2956	0.1130
15	2.8	0.3013	0.107
20	3	0.2991	0.0990
25	3	0.2436	0.0812
29	3	0.2428	0.0783

Table 16: The equivalent amount of amorphous carbon in the bottom region of the IP-SOFC.

Cell number	Cell area (cm^2)	Area under curve	Equivalent amount of carbon
5	3	0.2611	0.0870
10	3	0.2292	0.0764
15	2.8	0.2129	0.0760
20	2.9	0.2093	0.0720
25	2.7	0.1693	0.0627
29	2.6	0.1167	0.0448

Using the data from calculations given in Table 15 and Table 16, the total equivalent amount of carbon deposition in cells 5, 10, 15, 20, 25 and 29 at top and bottom regions of the IP-SOFC was calculated for amorphous carbon, as shown in Figure **76**.

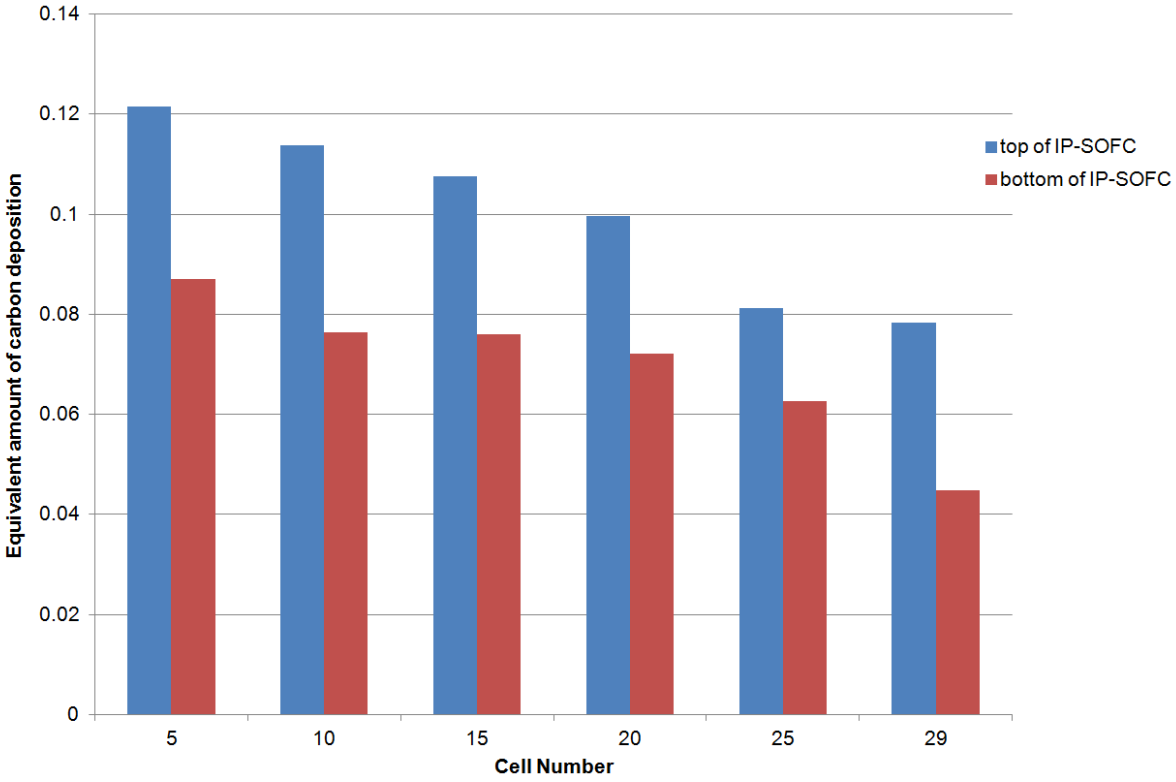

Figure 76: The equivalent amount of carbon deposition in cells, for amorphous carbon.

As can be seen in Figure 76, amorphous carbon deposition is concentrated in the beginning of the top cells of the IP-SOFC. The total equivalent amount of amorphous carbon was 0.121 per cm^2 at the top of cell number 5. A gradual decrease can be seen, where the total amount of amorphous carbon was 0.0783 per cm^2 at the top of cell number 29. At the same time, the total equivalent amount of amorphous carbon also fell at the bottom of the IP-SOFC, from 0.0870 per cm^2 at cell number 5 to 0.0448 per cm^2 at cell number 29. This is the lowest total equivalent amount of amorphous carbon, because the methane was consumed along the gas channels in the IP-SOFC.

A difference exists in the total amount of carbon deposition (amorphous and graphitic carbon) in the cells of the IP-SOFC, depending on many parameters, including

methane consumption and reaction temperature. It is clear in Figure 75 and Figure 76 that the largest amount of graphitic carbon deposition was found in the beginning of the cells of the IP-SOFC, probably as a result of exposure to the fuel mixture containing the highest levels of methane.

The second parameter affecting the total amount of carbon deposition is the reaction temperature. Air was pumped from the bottom of the IP-SOFC surrounding the cells, meaning that the temperature entering was less than the temperature of the furnace, as shown in Figure 77. This causes variation in the temperature of the IP-SOFC.

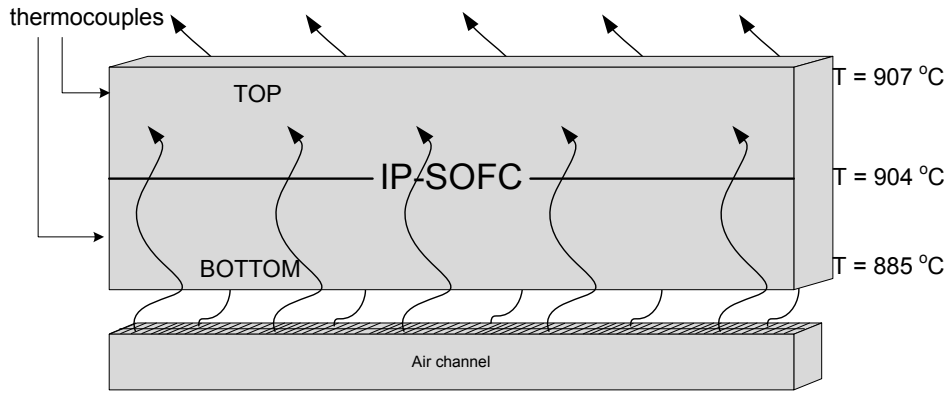

Figure 77: A schematic diagram for the distribution of temperature across the IP-SOFC.

The variation in the total amount of carbon deposited in relation to reaction temperature was significant. Carbon deposition rose sharply with increasing reaction temperature, due to methane decomposition, which becomes both kinetically and thermodynamically favourable with increasing reaction temperature. As illustrated in Figure 75 and Figure 76, the total carbon deposition in the bottom region was lower than the total carbon deposition in the top region for all the cells of the IP-SOFC. At the top of cell number 5, the total amount of graphitic carbon was 369 µg per cm^2,

when the average temperature was 907 ^{o}C, while at the bottom of the same cell, the total amount of graphitic carbon was 319 µg per cm^2 at the average temperature of 885 ^{o}C. Over the whole of the IP-SOFC the largest degree of carbon deposition was recorded in the top region that was exposed to the highest reaction temperature.

It should be noted that the expected degradation rate in the SOFC is low, at < 1% per 1000 hours operated in industrial application. This is a significant challenge as carbon deposition is a critical factor in the stability and rapid degradation in the performance in a SOFC, when operating with fuel that contains hydrocarbons such as methane [127]. In the previous chapter, the IP-SOFC was tested using a mixture fuel (hydrogen and methane) in order to investigate the effect of carbon deposition on the degradation behaviour of the IP-SOFC.

Figure 63 demonstrates that the performance of the IP-SOFC dropped and finally failed when a fuel mixture of 80% H_2 and 20% CH_4 was used. This decrease in performance of the IP-SOFC may have been caused by carbon deposition on the anode surface. The IP-SOFC features a porous ceramic support, which is a very hard layer and an anode layer, which contains nickel material that was printed above this layer. Ni is an excellent catalyst for carbon deposition reactions. In this case, the carbon forms between the porous ceramic support and the anode layer, resulting in the cells of the IP-SOFC layer cracking (as shown in Figure 78).

Figure 78: Cracking in the surface cells of the IP-SOFC

7.3 Conclusion

Carbon deposition is an important factor in IP-SOFC degradation, leading to direct structural damage of the IP-SOFC surface, which is composed of carbon between a porous ceramic support and an anode layer.

The IP-SOFC porous ceramic support was operated using a mixture fuel (hydrogen and methane) in order to study the degradation behaviour of the IP-SOFC caused by carbon deposition. The characterization results proved that two types carbon were formed on the anode surface: amorphous carbon, which oxidises between 150 ℃ and 550 ℃, and graphitic carbon, which oxidises between 550 ℃ and 780 ℃.

Reaction temperature and methane consumption seem to be the two main parameters increasing the total amount of carbon deposition on the anode surface of the IP-SOFC.

Chapter 8
Conclusions and Further work

8 Conclusions and future work

8.1 Conclusions

The aim of this thesis was to investigate some of the most critical problems affecting the performance of IP-SOFCs, in particular the microstructural changes and carbon deposition in SOFC operation. This was achieved by the characterisation of the performance of the IP-SOFC under different operating conditions, including a study into the effect of reduction techniques, load and thermal cycles to simulate extensive time-related damage over much shorter testing durations. A mixture fuel (hydrogen and methane) was used, but this mixture was found to be problematic when used as a fuel for the IP-SOFC, due to the resultant carbon deposition. The conclusions of this thesis are as follows:

1. In reduction processes for preparing the IP-SOFC for further testing, it has been shown that the flow rate of fuel in reduction processes onlys affect the performance of the IP-SOFC in a very small degree. High flow rate and low flow rate reduction techniques were studied. A small initial difference was observed at the beginning, but similar result was obtained for both techniques at more than 300 hours of operation.

2. In terms of the IP-SOFC operating under hydrogen, the study has shown that the causes of performance degradation include temperature gradient and increasing Ohmic resistance. This degradation is likely to occur due to operation of the IP-SOFC over a long time period, which affects the stability of materials, especially materials that are interconnected. The IP-SOFC ran steadily and gave a voltage degradation of 1.5% per 1000 hours of operation.

Durability testing of the IP-SOFC (over 6000 hours) has shown accelerated deterioration of IP-SOFC performance due to increasing Ohmic resistance and damage to the interconnected materials, which must also be taken into account. The Ohmic resistance was found to increase by approximately 1 Ω after 6000 hours of operation.

3. The shutdown and restarting during IP-SOFC testing causes serious problems due to the entry of oxygen to the anode surface. This exposure oxidizes Ni to NiO, resulting in the decreased performance of IP-SOFC at the subsequent restart.

4. The thermal cycling caused serious problems, with temperature change yielding particularly high levels of mechanical damage to the IP-SOFC materials during restarts or cooling. After several cycling stages, cracking (approximately 1cm) was observed on the IP-SOFC surface.

5. With methane contained fuel, the performance of the IP-SOFC has been shown to improve with methane contents in fuel mixtures (H_2 and CH_4). A higher open circuit voltage and the voltage under current applied were obtained in comparison to the IP-SOFCs operated with pure hydrogen. However, the long-term performance of the IP-SOFC was affected over time by this fuel mixture, resulting in a higher number of experiments where the voltage dropped. When using 95% H_2 and 5% CH_4, the IP-SOFC voltage degradation rate was 5% per 1000 hours. In contrast, when using 80% hydrogen and 20% methane, the voltage degradation rate was significantly higher, meaning that the IP-SOFC was completely dead.

6. The degradation behaviour observed in the IP-SOFC was mainly caused by the formation of solid carbon deposits inside the porous anode, which impede fuel diffusion and the electrochemical reaction on the anode side of the IP-SOFC.

7. Carbon deposition occurs on the anode surface. This begins with amorphous carbon being deposited, which oxidises between 150 ℃ and 550 ℃, after which graphitic carbon begins to build up, which oxidises between 550 ℃ and 780 ℃. Carbon deposition results in direct structural damage of the IP-SOFC surface because of the formation of carbon between the porous ceramic support and the anode layer. Two main parameters, reaction temperature and methane consumption, have been shown to increase the total amount of carbon deposition on the anode surface of the IP-SOFC.

8. The IP-SOFC consists of the anode, electrolyte, the cathode, and porous ceramic support. The active layers (anode, cathode, and electrolyte) are very thin, to reduce the Ohmic resistance of the IP-SOFC, meaning that the path of oxygen ions is very short in comparison with other types of solid oxide fuel cells. The IP-SOFC has a thick porous ceramic support, where fuel passes through the porous material to reach the anode layer. This requirement for a high flow rate to cross from the fuel channel in the IP-SOFC tube to the anode surface results in some fuel being wasted.

8.2 Further Work

Additional investigation and improvements are required in order to obtain a clearer understanding of the performance of the cells and their contribution to the use of alternative energy. This further work should include:

1. During the thermal cycling, the IP-SOFC was cracked, which caused serious degradation in the performance of the IP-SOFC. Due to the shortage of the IP-SOFCs, little detailed characterization has been done in this work. There should be further investigation into the behaviour of this IP-SOFC and its fracture mechanics.

2. The results of the experiments with the fuel show that the voltage output of the IP-SOFC is higher with the methane contained fuel than that with pure hydrogen. Further investigation is needed with long term period tests (between 1000 and 3000 hours), examining the effects of increasing the proportion of methane in the fuel mixture to over 20%.

3. The IP-SOFC performance has been successfully evaluated while operated with a fuel mixture of hydrogen and methane. Other large molecular hydrocarbons need to be tested under the cycling process and over longer time periods to compare their performance with the results of the hydrogen-methane fuel mixture.

4. While using the hydrogen and methane fuel mixture, carbon deposition was significantly increased due to the increased reaction temperature and the increased amount of methane in the fuel mixture. Therefore it is necessary to study the effect of carbon deposition on the performance of the IP-SOFC, with

changes in reaction temperature. The IP-SOFC needs to be tested with a different range of reaction temperatures between 700 ^{o}C and 900 ^{o}C, and the effect of the amount of methane in the fuel mixture also needs to be investigated further.

5. In this work, only single IP-SOFCs were tested. The testing of IP-SOFC stacks, with at least two IP-SOFCs connect together will provide valuable insight into other factors such as interconnection degradation and failure. Such an extensive study is required to investigate the effect of the cycling performance on the overall system efficiency.

6. Further development of test rig facilities for testing IP-SOFC is required. The current design allows air to enter though the outlet of IP-SOFC anode channel; this causes the oxidisation of the nickel material, which leads to decreasing performance of the IP-SOFC. A non-return valve must be installed at the anode exhaust.

9 References:

1. Almutairi, G., K. Kendall, and W. Bujalski, *Cycling durability studies of IP-SOFC.* International Journal of Low-Carbon Technologies, 2012. **7**(1): p. 63-68.
2. Almutairi, G., A. Dhir, and W. Bujalski, *Direct operation of IP-Solid Oxide Fuel Cell with hydrogen and methane fuel mixtures under current load cycle operating condition.* has been submitted to Fuel Cells, 2013.
3. Almutairi, G., A. Dhir, and W. Bujalski, *Analysing carbon deposition on Ni/YSZ anode of Integrated Planar Solid Oxide Fuel Cell (IP-SOFC)* has been submitted to Journal of Power Sources, 2013.
4. Steele, B.C.H., *Material science and engineering: The enabling technology for the commercialisation of fuel cell systems.* Journal of Materials Science, 2001. **36**(5): p. 1053-1068.
5. Williams, M.C., *Status and Promise of Fuel Cell Technology.* Fuel Cells, 2001. **1**(2): p. 87-91.
6. Hirschenhofer J, e.a., *Fuel Cell Hand Book fourth Edition*, P. Corp., Editor. 1998.
7. EG&G Services Parsons, I., Science Applications International Corporation, *TECHNOLOGY OVERVIEW*, in *Fuel Cell Handbook 5th*. 2000, U.S. Department of Energy, Office of Fossil Energy, National Energy Technology Laboratory: Morgantown, West Virginia. p. 5.
8. Gunter, R., *Fuel Cell Technologies for Hydrogen*, in *E.V.A.* 2002, The Austrian Energy Agency: Lisbon.
9. Tu, H. and U. Stimming, *Advances, aging mechanisms and lifetime in solid-oxide fuel cells.* Journal of Power Sources, 2004. **127**(1-2): p. 284-293.
10. Assabumrungrat, S., et al., *Thermodynamic analysis of carbon formation in a solid oxide fuel cell with a direct internal reformer fuelled by methanol.* Journal of Power Sources, 2005. **139**(1-2): p. 55-60.
11. Moon, D.J. and J.W. Ryu, *Electrocatalytic reforming of carbon dioxide by methane in SOFC system.* Catalysis Today, 2003. **87**(1-4): p. 255-264.
12. Richard, F., *A novel configuration for direct internal reforming stacks.* Journal of Power Sources, 1998. **71**(1-2): p. 281-287.
13. Winkler, W. and H. Lorenz, *The design of stationary and mobile solid oxide fuel cell–gas turbine systems.* Journal of Power Sources, 2002. **105**(2): p. 222-227.
14. Yokokawa, H., et al., *Fundamental mechanisms limiting solid oxide fuel cell durability.* Journal of Power Sources, 2008. **182**(2): p. 400-412.
15. T. Ishihara, N.S.a.O.Y., *Chapter 4: Electrolyte*, in *High Temperature Solid Oxide Fuel Cells: Fundamentals, Design and Applications*, S. Kendall Kevin, C. Subhash. , Editor. 2003, Oxford: Elsevier Ltd. p. 82.
16. Brandon, N.P. and D.J. Brett, *Engineering porous materials for fuel cell applications.* Philosophical Transactions of the Royal Society A: Mathematical, Physical and Engineering Sciences, 2006. **364**(1838): p. 147-159.
17. Gorte, R.J. and J.M. Vohs, *Novel SOFC anodes for the direct electrochemical oxidation of hydrocarbons.* Journal of Catalysis, 2011. **216**(1-2): p. 477-486.
18. Sun, C. and U. Stimming, *Recent anode advances in solid oxide fuel cells.* Journal of Power Sources, 2007. **171**(2): p. 247-260.
19. Yamamoto, O., *Solid oxide fuel cells: fundamental aspects and prospects.* Electrochimica Acta 2000. **45**(15-16): p. 2423-2435.
20. Veyo, S.E., Shockling, S. A., Dederer, J. E., Gillet, J. E. & Lundberg, W. L. , *Tubular Solid Oxide Fuel Cell/Gas Turbine Hybrid Cycle Power Systems: Status.* Journal of Engineering for Gas Turbines and Power 2000. **124**(4): p. 845-849.

21. Singhal, C.S., *Advances in solid fuel cell technology.* Solid State Ionics 2000. **135**(1-4): p. 305-313.
22. Kendall, K., Minh, N.Q., Singhal, S.C.,, *Chapter 8:Cell Stack and Designs*, in *High Temperature Solid Oxide Fuel Cells: Fundamentals, Design and Applications*, S. Kendall Kevin, C. Subhash. , Editor. 2003, Oxford: Elsevier Ltd. p. 197-228.
23. Minh, N.Q. and T. Takahashi, *Chapter 9 - Stack design and fabrication*, in *Science and Technology of Ceramic Fuel Cells*. 1995, Elsevier Science Ltd: Oxford. p. 233-306.
24. Ehsani Mehrdad, G.Y., Gay, E. Sebastien & Emadi Ali., *Modern Electric, Hybrid Electric, and Fuel Cell Vehicles: Fundamentals, Theory, and Design*. 2005, Boca Raton, Florida: CRC Press.
25. Kendall Kevin, M., Q. Nguyen & Singhal, C. Subhash. , *High Temperature Solid Oxide Fuel Cells: Fundamentals, Design and Applications*. Cell Stack and Designs. 2003: Oxford: Elsevier Ltd. 197-228.
26. Kendall Kevin, S., C. Subhash. , *Chapter 1:Introduction to SOFCs*, in *High Temperature Solid Oxide Fuel Cells: Fundamentals, Design and Applications*, S. Kendall Kevin, C. Subhash. , Editor. 2003, Oxford: Elsevier Ltd. p. 197-228.
27. Singhal, C.S., *Solid oxide fuel cells for stationary, mobile, and military applications.* Solid State Ionics, 2000. **152-153**: p. 405-410. .
28. Dhir, A. and K. Kendall, *Microtubular SOFC anode optimisation for direct use on methane.* Journal of Power Sources, 2008. **181**(2): p. 297-303.
29. Gardner, F.J., et al., *SOFC technology development at Rolls-Royce.* Journal of Power Sources, 2000. **86**(1-2): p. 122-129.
30. Minh, N.Q., *Ceramic Fuel Cells.* Journal of the American Ceramic Society, 1993. **76**(3): p. 563-588.
31. Alston, T., et al., *A 1000-cell SOFC reactor for domestic cogeneration.* Journal of Power Sources, 1998. **71**(1-2): p. 271-274.
32. Keegan C. Wincewicz and Joyce S. Cooper, *Taxonomies of SOFC material and manufacturing alternatives.* Journal of Power Sources, 2005. **140**(2): p. 280-296.
33. Gellings, P.J. and H.J.M. Bouwmeester, *Ion and mixed conducting oxides as catalysts.* Catalysis Today, 1992. **12**(1): p. 1-101.
34. Badwal, S.P.S. and K. Foger, *Materials for solid oxide fuel cells.* Material Forum, 1997. **21**: p. 187-224.
35. Ivers-Tiffée, E., A. Weber, and D. Herbstritt, *Materials and technologies for SOFC-components.* Journal of the European Ceramic Society, 2001. **21**(10-11): p. 1805-1811.
36. S.P.S, B., *Zirconia-based solid electrolytes: microstructure, stability and ionic conductivity.* Solid State Ionics, 1992. **52**(1-3): p. 23-32.
37. Badwal, S.P.S., F.T. Ciacchi, and D. Milosevic, *Scandia–zirconia electrolytes for intermediate temperature solid oxide fuel cell operation.* Solid State Ionics, 2000. **136-137**(0): p. 91-99.
38. H. Tianmin, L.Z., P. Li, H. Xiqiang, L. Zhiguo and S. Weihui, *Electrical properties of thin-walled 8 mol% yttria-stabilized zirconia electrolyte tubes prepared by an improved slip casting method.* Journal of Alloys and Compounds, 2002. **333**(1-2): p. 231-236.
39. Ralph, J.M., J.A. Kilner, and B.C.H. Steele, *Improving Gd-Doped Ceria Electrolytes for Low Temperature Solid Oxide Fuel Cells.* MRS Online Proceedings Library, 1999. **575**: p. null-null.
40. Ishihara, T., et al., *Transition Metal Doped LaGaO3 Perovskite Fast Oxide Ion Conductor and Intermediate Temperature Solid Oxide Fuel Cell.* MRS Online Proceedings Library, 1999. **575**: p. null-null.
41. Jeffrey W, F., *Electrolytes for solid oxide fuel cells.* Journal of Power Sources, 2006. **162**(1): p. 30-40.
42. Jacobson, A.J., *Materials for Solid Oxide Fuel Cells.* Chemistry of Materials, 2009. **22**(3): p. 660-674.

43. Kharton, V.V., F.M.B. Marques, and A. Atkinson, *Transport properties of solid oxide electrolyte ceramics: a brief review.* Solid State Ionics, 2004. **174**(1-4): p. 135-149.
44. Schwarz, K., *Materials design of solid electrolytes.* Proceedings of the National Academy of Sciences of the United States of America, 2006. **103**(10): p. 3497.
45. Seo, D.J., et al., *Synthesis and properties of Ce1−xGdxO2−x/2 solid solution prepared by flame spray pyrolysis.* Materials Research Bulletin, 2006. **41**(2): p. 359-366.
46. Joshi, A.V., et al., *Solid Electrolyte Materials, Devices, and Applications.* Journal of Electroceramics, 2004. **13**(1): p. 619-625.
47. Weber, A. and E. Ivers-Tiffée, *Materials and concepts for solid oxide fuel cells (SOFCs) in stationary and mobile applications.* Journal of Power Sources, 2004. **127**(1-2): p. 273-283.
48. Maguire, E., et al., *Cathode materials for intermediate temperature SOFCs.* Solid State Ionics, 2000. **127**(3-4): p. 329-335.
49. Jiang, S., *Development of lanthanum strontium manganite perovskite cathode materials of solid oxide fuel cells: a review.* Journal of Materials Science, 2008. **43**(21): p. 6799-6833.
50. Hart, N.T., et al., *Functionally graded composite cathodes for solid oxide fuel cells.* Journal of Power Sources, 2002. **106**(1-2): p. 42-50.
51. Tsai, T. and S.A. Barnett, *Effect of LSM-YSZ cathode on thin-electrolyte solid oxide fuel cell performance.* Solid State Ionics, 1997. **93**(3-4): p. 207-217.
52. Yoon, S.P., et al., *Performance of anode-supported solid oxide fuel cell with La0.85Sr0.15MnO3 cathode modified by sol–gel coating technique.* Journal of Power Sources, 2002. **106**(1-2): p. 160-166.
53. Petrov, A.N., et al., *Crystal structure, electrical and magnetic properties of La1 − xSrxCoO3 − y.* Solid State Ionics, 1995. **80**(3-4): p. 189-199.
54. Tai, L.W., et al., *Structure and electrical properties of La1 − xSrxCo1 − yFeyO3. Part 2. The system La1 − xSrxCo0.2Fe0.8O3.* Solid State Ionics, 1995. **76**(3-4): p. 273-283.
55. Tu, H.Y., et al., *Ln0.4Sr0.6Co0.8Fe0.2O3−δ (Ln=La, Pr, Nd, Sm, Gd) for the electrode in solid oxide fuel cells.* Solid State Ionics, 1999. **117**(3-4): p. 277-281.
56. Chen, J., et al., *Palladium and ceria infiltrated La0.8Sr0.2Co0.5Fe0.5O3−δ cathodes of solid oxide fuel cells.* Journal of Power Sources, 2009. **194**(1): p. 275-280.
57. Nie, L., et al., *La0.6Sr0.4Co0.2Fe0.8O3−δ cathodes infiltrated with samarium-doped cerium oxide for solid oxide fuel cells.* Journal of Power Sources, 2010. **195**(15): p. 4704-4708.
58. Bastidas, D.M., S. Tao, and J.T.S. Irvine, *A symmetrical solid oxide fuel cell demonstrating redox stable perovskite electrodes.* Journal of Materials Chemistry, 2006. **16**(17): p. 1603-1605.
59. Zhen, Y.D., et al., *La(Ni,Fe)O3 as a cathode material with high tolerance to chromium poisoning for solid oxide fuel cells.* Journal of Power Sources, 2007. **170**(1): p. 61-66.
60. Sahibzada, M., et al., *Pd-promoted La0.6Sr0.4Co0.2Fe0.8O3 cathodes.* Solid State Ionics, 1998. **113-115**(0): p. 285-290.
61. Xia, C. and M. Liu, *Novel Cathodes for Low-Temperature Solid Oxide Fuel Cells.* Advanced Materials, 2002. **14**(7): p. 521-523.
62. Haanappel, V.A.C., et al., *The influence of noble-metal-containing cathodes on the electrochemical performance of anode-supported SOFCs.* Journal of Power Sources, 2004. **130**(1-2): p. 119-128.
63. Minh, N.Q. and T. Takahashi, *Chapter 6 - Anode*, in *Science and Technology of Ceramic Fuel Cells*. 1995, Elsevier Science Ltd: Oxford. p. 147-164.
64. Augustin, M., *Chapter 6 - Anodes*, in *High Temperature and Solid Oxide Fuel Cells*, C.S. Subhash and K. Kevin, Editors. 2003, Elsevier Science: Amsterdam. p. 149-171.
65. Goodenough, J.B. and Y.-H. Huang, *Alternative anode materials for solid oxide fuel cells.* Journal of Power Sources, 2007. **173**(1): p. 1-10.

66. Tao, S. and J.T. Irvine, *Discovery and characterization of novel oxide anodes for solid oxide fuel cells.* Chem Rec, 2004. **4**(2): p. 83-95.
67. Vielstich, W.L., A. Gasteiger H., *Fundamental and Technology and Applications*, in *Handbook Fuel Cells*. 2003, John Wiley & son Ltd: West Sussex, UK. p. 439.
68. Zhe Cheng, J.-H.W., and Meilin Liu, *Chapter 2 : Anode*, in *Solid Oxide Fuel Cells: Materials Properties and Performance*, R.H. Jeffrey W. Fergus, Xianguo Li, David P. Wilkinson, Jiujun Zhang, Editor. 2009, CRC Press. p. 74-125.
69. Dees, D.W., et al., *Conductivity of Porous Ni/ZrO[sub 2]-Y[sub 2]O[sub 3] Cermets.* Journal of The Electrochemical Society, 1987. **134**(9): p. 2141-2146.
70. B.C.H, S., *Appraisal of Ce1−yGdyO2−y/2 electrolytes for IT-SOFC operation at 500°C.* Solid State Ionics, 2000. **129**(1-4): p. 95-110.
71. Murray, E.P., T. Tsai, and S.A. Barnett, *A direct-methane fuel cell with a ceria-based anode.* Nature, 1999. **400**(6745): p. 649-651.
72. McIntosh, S., J.M. Vohs, and R.J. Gorte, *Role of Hydrocarbon Deposits in the Enhanced Performance of Direct-Oxidation SOFCs.* Journal of The Electrochemical Society, 2003. **150**(4): p. A470-A476.
73. Kim, H., et al., *Cu-Ni Cermet Anodes for Direct Oxidation of Methane in Solid-Oxide Fuel Cells.* Journal of The Electrochemical Society, 2002. **149**(3): p. A247-A250.
74. Lashtabeg, A. and S.J. Skinner, *Solid oxide fuel cells-a challenge for materials chemists?* Journal of Materials Chemistry, 2006. **16**(31): p. 3161-3170.
75. Wang, C., et al., *Fabrication and Performance of Thin-Film YSZ Solid Oxide Fuel Cells.* Journal of The Electrochemical Society, 2001. **148**(8): p. A864-A868.
76. Sauvet, A.L. and J.T.S. Irvine, *Catalytic activity for steam methane reforming and physical characterisation of La1−xSrxCr1−yNiyO3−δ.* Solid State Ionics, 2004. **167**(1-2): p. 1-8.
77. Weston, M. and I.S. Metcalfe, *La0.6Sr0.4Co0.2Fe0.8O3 as an anode for direct methane activation in SOFCS.* Solid State Ionics, 1998. **113-115**(0): p. 247-251.
78. Vernoux, P., et al., *Alternative anode material for gradual methane reforming in solid oxide fuel cells.* Solid State Ionics, 2000. **135**(1-4): p. 425-431.
79. Hui, S. and A. Petric, *Evaluation of yttrium-doped SrTiO3 as an anode for solid oxide fuel cells.* Journal of the European Ceramic Society, 2002. **22**(9-10): p. 1673-1681.
80. Klemenso, T., et al., *The Mechanism Behind Redox Instability of Anodes in High-Temperature SOFCs.* Journal of The Electrochemical Society, 2005. **152**(11): p. A2186-A2192.
81. Klemensø, T. and M. Mogensen, *Ni–YSZ Solid Oxide Fuel Cell Anode Behavior Upon Redox Cycling Based on Electrical Characterization.* Journal of the American Ceramic Society, 2007. **90**(11): p. 3582-3588.
82. Fergus, Z.G.Y.a.J.W., *Chapter 4 : Interconnects*, in *Solid Oxide Fuel Cells: Materials Properties and Performance*, R.H. Jeffrey W. Fergus, Xianguo Li, David P. Wilkinson, Jiujun Zhang, Editor. 2009, CRC Press. p. 179-205.
83. Jeffrey W, F., *Lanthanum chromite-based materials for solid oxide fuel cell interconnects.* Solid State Ionics, 2004. **171**(1-2): p. 1-15.
84. Minh, N.Q. and T. Takahashi, *Chapter 7 - Interconnect*, in *Science and Technology of Ceramic Fuel Cells*. 1995, Elsevier Science Ltd: Oxford. p. 165-198.
85. Zhu, W.Z. and S.C. Deevi, *Development of interconnect materials for solid oxide fuel cells.* Materials Science and Engineering: A, 2003. **348**(1-2): p. 227-243.
86. Sehlin, S.R., H.U. Anderson, and D.M. Sparlin, *Electrical characterization of the (La,Ca)(Cr,Co)O3 system.* Solid State Ionics, 1995. **78**(3-4): p. 235-243.
87. Zhu, W.Z. and S.C. Deevi, *Opportunity of metallic interconnects for solid oxide fuel cells: a status on contact resistance.* Materials Research Bulletin, 2003. **38**(6): p. 957-972.
88. Yang, Z., J. Stevenson, and P. singh, *Solid Oxide Fuel Cells.* Adv. Mater. Process, 2003. **161**(6): p. 34-37.

89. Kofstad, P. *High temperature oxidation of chromium and chromium-forming alloys*. in *Proceedings of Second European Solid Oxide Fuel Cell Forum*. 1996. Oslo, Norway.
90. Brylewski, T., et al., *Application of Fe–16Cr ferritic alloy to interconnector for a solid oxide fuel cell.* Solid State Ionics, 2001. **143**(2): p. 131-150.
91. Linderoth, S., et al., *Investigations of metallic alloys for use as interconnects in solid oxide fuel cell stacks.* Journal of Materials Science, 1996. **31**(19): p. 5077-5082.
92. S.P.S, B., *Stability of solid oxide fuel cell components.* Solid State Ionics, 2001. **143**(1): p. 39-46.
93. Kim, J.-H., R.-H. Song, and S.-H. Hyun, *Effect of slurry-coated LaSrMnO3 on the electrical property of Fe–Cr alloy for metallic interconnect of SOFC.* Solid State Ionics, 2004. **174**(1-4): p. 185-191.
94. P.A. Lessing, J.H., and S. Elangovan, *Chapter 5 : sealant*, in *Solid Oxide Fuel Cells: Materials Properties and Performance*, R.H. Jeffrey W. Fergus, Xianguo Li, David P. Wilkinson, Jiujun Zhang, Editor. 2009, CRC Press. p. 179-205.
95. Cimenti, M. and J. Hill, *Direct Utilization of Liquid Fuels in SOFC for Portable Applications: Challenges for the Selection of Alternative Anodes.* Energies, 2009. **2**(2): p. 377-410.
96. He, H. and J.M. Hill, *Carbon deposition on Ni/YSZ composites exposed to humidified methane.* Applied Catalysis A: General, 2007. **317**(2): p. 284-292.
97. Nikooyeh, K., et al., *Effect of hydrogen on carbon formation on Ni/YSZ composites exposed to methane.* Applied Catalysis A: General, 2008. **347**(1): p. 106-111.
98. Alzate-Restrepo, V. and J.M. Hill, *Effect of anodic polarization on carbon deposition on Ni/YSZ anodes exposed to methane.* Applied Catalysis A: General, 2008. **342**(1-2): p. 49-55.
99. J.R, R.-N., *Production of synthesis gas.* Catalysis Today, 1993. **18**(4): p. 305-324.
100. Bharadwaj, S.S. and L.D. Schmidt, *Catalytic partial oxidation of natural gas to syngas.* Fuel Processing Technology, 1995. **42**(2-3): p. 109-127.
101. Naidja, A., et al., *Cool flame partial oxidation and its role in combustion and reforming of fuels for fuel cell systems.* Progress in Energy and Combustion Science, 2003. **29**(2): p. 155-191.
102. Vernon, P.D.F., et al., *Partial oxidation of methane to synthesis gas, and carbon dioxide as an oxidising agent for methane conversion.* Catalysis Today, 1992. **13**(2-3): p. 417-426.
103. Swaan, H.M., et al., *Deactivation of supported nickel catalysts during the reforming of methane by carbon dioxide.* Catalysis Today, 1994. **21**(2-3): p. 571-578.
104. Jiang, Y. and A.V. Virkar, *A High Performance, Anode-Supported Solid Oxide Fuel Cell Operating on Direct Alcohol.* Journal of The Electrochemical Society, 2001. **148**(7): p. A706-A709.
105. McIntosh, S. and R.J. Gorte, *Direct Hydrocarbon Solid Oxide Fuel Cells.* Chemical Reviews, 2004. **104**(10): p. 4845-4866.
106. Brett, D.J.L., et al., *Methanol as a direct fuel in intermediate temperature (500–) solid oxide fuel cells with copper based anodes.* Chemical Engineering Science, 2005. **60**(21): p. 5649-5662.
107. Liu, M., et al., *Direct liquid methanol-fueled solid oxide fuel cell.* Journal of Power Sources, 2008. **185**(1): p. 188-192.
108. Dicks, J.L.a.A., *Fuel Cell Systems Explained*. 2002, England: John Wiley & Sons Ltd.
109. Liu, Y.L., et al., *Studies of Interfacial Microstructure in SOFCs by Transmission Electron microscopy*, in *Proceedings of the 26th Risø International Symposium on Materials Science: Solid State Electrochemistry*, e.a. S. Linderoth, Editor. 2005: Risø National Laboratory, Roskilde, Denmark. p. pp. 273-278.
110. S.P, J., *Issues on development of (La,Sr)MnO3 cathode for solid oxide fuel cells.* Journal of Power Sources, 2003. **124**(2): p. 390-402.

111. Kuo, J.H., H.U. Anderson, and D.M. Sparlin, *Oxidation-reduction behavior of undoped and Sr-doped LaMnO3: Defect structure, electrical conductivity, and thermoelectric power.* Journal of Solid State Chemistry, 1990. **87**(1): p. 55-63.
112. Jiang, S.P., *Sintering behavior of Ni/Y₂O₃-ZrO₂cermet electrodes of solid oxide fuel cells.* Journal of Materials Science, 2003. **38**(18): p. 3775-3782.
113. Faes, A., et al., *Nickel–Zirconia Anode Degradation and Triple Phase Boundary Quantification from Microstructural Analysis.* Fuel Cells, 2009. **9**(6): p. 841-851.
114. Tu, H. and U. Stimming, *Advances, aging mechanisms and lifetime in solid-oxide fuel cells.* Journal of Power Sources, 2004. **127**(1–2): p. 284-293.
115. Jiang, S.P. and W. Wang, *Sintering and grain growth of (La,Sr)MnO3 electrodes of solid oxide fuel cells under polarization.* Solid State Ionics, 2005. **176**(13–14): p. 1185-1191.
116. Hagen, A., et al., *Degradation of Anode Supported SOFCs as a Function of Temperature and Current Load.* Journal of The Electrochemical Society, 2006. **153**(6): p. A1165-A1171.
117. Tanasini, P., et al., *Experimental and Theoretical Investigation of Degradation Mechanisms by Particle Coarsening in SOFC Electrodes.* Fuel Cells, 2009. **9**(5): p. 740-752.
118. Dhir, A., *Improved MicrotubularSolid Oxide Fuel Cells*, in *School of Chemical Engineering*. 2008, University of Birmingham. p. 191.
119. Finnerty, C.M., et al., *Carbon formation on and deactivation of nickel-based/zirconia anodes in solid oxide fuel cells running on methane.* Catalysis Today, 1998. **46**(2-3): p. 137-145.
120. Mallon, C. and K. Kendall, *Sensitivity of nickel cermet anodes to reduction conditions.* Journal of Power Sources, 2005. **145**(2): p. 154-160.
121. R.M, O., *Internal reforming in solid oxide fuel cells*, in *Studies in Surface Science and Catalysis*, G.F. Froment and K.C. Waugh, Editors. 1999, Elsevier. p. 35-46.
122. Lee, T.J., *Characterisation of Anode Support Microtubular SOFC Process on Pure Methane Reduction and Operation*, in *Chemical Engineering*. 2009, University of Birmingham: Birmingham.
123. Takeguchi, T., et al., *Effect of precious metal addition to Ni-YSZ cermet on reforming of CH4 and electrochemical activity as SOFC anode.* Catalysis Today, 2003. **84**(3-4): p. 217-222.
124. Iida, T., et al., *Internal Reforming of SOFCs.* Journal of The Electrochemical Society, 2007. **154**(2): p. B234-B241.
125. Sumi, H., et al., *Comparison Between Internal Steam and CO[sub 2] Reforming of Methane for Ni-YSZ and Ni-ScSZ SOFC Anodes.* Journal of The Electrochemical Society, 2010. **157**(8): p. B1118-B1125.
126. Sumi, H., et al., *Performance of nickel–scandia-stabilized zirconia cermet anodes for SOFCs in 3% H2O–CH4.* Solid State Ionics, 2004. **174**(1-4): p. 151-156.
127. Chen, T., et al., *Evaluation of carbon deposition behavior on the nickel/yttrium-stabilized zirconia anode-supported fuel cell fueled with simulated syngas.* Journal of Power Sources, 2011. **196**(5): p. 2461-2468.
128. Lin, Y., et al., *Direct operation of solid oxide fuel cells with methane fuel.* Solid State Ionics, 2005. **176**(23–24): p. 1827-1835.
129. Liu, J. and S.A. Barnett, *Operation of anode-supported solid oxide fuel cells on methane and natural gas.* Solid State Ionics, 2003. **158**(1–2): p. 11-16.
130. Gunji, A., et al., *Carbon deposition behaviour on Ni–ScSZ anodes for internal reforming solid oxide fuel cells.* Journal of Power Sources, 2004. **131**(1–2): p. 285-288.
131. Vernoux, P., et al., *Alternative anode material for gradual methane reforming in solid oxide fuel cells.* Solid State Ionics, 2000. **135**(1–4): p. 425-431.
132. Park, S., J.M. Vohs, and R.J. Gorte, *Direct oxidation of hydrocarbons in a solid-oxide fuel cell.* Nature, 2000. **404**(6775): p. 265-267.

133. Singh, D., et al., *Carbon deposition in an SOFC fueled by tar-laden biomass gas: a thermodynamic analysis.* Journal of Power Sources, 2005. **142**(1–2): p. 194-199.
134. Laycock, C.J., J.Z. Staniforth, and R.M. Ormerod, *Biogas as a fuel for solid oxide fuel cells and synthesis gas production: effects of ceria-doping and hydrogen sulfide on the performance of nickel-based anode materials.* Dalton Transactions, 2011. **40**(20): p. 5494-5504.
135. Finnerty, C.M., et al., *Carbon formation on and deactivation of nickel-based/zirconia anodes in solid oxide fuel cells running on methane.* Catalysis Today, 1998. **46**(2–3): p. 137-145.
136. Triantafyllopoulos, N.C. and S.G. Neophytides, *The nature and binding strength of carbon adspecies formed during the equilibrium dissociative adsorption of CH4 on Ni–YSZ cermet catalysts.* Journal of Catalysis, 2003. **217**(2): p. 324-333.
137. Alzate-Restrepo, V. and J.M. Hill, *Effect of anodic polarization on carbon deposition on Ni/YSZ anodes exposed to methane.* Applied Catalysis A: General, 2008. **342**(1–2): p. 49-55.
138. H. Oppolzer, *Analytics for Materials, Siemens-Review Special-R&D*. 1996: Fall. p. p.5.
139. Yokokawa, H., S. Yamauchi, and T. Matsumoto, *Thermodynamic database MALT2 and its applications to high temperature materials chemistry.* Thermochimica Acta, 1994. **245**(0): p. 45-55.
140. Chen, M., et al., *Thermodynamic modeling of the La–Mn–Y–Zr–O system.* Calphad, 2006. **30**(4): p. 489-500.
141. Taniguchi, S., et al., *Degradation phenomena in the cathode of a solid oxide fuel cell with an alloy separator.* Journal of Power Sources, 1995. **55**(1): p. 73-79.
142. Matsuzaki, Y. and I. Yasuda, *Electrochemical properties of a SOFC cathode in contact with a chromium-containing alloy separator.* Solid State Ionics, 2000. **132**(3–4): p. 271-278.
143. Yokokawa, H., et al., *Thermodynamic considerations on Cr poisoning in SOFC cathodes.* Solid State Ionics, 2006. **177**(35–36): p. 3193-3198.
144. Larrain, D., J. Van herle, and D. Favrat, *Simulation of SOFC stack and repeat elements including interconnect degradation and anode reoxidation risk.* Journal of Power Sources, 2006. **161**(1): p. 392-403.
145. Wuillemin, Z., et al., *Modeling and Study of the Influence of Sealing on a Solid Oxide Fuel Cell.* Journal of Fuel Cell Science and Technology, 2008. **5**(1): p. 011016-9.
146. Matsuzaki, Y. and I. Yasuda, *The poisoning effect of sulfur-containing impurity gas on a SOFC anode: Part I. Dependence on temperature, time, and impurity concentration.* Solid State Ionics, 2000. **132**(3–4): p. 261-269.
147. Cheng, Z., S. Zha, and M. Liu, *Influence of cell voltage and current on sulfur poisoning behavior of solid oxide fuel cells.* Journal of Power Sources, 2007. **172**(2): p. 688-693.
148. Hattori, M., et al., *Effect of annealing on the electrical conductivity of the Y2O3–ZrO2 system.* Journal of Power Sources, 2004. **131**(1–2): p. 247-250.
149. Van Herle, J. and R. Vasquez, *Conductivity of Mn and Ni-doped stabilized zirconia electrolyte.* Journal of the European Ceramic Society, 2004. **24**(6): p. 1177-1180.
150. Haering, C., A. Roosen, and H. Schichl, *Degradation of the electrical conductivity in stabilised zirconia systems: Part I: yttria-stabilised zirconia.* Solid State Ionics, 2005. **176**(3–4): p. 253-259.
151. Sasaki, K., et al., *H[sub 2]S Poisoning of Solid Oxide Fuel Cells.* Journal of The Electrochemical Society, 2006. **153**(11): p. A2023-A2029.
152. Haga, K., et al., *Poisoning of SOFC anodes by various fuel impurities.* Solid State Ionics, 2008. **179**(27-32): p. 1427-1431.
153. Shaffer, S., *Development Update on Delphi's Solid Oxide Fuel Cell Power System*. 2004, SECA: Philadelphia, PA.
154. Bujalski, W., C.M. Dikwal, and K. Kendall, *Cycling of three solid oxide fuel cell types.* Journal of Power Sources, 2007. **171**(1): p. 96-100.

155. Horita, T., et al., *Effects of impurities on the degradation and long-term stability for solid oxide fuel cells.* Journal of Power Sources, 2009. **193**(1): p. 194-198.
156. Komatsu, T., et al., *A long-term degradation study of power generation characteristics of anode-supported solid oxide fuel cells using LaNi(Fe)O3 electrode.* Journal of Power Sources, 2009. **193**(2): p. 585-588.
157. Park, K., et al., *Fast performance degradation of SOFC caused by cathode delamination in long-term testing.* International Journal of Hydrogen Energy, 2010. **35**(16): p. 8670-8677.
158. Tietz, F., et al., *Performance of LSCF cathodes in cell tests.* Journal of Power Sources, 2006. **156**(1): p. 20-22.
159. Mai, A., et al., *Time-dependent performance of mixed-conducting SOFC cathodes.* Solid State Ionics, 2006. **177**(19-25): p. 1965-1968.
160. Komatsu, T., et al., *Degradation behavior of anode-supported solid oxide fuel cell using LNF cathode as function of current load.* Journal of Power Sources, 2010. **195**(17): p. 5601-5605.
161. Simner, S.P., et al., *Silver-perovskite composite SOFC cathodes processed via mechanofusion.* Journal of Power Sources, 2007. **168**(1): p. 236-239.
162. Simner, S.P., et al., *Performance of a novel La(Sr)Fe(Co)O3–Ag SOFC cathode.* Journal of Power Sources, 2006. **161**(1): p. 115-122.
163. Yamaguchi, T., et al., *Electrochemical characterizations of microtubular solid oxide fuel cells under a long-term testing at intermediate temperature operation.* Journal of Power Sources, 2011. **196**(5): p. 2627-2630.
164. Akhtar, N., et al., *Mixed-reactant, micro-tubular solid oxide fuel cells: An experimental study.* Journal of Power Sources, 2009. **193**(1): p. 39-48.
165. C. M. Dikwal, W.Bujalski, and K. Kendall, *Thermal cycling of microtubular SOFC.*, in *8th European Solid Oxide Fuel Cell Conference*. 2008: Lucerne.
166. M. Prica and et al., *Solid oxide fuel cells (SOFC-V) : proceedings of the fifth International Symposium on Solid Oxide Fuel Cells*. 1997, Pennington, NJ: Electrochemical Society, inc.
167. Sales, K. and e. al., *Ceramics in Energy Applications*, in *Second International Conference on 'Ceramics in Energy Applications'*. 1994, Institute of Energy,: London. p. p. 55-63.
168. Pusz, J., et al., *Fracture strength of micro-tubular solid oxide fuel cell anode in redox cycling experiments.* Journal of Power Sources, 2007. **163**(2): p. 900-906.
169. Dikwal, C.M., *Cycling Studies of Micro-tubular Solid Oxide Fuel Cells*, in *School of Chemical Engineering*. June, 2009, University of Birmingham. p. 232.
170. Hsiao, Y.C. and J.R. Selman, *The degradation of SOFC electrodes.* Solid State Ionics, 1997. **98**(1–2): p. 33-38.
171. Simwonis, D., F. Tietz, and D. Stöver, *Nickel coarsening in annealed Ni/8YSZ anode substrates for solid oxide fuel cells.* Solid State Ionics, 2000. **132**(3–4): p. 241-251.
172. Waldbillig, D., A. Wood, and D.G. Ivey, *Electrochemical and microstructural characterization of the redox tolerance of solid oxide fuel cell anodes.* Journal of Power Sources, 2005. **145**(2): p. 206-215.
173. X.Y. Zhou, A. Pramuanjaroenkij, and a.S. Kakaç, *A Review on Miniaturization of Solid Oxide Fuel Cell Power Sources-I: State-of-The-Art Systems*, in *Mini -Micro Fuel CellsFundamentals and Applications*, S. Kakacs, A. Pramuanjaroenkij, and a.L. Vasiliev, Editors. 2007, Springer: Cesme – Izmir, Turkey. p. 303-3018.
174. Liu, L., G.-Y. Kim, and A. Chandra, *Modeling of thermal stresses and lifetime prediction of planar solid oxide fuel cell under thermal cycling conditions.* Journal of Power Sources, 2010. **195**(8): p. 2310-2318.
175. N Hart and e. al. *Improving the manufacture and durability of multi-cell modules for the IP-SOFC*. 2001 [cited 2013 29/01]; Available from: http://webarchive.nationalarchives.gov.uk/+/http://www.berr.gov.uk/files/file15287.pdf.
176. Spangler, A. and G. Agnew, *9th Grove Fuel Cell Symposium*. 2005: London, UK.

177. Ben Haberman, Carlos Martinez Baca, and G. Rush. *Overview of the Rolls-Royce Fuel Cell Multi-Physics Code Project*. 28 July 2011 [cited 2013 21/02]; Available from: http://www.netl.doe.gov/publications/proceedings/11/seca/pdf/Thu%20AM/Haberman.%20SECA%20Workshop%20v4_28July11.pdf.
178. Lee, T.J., *Characterisation of anode supported microtubular SOFC process on pure methane reduction and operation*, in *School of Chemical Engineering*. 2010, University of Birmingham. p. 148.
179. Preece, J.C., *Oxygenated hydrocarbon fuels for solid oxide fuel cells*, in *Chemical Engineering*. 2006, University of Birmingham. p. 195.
180. Meusinger, J., E. Riensche, and U. Stimming, *Reforming of natural gas in solid oxide fuel cell systems.* Journal of Power Sources, 1998. **71**(1–2): p. 315-320.
181. Washburn, E.W., *Note on a Method of Determining the Distribution of Pore Sizes in a Porous Material.* Proceedings of the National Academy of Sciences, 1921. **7**(4): p. 115-116.
182. [cited 2013 21/02]; Available from: http://mtixtl.com/diamondsaw-syj-40.aspx.
183. A. Hagen, et al., *Durability Study of SOFCs Under Cycling Current Load Conditions.* FUEL CELLS, 2009. **9**(6): p. 814–822.
184. Gemmen, R.S., M.C. Williams, and K. Gerdes, *Degradation measurement and analysis for cells and stacks.* Journal of Power Sources, 2008. **184**(1): p. 251-259.
185. Leone, P., et al., *Experimental investigations of the microscopic features and polarization limiting factors of planar SOFCs with LSM and LSCF cathodes.* Journal of Power Sources, 2008. **177**(1): p. 111-122.
186. Offer, G.J. and N.P. Brandon, *The effect of current density and temperature on the degradation of nickel cermet electrodes by carbon monoxide in solid oxide fuel cells.* Chemical Engineering Science, 2009. **64**(10): p. 2291-2300.
187. Sohal, M.S., *Degradation in Solid Oxide Cells During High Temperature Electrolysis*. 2009: Idaho Falls.
188. Noren, D.A. and M.A. Hoffman, *Clarifying the Butler–Volmer equation and related approximations for calculating activation losses in solid oxide fuel cell models.* Journal of Power Sources, 2005. **152**(0): p. 175-181.
189. Akkaya, A.V., *Electrochemical model for performance analysis of a tubular SOFC.* International Journal of Energy Research, 2007. **31**(1): p. 79-98.
190. Hjelm, J. *Degradation Testing: Quantification and Interpretation*. in *2nd International Workshop on Degradation Issues of Fuel Cells*. 2011. Thessaloniki: National Laboratory for Sustainable Energy.
191. Borglum, B., E. Tang, and M. Pastula, *Development of Solid Oxide Fuel Cells at Versa Power Systems.* ECS Transactions, 2011. **35**(1): p. 63-69.
192. Greg Gege Tao and Anil V. Virkar. *Lessons Learned from SOFC/SOEC Development*. in *REVERSIBLE FUEL CELLS Workshop in NREL/DOE*. 2011. Crystal City, Virginia: Materials and Systems Research, Inc.
193. Dikwal, C.M., W. Bujalski, and K. Kendall, *The effect of temperature gradients on thermal cycling and isothermal ageing of micro-tubular solid oxide fuel cells.* Journal of Power Sources, 2009. **193**(1): p. 241-248.
194. Mallon, C., *Nickel Cermet Anode Optimisation for Micro-Tubular Solid Oxide Fuel Cell Operation on Alkanes*, in *Chemical Engineering*. 2006, The University of Birmingham: Birmingham.

10 Appendices

10.1 Nomenclature & Abbreviations

The abbreviations and terminology are defined in the following tables:

Abbreviation	Full Description
SOFCs	Solid Oxide Fuel Cells
RRFCS	Rolls Royce Fuel Cell Systems
IP-SOFC	Integrated Planar Solid Oxide Fuel Cell
ADT	Accelerated degradation testing
TPO	Temperature-programmed oxidation
CO_2	Carbon Dioxide
DC	Direct current
AC	Alternating current
PEMFC	Proton Exchange Membrane Fuel Cell
AFC	Alkaline Fuel Cell
PAFC	Phosphoric Acid Fuel Cell
MCFC	Molten Carbonate Fuel Cell
H_2	Hydrogen
CO	Carbon monoxide
H_2O	Water
O_2	Oxygen
CHP	combined heat and power
YSZ	Yttria Stabilised Zirconia
LSM	Lanthanum Strontium Manganate
TPB	three phase boundary
Ni	Nickel
NiO	Nickel oxide
SSZ	scandia-stabilized zirconia

LSGM	strontium/magnesium-doped lanthanum gallate
LSMC	lanthanum strontium manganese chromite
LSCF	lanthanum strontium cobalt ferrite
Cu	Copper
Redox	Reduction and Oxidation
Fe	Iron
CGO	Cerium gadolinium oxide
SDC	Samaria doped ceria,
η_{act}	Activation polarizations
η_{ohm}	Ohmic polarizations
η_{conc}	Concentration polarizations
V_{cell}	Net voltage
Ru	Ruthenium
ScSZ	scandia stabilised zirconia
S/C	carbon ratio
C	Carbon
TPR	temperature-programmed reduction
OCV	open circuit voltage
Cr	Chromium
H_2S	Hydrogen Sulfide
Cl_2	Chlorine
PEN	Positive-Electrolyte-Negative
UPS	uninterruptable power supply
CTE	Coefficient of Thermal Expansion
SEM	Scanning Electron Microscopy

CH4	Methane
DR	degradation rate
ASR	area-specific resistance
F	Faraday's constant.
ΔG^{o}	Gibbs free energy

10.2 Publications

Papers:

1. G. Almutairi, K. Kendall, and W. Bujalski, Cycling durability studies of IP-SOFC. *International Journal of Low-Carbon Technologies*, 2012. 7(1): p. 63-68.

2. Ghzzai Almutairi, Aman Dhir and Waldemar Bujalski, Direct operation of IP-Solid Oxide Fuel Cell with hydrogen and methane fuel mixtures, submitted to *Fuel Cells.*

3. Ghzzai Almutairi, Aman Dhir and Waldemar Bujalski, *Analysing carbon deposition on Ni/YSZ anode of Integrated Planar Solid Oxide Fuel Cell (IP-SOFC)*, submitted to Journal of Power Sources.

Posters:

1. G. Almutairi, W. Bujalski* and K. Kendall, Durability studies of Rolls Royce IP-SOFC, 6th Annual International Conference & Exhibition “Hydrogen & Fuel cells for Clean Cities” 25 March 2010, Gallery Suite, NEC, Birmingham, UK.

2. G. Almutairi, A. Dhir and W. Bujalski,IP-SOFC Operated on Hydrogen-Methane Mixture as fuel, **7**th Annual International Conference & Exhibition “Hydrogen & Fuel cells for Clean Cities” 2011, Gallery Suite, NEC, Birmingham, UK.

3. Ghzzai Almutairi, Aman Dhir and Waldemar Bujalski, Direct operation of IP-Solid Oxide Fuel Cell with hydrogen and methane fuel mixtures, EMHyTeC 2012, Hammamet, Tunisia, September 11-14, 2012.